Modeling of Photocurrent Transient Response in a-Si:H Pixel Sensor for Diagnostic Implications

Shaikh Noora Alam

A Thesis

in

The Department

of

Electrical and Computer Engineering

Presented in Partial Fulfillment of the Requirements
for the Degree of Master of Applied Science (Electrical & Computer Engineering) at
Concordia University
Montreal, Quebec, Canada

August 2007

Your file Votre référence
ISBN: 978-0-494-40876-6
Our file Notre référence
ISBN: 978-0-494-40876-6

ABSTRACT

Modeling of photocurrent transient response in a-Si:H Pixel Sensor for diagnostic implications

Shaikh Noora Alam

Amorphous silicon based sensor technology transcends the limits of conventional imaging and is the foundation for innovative solutions in radiology. Biometric detections, clean power generations, preventive security, bulk production monitoring, NDT (non-destructive testing) and PACS (picture archival and communication system) facilitated remote analysis etc, all benefits can be provided by AMFP (active matrix flat panel) hydrogenated amorphous silicon (a-Si:H) imaging sensors. Creative designs and innovative digital approach of a-Si:H sensors could ensure defined promise for exciting new generation of cost-effective, reliable, and real-time x-ray imaging pixel sensor. This research pursued to model such a visionary device to comply these challenges and to meet efficient, compact and flexible x-ray image detector into integral readout arena. In this thesis, primarily present a numerical model of transient photoresponse for a-Si:H pixel photodiode in active matrix 2-D environments. In numerical model, we considered all possible charge transport properties such as carriers drifting, trappings/de-trappings and recombination. The architecture configured as p-i-n structured a-Si:H photodiode and addressed by thin film pass transistor and integrated with charge storage capacitor. This work also includes quantitative study, test, and characterize the combined effects of the photodiode with varying geometry, and operating conditions by a customized simulator. The simulator code has written based on numerical model equations. Therefore, the simulator itself a model device and is operable in soft-hand environment to realize true device before fabrication. Our soft-hand experimental set up is based on indirect conversion principle and overall architecture is AMFP detection system.

ACKNOWLEDGEMENTS

I would like to thank my wife ***Sonali*** **Shahanaz**, who has always been there with love and compassion and also ever inspiration my daughter **Ariya Noor** ***Ahona***, her continual smile and kitty questionnaire keeps me alive to stay in the course. My mother who also has been there with restless compassion since my birth, and for that I am ever grateful to her.

I would like to express my sincere thanks to my supervisor, **Dr. Mojtaba Kahrizi** for his technical, emotional, financial supports, and friendship guidance during my entire research. This work would never be realized without his guidance. His insistence that I continually delve deeper for the underlying truth is appreciated and a lesson well learned days to come.

I would like to thank Dr. M. Zahangir Kabir for his strategical support and technical advice during this work. My appreciation goes to all of my course instructors at University of Concordia. Special thanks to professors Mojtaba Kahrizi, V.K. Sood, Luiz A.C. Lopez, M. Reza Soleymani, Wei-Ping Zhu, X. Wang and Ted Obuchowicz. Dr. Simona Badilescu deserves mention here for the many occasions that she graciously offered her time and assistance, and for that I am grateful to her. My sincere thank goes to Professor Gordon Roberts from McGill University, who help me out in many ways during my research, especially mix-signal orientations. I also greatly value the lessons that I received from my fellow researcher/colleagues and deeply admire their contributions.

I would also like to express my sincere appreciation to University of Concordia, NSERC and Ministry of education and training, Ontario, Canada for their financial support during the past two years of my study.

COPYRIGHT

TABLE OF CONTENTS

LIST OF FIGURES

LIST OF TABLES

LIST OF ABREVIATIONS

a-Si Amorphous Silicon

AMA Active Matrix Array

AMFP Active Matrix Flat Panel

ASIC Application Specific Integrated Circuit

Ar Argon

CCDCharge Coupled Device

CsI Cesium Iodide

CMOS Complementary Metal Oxide Semiconductor

CT Computed tomography

CFO Cohen, Fritzche, and Ovshinsky

DQEDetective Quantum Efficiency

EHP Electron-Hole Pairs

FPD Flat Panel Detector

Fps frame per second

FF Fill factor

ITO Indium Tin Oxide

IC Integrated Circuits

IIT Imaging Intensifier Tube

LCD Liquid crystal display

MRI Magnetic resonance imaging

MO Marshal and Owen

Mo Molybdenum

MIS Metal-Insulator-Si

NDTNon-Destructive Test

NSB Normal structure bonding

PD Photodiode

PPD Pixel photodiode

PET Position emission tomography

PECVDPlasma Enhanced Chemical Vapor Deposition

PACS Picture Archiving and Communication System

p-i-n p doped-intrinsic-n doped

QE Quantum efficiency

SoC System on Chip

SPECT Single photon emission computed tomography

SIMS Scanning ion mass spectrometry

TFT Thin Film Transistor

WAN Wide Area Network

2D Two Dimensional

Chapter 1: Introduction, Objectives and Thesis Organization

1.0 Introduction

Since discovery of x-rays by Wilhem Roentgen, numerous researches have been led in various disciplines. Among them radiology are frontier as the radiographic imaging being remained as one of the most useful tools to aid physicians. In diagnostic imaging applications, currently available instrumentation imposes significant constraints and limitations, especially in fluoroscopic use. The recent advancement in fabrication and development of hydrogenated amorphous silicon (a-Si:H) semiconductors offer the prospect of active matrix flat-panel imaging tips, which would eliminate hopefully many of these constraints that exists in present modalities [1].

The active-matrix flat-panel imagers demonstrate high x-ray sensitivity combined with low-noise, and hence offer high image quality over a wide range of radiation exposure. Moreover, a-Si:H is ideal for x-ray detectors because it is immune to radiation damage. A flat-panel digital detector, in principle could perform all current radiological modalities. Flat-panel sensor imaging also promises to eliminate the film that is use in radiography by supplanting it with a large area a-Si detector that has a comparable field-of-view. Furthermore it promises significant improvement of present day digital fluoroscopy by replacing the bulky image-intensifier/video-camera with smaller, lighter, and portable imagers. Also, advancement in this field may lead to systems appropriate to through digital mammography [2]. Amorphous silicon detectors may also be used in many others x-ray imaging applications, such as bone mineral densitometry, x-ray crystallography and diffraction analysis, or even detection of explosive devices.

The digital x-ray systems and its much use extend beyond solely clinical application to non-destructive testing (NDT) in industry. Casting or electronic component inspections, high volume manufacturing inspection, component operation, structural integrity or process analysis are only a few examples of industrial applications that may be improved with the incorporation of a-Si sensor technology. Current world politics dictates, security is no longer an option but obligatory preventions. This technology can provides faster, convenient and mobile ways to take real-time images for in use especially airport, law enforcement and military personnel for strategic analysis. Its ability to quickly view a clear digital "snapshot" or moving image of objects- instantly can be transmitted electronically to the associated security offices for further evaluations.

Biometric detection, vehicle or luggage inspection, portable and remote analysis and other security applications, all benefit can be provided by light weight, compact size and real-time thinned AMFP arrayed a-Si imaging systems. Our successive efforts in this work, mostly concentrated on individual pixel sensor and more precisely the transient photoresponse of pixel photodiode only.

1.1 Radiographic image succession concepts

In radiography, the creation of images by measuring the differential attenuation of ionizing radiation, such as x-rays which pass through a body, is well established diagnostic tool in hospitals and medical clinics. Currently, radiographic professionals still depends on film emulsion to store the optical response that is generated when incident x-ray photons interact with a phosphorescent screen. The film and screen are coupled together and packaged as an x-ray detector cassette, which is manually inserted into the

radiographic system prior to exposing the patient and processed in different set-ups. When the image quality does not realize up to the mark, further processed is must. The resulting image prints are hazardous, difficult to handle and store. It must be physically examined on a lighted view box to diagnose the patient's condition.

On the other hand, digital imaging technology has the potentiality to make the process of capturing x-ray images considerably more efficiently and resourceful [3]. Ideally, a digital radiographic system is capable to re-construct the image data to generate the quality image, automatically adjustable the exposure settings as necessary, and display a digital image immediately after the x-ray exposure on a video monitor. Such "real-time" detectors are ideally suited for fluoroscopic procedures, where a motion picture is generated to aid internal guiding therapies such as angioplasty.

The digital option also offered several advantages over analog counterpart; for instance contrast, resolution, picture archival and communication system (PACS) etc. Moreover, analytical software can be used to enhance the quality of the digital image as being used in current available technology or to facilitate the 3-D computer-aided-diagnoses in case of complex medical situations [4]. The digital image data files can easily be stored on servers and shared over computer networks for the provision of clinical care to individuals over wide area network (WAN) for remote users [5].

The p-i-n photodiode array can be easily deposited over a large area at low cost with the compatible processes to fabricate with thin film transistor in array [6]. In addition, its overall detective quantum efficiency is comparatively rich and ideal to the x-ray imager to obtain images for medical diagnosis in practical applications. However, inherent high leakage current of an a-Si:H p-i-n photodiode, can in practice adversely

affect the integration of the p-i-n diodes with peripheral electronics. The leakage of the photodiode should be as small as possible since the detected signal is in the form of the electric charge stored in each pixel capacitor, and the signal shouldn't be lost before it is read-out.

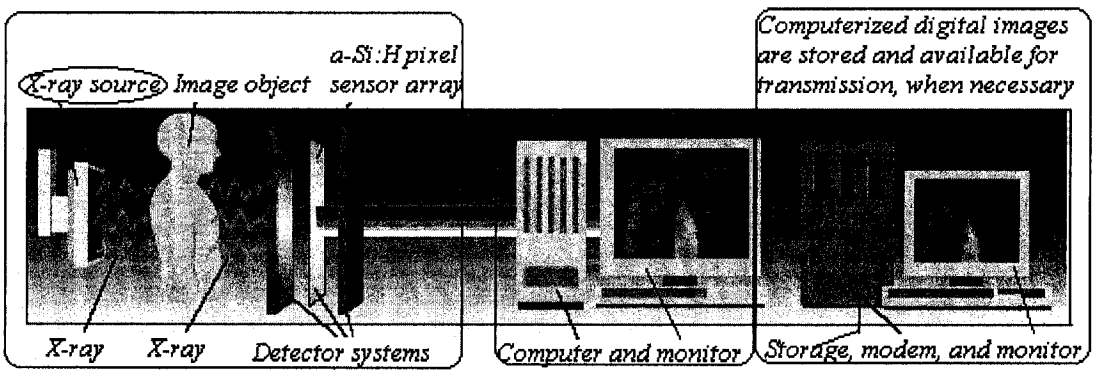

Figure 1.1: X-ray imaging system graphical orientations and layout [7].

The x-rays impinging on the phosphor screen give off light that exposes on the sensors to create a latent image that is subsequently amplified and implied digital imaging techniques to interface with the digital world as shown in Figure 1.1. The informative x-ray photons after object let expose onto detector photodiodes via scintillator. The scintillator converts the informative x-ray photons into electronic carriers in two-stage conversion. Eventually the charges are stored over scan period of time in to charge collection capacitors, located in each unit of AMA pixels [7]. Photodiode array is the key element of an active matrix x-ray imaging system and determines the phenomenal characteristics of the system.

When converted visible light photons absorb in fully depleted intrinsic region of a-Si:H p-i-n photodiode, the light photons generate electron-hole pairs (EHP). The

generated carriers later on sweep out by applied external fields and accumulated carriers bear the latent image impression. In fact, the collected carrier causes low-level current signal that are proportional to the level of illumination. After an integrated complexity, one can achieve complete image detections so forth. A complete flow diagram has been shown in Figure 1.2 to understand the level of total functionality of digital image realization by a-Si:H pixel sensors.

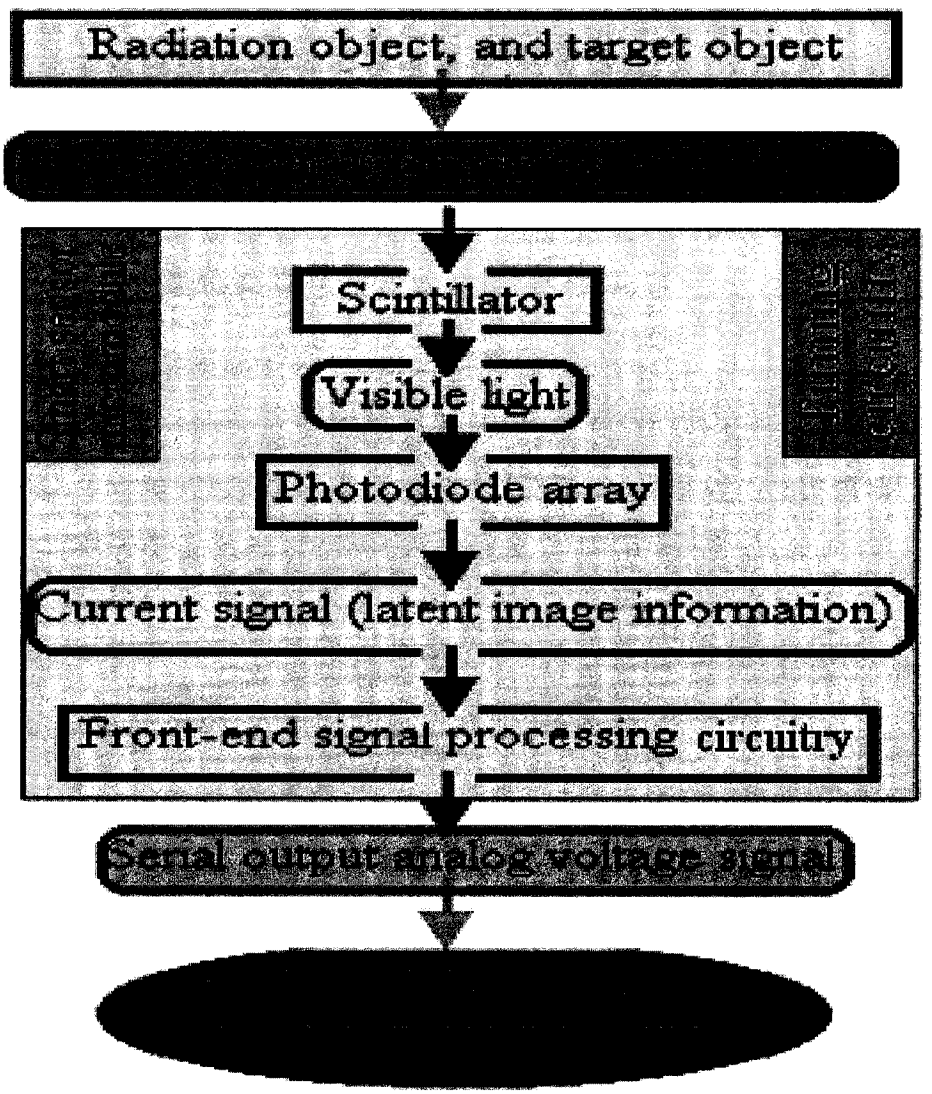

Figure 1.2: Signal flow chart of a typical x-ray imaging digital system.

1.2 Radiographic image realization by photodetector

Current researches are mostly involved in either large area flat panel imaging applications or linear imaging systems. The linear imaging systems, such as photocopies, fax machines and scanners, where sensors are arrayed so that sensed linearly to have image of the object of interest only. But in large area flat panel imaging systems, we pretty much deal with two-dimensional (2-D) systems. For instance optical or video cameras, where matrix based 2-D sensing systems have been realized to have an image signal. These systems are tactfully up by CCD or CMOS imaging chips coupled with optical means to transfer the large area information to the small sensitive area. In both linear and 2-D systems, the basic imaging unit is called a pixel, which is comprised by an image sensor and a switch. One of the basic and most widely used pixels in 2-D configuration is shown in Figure 1.3.

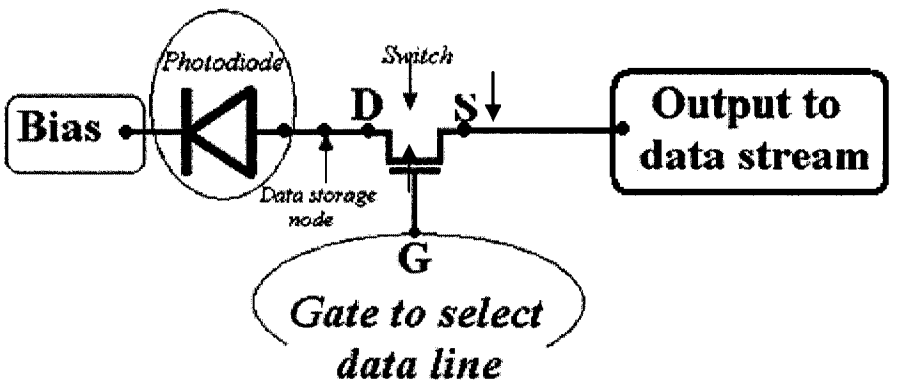

Figure 1.3: The basic pixel schematic, where storage mode is employed.

The pixel consists of either a field effect transistor (FET) exploiting CMOS technology or thin film transistor (TFT) technology, connected with a photodiode being an optical sensor. Our research is mostly focused on a-Si:H photodiode based image

detections; we investigate its inner physics to model transient photoresponse so that an engineered image signal could be realized at pixel environment. The carriers can be integrated over a time of interest to yield a permissible signal. When a voltage pulse is applied to the gate line, the charges in the photodiode are transferred to the data lines where they are detected further by a sensitive amplifier. Prior to this readout mode, the generated carriers are stored in capacitor for clock scan time as integration mode [8].

1.3 Image sensors array architecture

A 2-D imaging array with active matrix readout is shown in Figure 1.4 [9,10]. The TFT in each pixel acts as an electronic switch with three electrical connections – drain, source and gate. The drain is connected to the photodiode, the source is connected to a data line, which is routed to an external charge sensitive amplifier, and the gate is connected to the scanning control line.

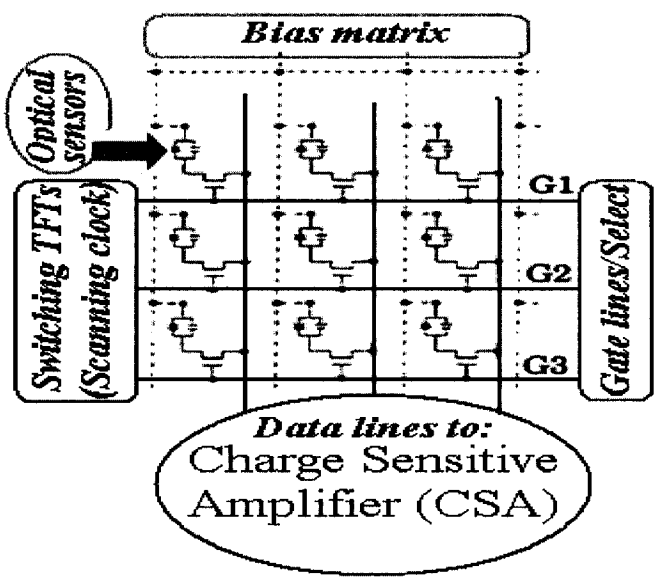

Figure 1.4: Architecture of 2-D imaging array.

All the pixels of the same column share a common data line and an amplifier. The readout of the entire detector can be performed in real-time basis, thus permitting the creation 2-D live images. In 2-D imaging process, the scanning clock selects one row of TFT switches and turns on all the switches in this row. The charges of each photodiode are transferred through the TFT switch to an integrated storage capacitor available in each individual pixel in array basis, then input of (external) amplifier through the same clock. The clock trailing edge turns off the switch. The signal at the amplifier input is transferred to the amplifier output. Finally the reset signal resets the amplifier input to zero. The cycle is repeated for the next row until all rows are scanned. The signal readout is then transferred to the image processor for data analysis and video display.

1.4 a-Si:H imaging technology

Recently, optical and x-ray imaging using hydrogenated amorphous silicon (a-Si:H) technology have gained great promise. As depicted in Figure 1.4, each pixel must have one photodiode and one TFT. a-Si:H technology enables the easy manufacture of large area electronics at low temperature (~250°C) [11] in contrast to the single-crystal (CCD or CMOS) technology, which imposes restrictions in terms of either higher cost or limited detectable area. The a-Si:H fabrication process is borrowed from the IC technology. Since a-Si:H is in a state of greater disorder, it could be expected to be considerably less sensitive to radiation damage than its single crystalline silicon (c-Si) counterpart. Image sensor technologies of c-Si and a-Si:H is compared in Table 1.1, and demonstrated a clear possibility for higher quality, speed, and resolution [12]. However,

the low optical irradiation level and photosensitivity still need to be improved for x-ray imaging medical use.

Table 1.1: Silicon semiconductor based diagnostic imaging sensor; a comparison between crystalline silicon to hydrogenated amorphous silicon sensor properties.

Properties	c-Si	a-Si:H
Sensitivity to visible light	Yes	Yes
Response time	10 to 100 ps	500 to 1 μs
Radiation sensitivity	No	Yes
Large area compatibility	No	Yes

As the a-Si:H Schottky interfaces are operated under reverse bias, the shift in leakage current with time can be a major concern. In many applications, a leakage current of 10^{-10} A/cm^2 is low enough to achieve an imaging system with 30 frames per second (fps). As listed in Table 1.2, the leakage current of the p-i-n photodiode structures is lower than that of counterparts [13]. The mechanisms underlying the leakage current and the interface integrity are still in favor of p-i-n architecture.

Table 1.2: The comparative performance of a-Si:H image pixel with different photoconductive structure.

Parameters↓	p-i-n PD	Schottky diode	Photoconductor	Photo TFT
Photosensitivity	Low	Low	High	High
Response time (μs)	Fast (<5)	Fast (~50)	Slow (~500)	Slow (~500)
Dark current (A/cm^2)	10^{-10}~10^{-12}	10^{-7}~10^{-9}	~10^{-6}	10^{-7}~10^{-8}
Stability	Good	Good	Good	Acceptable
Large area compatibility	Yes	Yes	Yes	Yes

1.5 Research objectives

Amorphous semiconductors have been experienced widespread application over the last decade. Its commercialization and the potential new applications have fuelled considerable interest in studying the electronic properties of amorphous semiconductors. The present work aims to further understanding of the physical processes involved in charge carriers transport in a-Si:H photodiode. The study of transient photoresponse in hydrogenated amorphous silicon photodiode in a-Si:H pixel sensor is intended to advance the current understanding of silicon and other amorphous materials as well. Besides the commercial interest in the material, amorphous silicon has recently been the topic of considerable scientific interest in terms of its efficient photosensitivity.

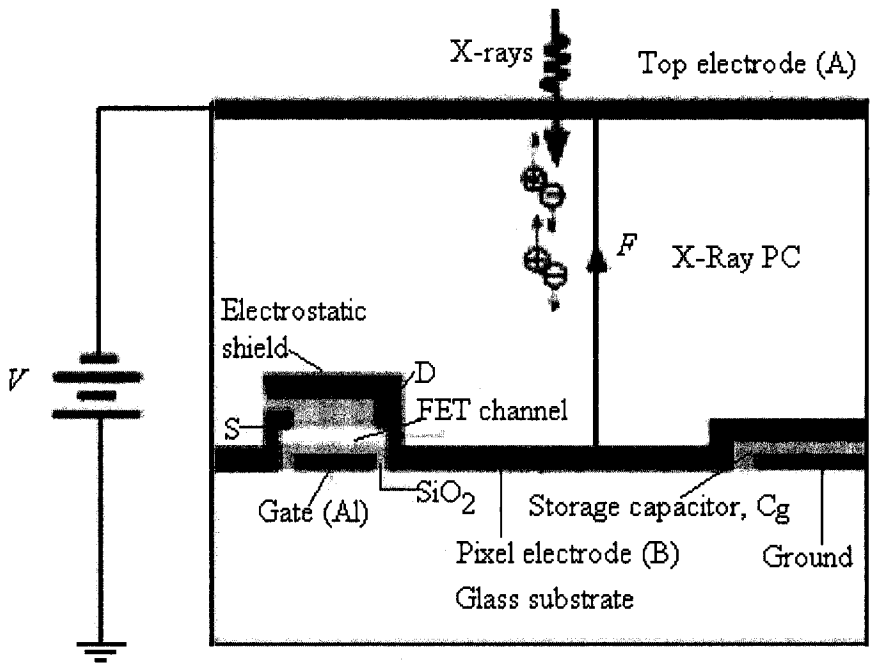

Figure 1.5 : Highly simplified cross section of a single pixel (i, j) with a TFT showing the accumulation of x-ray generated charge on the pixel electrode and, hence the storage capacitance Cg. The top electrode (A) on the photoconductor is a vacuum coated metal (e.g., Al). The bottom electrode (B) is the pixel electrode that is one of the plates of the storage capacitance (Cg) [15]. (Not to scale and the FET height is highly exaggerated).

In the past, there have been limited descriptions and behavioral depictions of photoresponses in amorphous silicon semiconductor. In previous works, models based on a-Si:H sensors were reported [14]. In those models only the contribution of one of the carriers (either electrons or holes) were considered. Also, researchers were trying to achieve 100% fill factor (FF). As we were focused on the transient photoresponse modeling of a-Si:H photodiode in pixel sensor, we adapted the TFT switch and storage capacitor from previously reported works as shown in figure 1.5 [15]. However, in our work we used different architecture in prototype manner. Accordingly our proposed pixel architecture as shown in chapter 4, the photodiode will be fabricated on top of the thin film transistor (TFT) and storage capacitor in order to achieve about 100% FF.

As mentioned, previous reported models were derived based on either electrons or holes contributions basis. In our approach, we model a device based on continuity equations for both electrons and holes. Further we extended our work to present a customized simulator based proposed numerical model and implied optimization techniques. In this work, our goal is to develop and design a photoresponse of a-Si:H pixel photodiode (PPD), which could be integrated into AMA x-ray image pixel sensor in arrayed arena for diagnostic implications. We described inner physics of a-Si:H pixel photodiode by graphical portions of electrons and holes carrier traps in density measure in the mobility gap. Also, the subsequent photoresponses are studied for both analog and digital domain image realization with the help of ASIC peripherals.

The areas of investigation that will be undertaken in this work involve primarily the charge transport parameters of biased a-Si:H photodiodes in arrayed pixel arena. The decay currents in time domain of each individual pixel sensors are very important in

fluoroscopic use in medical science. Because it adversely constitutes in further usability perspective and unwanted ghosting effects evolved which is a long time issue in x-ray imaging era. The carrier's continuation after switched off condition restricts further use of the system. Because these extra carriers brings less prominent previous image or shadow in to the real time one, which is not expected and this unexpected natural phenomena is referred as ghosting in radiology. Secondly, how they fabricate and meet challenges the influenced parameters changes condition.

However, the basis of these experimental examinations will be the transient photodiode photoresponse modeling at varying applied fields, photoconductor thickness, dose and exposure time conditions. In order to comply research objectives, systematically we proceed numerical modeling of a-Si:H photodiode, model based simulator code writing, and displayed soft-hand experimental results.

1.6 Thesis outline

This research work is divided into six chapters. Following this introductory chapter, a review of generalized photoconductor principles, useful theories, definitions and explanations of important applications for amorphous image detectors are given in Chapter 2. A discussion of the potential challenge in active matrix arrayed photoconductor use and properties for x-ray image detection are also taken place in this chapter. The crucial atomic structure, band architecture, doped properties and alloying characteristics of amorphous materials are explained in chapter 3. The deposition techniques of hydrogenated amorphous silicon (a-Si:H) and conductive electrodes are also described in this chapter. Further, the development of different physical layers and

issues, such as p-i-n active layers, transparent (ITO) top electrode, and bottom electrode (Mo) in imaging perspectives are discussed.

The numerical model developments for a-Si:H photodiode for imaging sensor as well as model based customized simulator creations are successfully developed and deployed in chapter 4. The verifications of simulator are also successfully employed in this chapter. In chapter 5, the post modeling soft-hand simulative experiments were conducted and analyzed at varying fields, active layer thickness, dose and exposure condition of the photodiode to optimize operable parameters and pixel architecture. Finally, the conclusions drawn from the theoretical calculations and experimental results all are presented in Chapter 6 along with recommendations for future works. The fabrication techniques of x-ray imaging pixel sensor are illustrated in appendix G.

Chapter 2: Amorphous Semiconductors Techno-Physics and Active Matrix Flat-Panel Applications

2.0 Background of amorphous semiconductors

Although the amorphous semiconductor has been more than three decades since it was first demonstrated to be useful as switching and memory devices, the field of amorphous semiconductor technology is still in somewhat of a period of pioneering. Crystalline semiconductors continue to dominate many applications in information processing and electronics. However, medical x-ray imaging, electrophotography, laser printing and fax technology are promising billions dollars hope based on amorphous technology. These implications of amorphous semiconductors have been tendering its importance and got much attention in commercial era.

The technology that is used to fabricate amorphous materials is comparatively simple rather than its counterpart crystalline, which require complex and careful preparation during fabrication. Therefore, the amorphous technology is growing fast and very appealing in flat panel imaging technology [16]. Unfortunately, lag of theoretical thorough understanding of the amorphous semiconductors has diminutive their growth in electronics applications. In fact, the study of amorphous semiconductors was limited for decades because of the misconceptions and conformist nature of customary solid-state physicists.

Recently, many analyses on quantum continuity behavior of charge carriers in amorphous solids have been demonstrated and already carved up some of mystery, which once steamed up the concepts of charge transport in amorphous semiconductors. One imperative concept is being emerged that the electronic properties of amorphous

semiconductors are controlled by well defined "trap levels" in the mobility gap occupied by charge in unusual energy states but behaves just they are in crystalline semiconductors. The major differences between amorphous and crystalline materials are that the crystalline solid is composed of molecules aligned in ordered in all 3-D arrays, which exhibit long-range periodicity. Although a great many useful electronic devices was made possible based on crystalline semiconductor materials, but the costs associated with complex and vigilant crystal growth are an obvious drawback.

On the other hand, a less stern fabrication requirement for amorphous materials have led their commercial value in many applications, especially those are required large active areas flat panel such as x-ray image arrayed sensors [17]. Contrary to crystalline structure, the amorphous silicon forms a class of materials with a far greater range of diversity in their physical properties. They can be insulators, semiconductors, metals, and superconductors. The preparation of amorphous materials usually requires much less care, less expensive growth techniques, and hence referred an important economic advantage over crystalline counterpart.

2.1 FPD-perspective implications

Flat panel detector (FPD) is a back bone of digital x-ray radiology. The principal difference between x-ray imaging and visible imaging is the size of the detector. CCDs (Charge coupled detectors) and CMOS imagers found in cameras and video recorders are typically on the order of one to two centimeters in area. Since x-rays are not easily focused, therefore the imager itself is necessarily on the scale of the object being imaged. Fortunately, a large-area amorphous technology exists in the form of integrated

photodiodes (PD) and thin-film-transistor (TFT) arrays. These PD-TFT arrays are currently in use in millions of laptops and their application is broadening day by day.

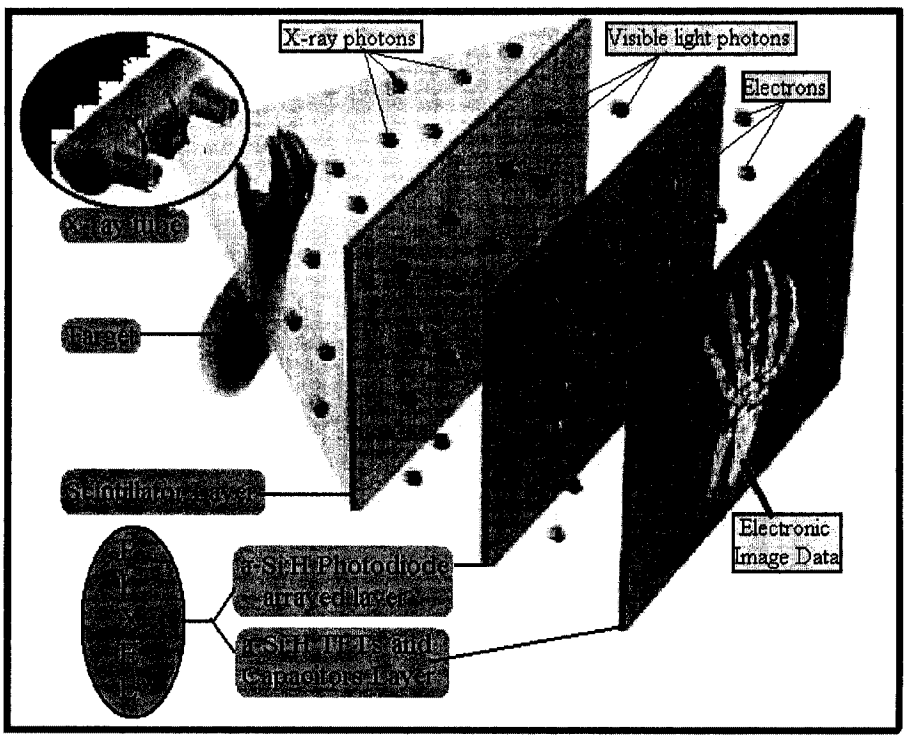

Figure 2.1: Flat panel x-ray imaging layout [18].

A number of detector technologies have been developed based on amorphous silicon TFT arrays, but the most successful and widely used detectors are called "indirect" detectors. These detectors are based on amorphous-silicon PD-TFT arrays, fundamentally coupled with x-ray scintillators as shown in Figure 2.1, which adapted from PAXSCAN® Varian medical systems. The success of the indirect FPD technology stems from the fact that both amorphous silicon and scintillator technologies are well understood and have decades of research behind them.

At a microscopic scale, the amorphous silicon has been imprinted with millions of transistors arranged in a highly ordered array, like the grid on a sheet of graph paper. Each of these TFTs and capacitors are integrated with each light absorbing a-Si:H photodiode. These three components at integrated device is referred widely known pixel (picture element). Since the number of carriers that produced will vary with the intensity of incoming light photons, an electrical pattern is created that can be swiftly read and interpreted by a computer to produce a digital image.

Although amorphous silicon has poor absorbing capability to highly x-ray photons, therefore x-rays at first let expose on scintillators, which made up from popular scintillating compounds. For instance, Gadolinium Oxysulfide or CsI has such an excellent absorber of x-rays, and coverts them to visible light photons efficiently at energies that amorphous silicon is best able to convert to charge carriers. Especially the use of compounding materials in scintillators structure raises the detective quantum efficiency (DQE) to the highest possible. DQE is the yardstick by which the performance of imagers is measured. It's a measure to quantify input radiation to output image succession phenomenon in a successive way. A high DQE means images can be acquired with either superior quality or the same quality at a lower dose.

2.2 Ideal a-Si:H x-ray indirect photodetectors

The flat-panel X-ray image detectors described in Section 2.1, with an a-Si photodiode could provide excellent images. But it requires some geometrical and physical properties to meet clinical image quality. Ideally, the indirect photodetectors in x-ray imaging technology should have the following properties [15].

- Nearly all the incident x-ray radiation should be absorbed within a practical scintillator thickness to avoid unnecessary patient exposure. This means that over the energy range of interest, the absorption coefficient due to the photoelectric effect must be large; the x-ray absorption depth must be substantially less than that of the device layer thickness.
- The photodetectors should have high intrinsic x-ray sensitivity, i.e. it must be able to generate as many convertible light photons as possible per unit of absorbed radiation. In other words, there should be a maximal visible light photons generation rate since the photon EHP generation rate is proportional to the bandgap of the photodetector material, therefore the low band gap materials would be a better option.
- The dark current should be negligibly small. This means the contacts to the photodiode should be non-injecting and the rate of thermal generation of carriers from various defects or states in the bandgap should be negligibly small. Small dark conductivity generally requires a wide bandgap semiconductor that conflicts with the second condition mentioned above. The dark current should preferably not exceed ~10–100 pA cm^{-2} depending on the clinical application.
- There should be minimal bulk recombination of electrons and holes as they drift to the collection electrodes with particular time of interest; EHPs are generated in the bulk of the photodiode. Bulk recombination is proportional to both the concentration of holes and electrons and typically it is negligible provided the instantaneous x-ray exposure is not too high.

- ❖ There should be no deep trapping of EHPs, which means that for both electrons and holes, the Schubweg range should be adequately large i.e. $\mu\tau F >> d$, where μ is the drift mobility, τ is the deep trapping time (lifetime), F is the electric field, and d is the photodiode intrinsic layer thickness. The Schubweg is the distance a carrier drifts before it is trapped and, thereby, becomes unavailable for conduction and collection by the external circuit.
- ❖ The longest carrier transit time, which depends on the smallest drift mobility, must be shorter than the access time of the pixel and inter-frame time in fluoroscopy.
- ❖ The photoconductor should be easily coated onto the AMA panel, e.g., by conventional vacuum techniques (e.g. plasma enhanced chemical vapor deposition-PECVD) without rising the temperature of the AMA to avoids damaging levels (e.g., 300°C for a-Si:H panels). Special processes are generally more expensive. A large area detector is essential in radiography since the lack of a practical means to focus x-rays necessitates a shadow x-ray image that is larger than the body part to be imaged.

The above characteristics should not change or deteriorate with time and as a consequence of repeated exposure to x-rays, i.e., x-ray fatigue and x-ray damage should be negligible. However to date, the above conditions have not been yet realized for any particular photodetector. But in order to optimize the design goals, an improved condition is always expected and that is to be our challenge in this research.

2.3 Two-dimensional (2-D) pixelated architecture

Recent research has identified that the active matrix flat-panel (AMFP) digital radiographic systems as a promising readout technique. This approach permits essentially instantaneous readout and higher quality in indirect or direct detection basis. The later term, 'direct' detection refers to the fact that the x-ray photons are directly converted to charges in the photoconductor that are subsequently collected. But with indirect-conversion systems, there is an intermediate conversion i.e. x-rays via a phosphor makes visible light photons. These light photons converted to collectable charges in the photoconductor with the presence of an external field [19, 20].

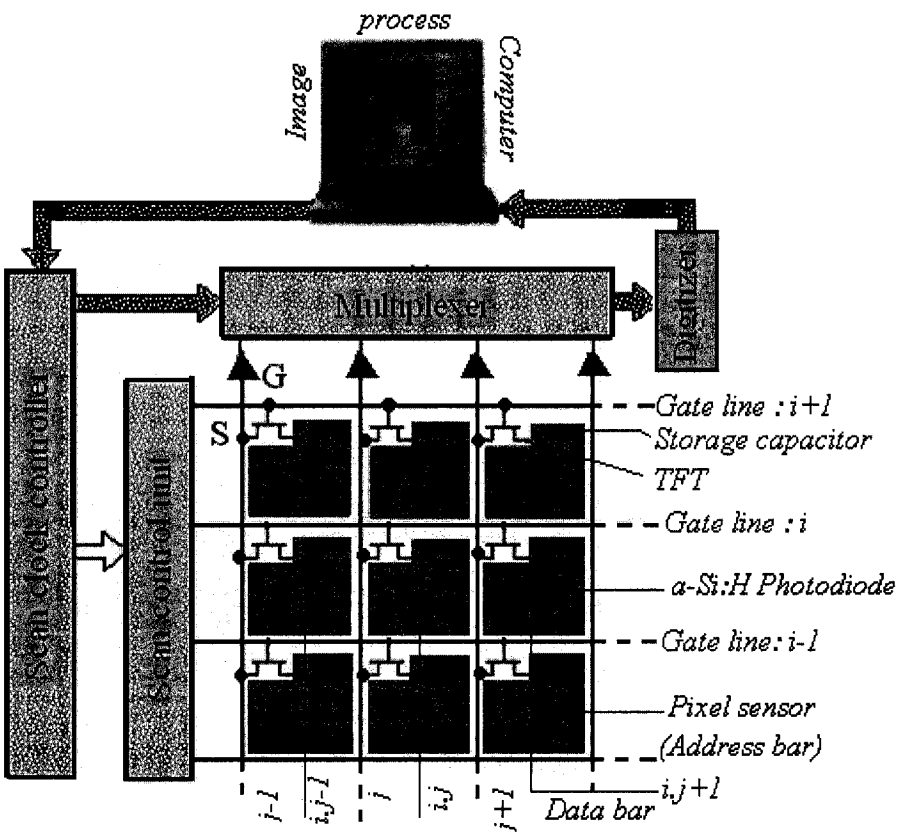

Figure 2.2: Active Matrix TFT Array for use in x-ray image detections with self-scanned electronic readout and peripheral electronics for digital signal multiplexing. Adapted from [22].

Since the development of TFT in flat-panel detector technology, the applications had been primarily limited and directed at the consumer application and displays [21]. However, the requirements for an active matrix array (AMA) as a detector are essentially identical and so x-ray detectors are a useful spin-off. Anyway, for both indirect and direct conversion approaches, the latent image is a charge distribution residing on the panel pixels. The charges simply are read out by scanning the arrays row by row using the peripheral electronics and multiplexing the parallel columns to a serial digital signal as illustrated in Figure 2.2.

This signal is then transmitted to a computer system. The system is simple, inherently digital, and has so many advantages that it has now been considered a major contender in digital radiography [22]. An AMA, as depicted in Figure 2.2, consists of similar millions of individual pixel connected by TFTs (one for each pixel) to electrodes passing over the whole array to subsidiary electronics on the periphery. The TFTs act as switches to control the clocking out of image charges per line basis at a time. The AMA consists of $(i \times j)$ storage capacitors, whose charges can be read through addressing the TFT (i,j) via the gate (i) and source (j) lines. The external readout electronics convert the charges as on in each C_{ij} to a digital image by self scanning means.

The software facilitated scanning operation is part of the flat-panel detector peripheral electronics and therefore reduced significant read-out circuitry which permitting a truly compact device. Research and development into both indirect and direct-conversion flat-panel imagers is on going, however this research directly involved with indirect-conversion method to obtain highest possible resolution and probably the most economic techniques to manufacture AMA panel structure. Both electrodes are

incorporated with doped a-Si:H respectively for ohmic contact purposes and top electrode (labeled ITO) is subsequently deposited on the p+a-Si layer to enable the application of a biasing potential and, thereby implied an electric field F in the intrinsic a-Si layer as shown in figure 2.3.

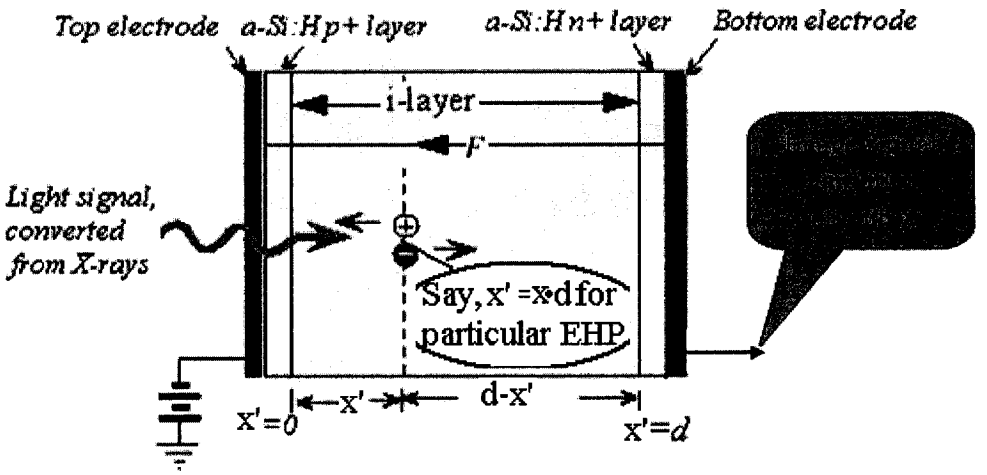

Figure 2.3: A typical models for individual a-Si:H p-i-n photodiode in pixel sensor.

The equivalent schematic of a single pixel is shown in Figure 2.4. With negative bias on A, the electron-hole pairs (EHPs) that are generated in the photoconductor by the absorption of light photons travel with/against the field lines. The charge carriers are collected by the bias-electrodes and accumulate on the storage capacitor C_{ij}. These accumulated carriers constitute a charge signal ΔQ_{ij} that are read out during self-scanning period. The x-ray generated charges ΔQ_{ij} is then collected and stored on the storage capacitance C_{st}. The TFT is switched on every Δt seconds to read out these charges on the pixel followed by a charge amplifier. The applied bias is typically several kilovolts for an a-Si-based photodiode and can be positive or negative. The negative bias shown on the

receiving electrode in figure 2.4 has the advantage that the device is self-protecting to high voltage damage.

On the other hand, if somehow large amount of charge accumulates on the pixel electrode because of high radiation exposed and thereby if voltage on C_{st} rises substantially to potentially damaging levels, the pass transistor TFT might be in danger. Because, inherently TFT has only ~50V volts beyond breakdown, whereas the applied bias is several kilovolts and more importantly, the bottom electrode is shared for both TFT and photoconductor in integrated arena. Any failure of the pass transistor into integrated large AMA system is strategically huge failure of the whole system and no easy solution so far. The resolution is primarily determined by the pixel size and available image detector is typically 1 μm with applied field of 2 V/μm. TFT and Photo-PD, although their properties are different, both can be readily prepared within one process run in large areas.

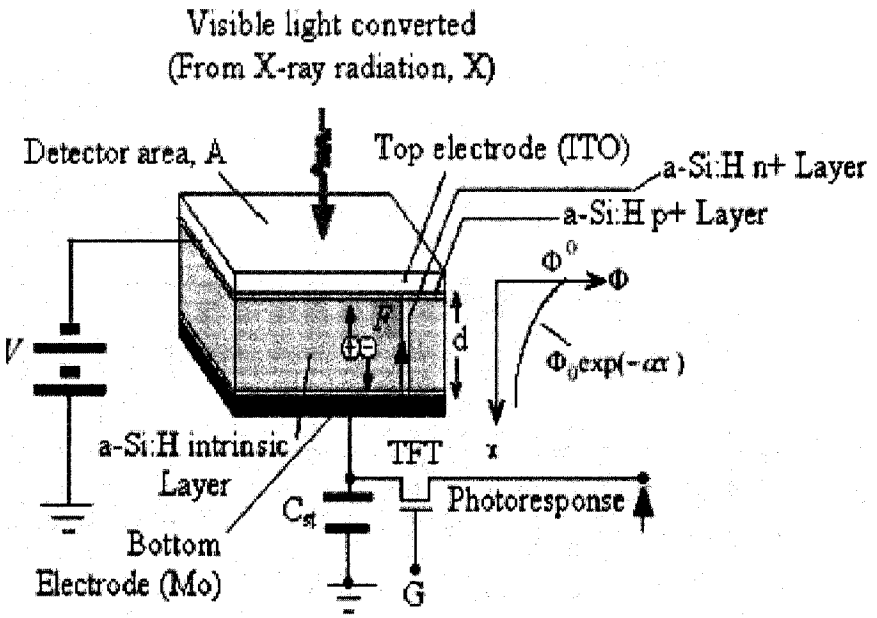

Figure 2.4: a-Si:H pixel sensor schematic and photodiode block depicted inside.

2.4 X-ray absorption and quantum efficiency

It is highly desirable in medical imaging that the photoconductor should absorb as much of the incident radiation energy as possible to minimize patient exposure [23]. The fraction of incident photons in the beam is attenuated in the scintilator and generates proportionate visible light photons. These light photons carry the object information and detected by the photoconductor. The conversion efficiency of scintillator depends on the linear attenuation coefficient of the photoconductor material and its thickness as well. The detector quantum efficiency is given by:

$$A_Q = \eta_S[1 - \exp(-\alpha d)] \tag{2.1}$$

Where, η_s is the conversion efficiency of the scintillator and d is the conductor thickness. Also, α (E, Z, ρ) is the linear attenuation coefficient of the material and it is a function of energy E, atomic number Z, and density ρ of the material. A_Q is called the quantum efficiency because it describes the efficiency with which the medium attenuates photons. The actual energy deposited into the photoconductor per unit area is then given by

$$E_{absorbed} = \int_0^{E\max} \eta_S \Phi(E) \frac{\alpha_{eN}}{\alpha(E)} E[1 - \exp\{-\alpha(E)d\}]dE \tag{2.2}$$

Where, Φ(E) is the photon fluence per unit energy, i.e., number of photons arriving per unit area per unit energy, which is the energy spectrum of the x-ray beam. The energy absorbed by a given photoconductor material can be maximized by making the detector thickness several times of the attenuation depth, δ. For indirect conversion, the initial interaction of an x-ray photon with an atom of the scintillating compounds

leads to the emission of an energetic electron from an inner core, such as the K-shell, into the conduction band being photoelectric effect.

2.5 Structure of a photodiode and image sensor

Due to the brisk advances in active matrix fabrication technology and sophisticated design technique, highly developed self-scanned displays will able to collect more data and hence reduction of bandwidth decompression circuitry. Amorphous active matrix arrayed technology has made possible the concept of flat panel imaging systems for digital radiography. The general structure of the arrayed pixel is shown in Figure 2.5 [24].

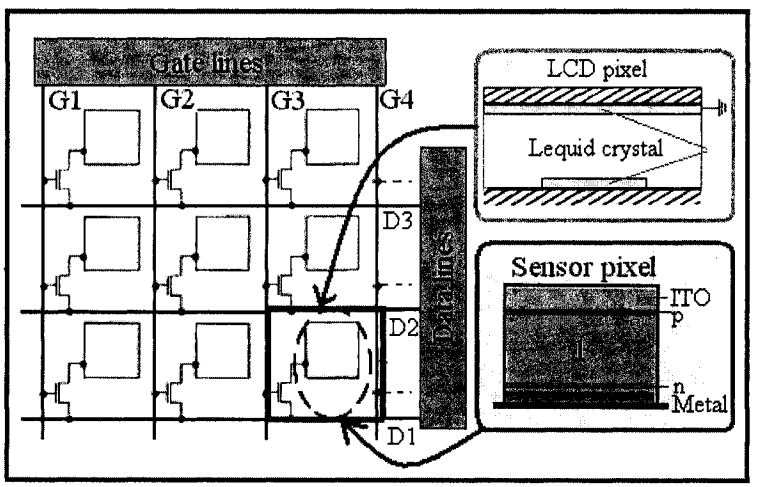

Figure 2.5: The pixel contains a-Si:H transistor and p-i-n photodiode. The sensor could be either liquid crystal instead or p-i-n photodiode. Adapted from [26].

The above structure can be used for two-dimensional sensor array with the different design of the pixel element. Each pixel occupies the intersection of a grid and data line, which is connected to a pass transistor. A voltage on the gate line activates the

pass transistors in that column allowing associated pixel to be activated. The whole array is accessed by sequentially addressing all the gate lines. Based on these principles, there have been several products already in use; for instance LCD display, scanner arrays, thin film transistor (TFT), solar cell, memory device, position sensors, photoreceptors, smart power and many more are in developing stage.

2.6 Scintillator

Scintillator works by converting x-ray energy into visible light. Fluorescence caused by incident radiation such as α, β, and γ-rays is called scintillation and the materials compound is referred as phosphors. When an optical sensor is coupled with a phosphor layer, an x-ray detector can be realized. Phosphors enable the use of x-rays to visualize objects in real time or to record a single image. The principal use of scintillator is to detect and measures the energy, position, and time of the incident radiation [25].

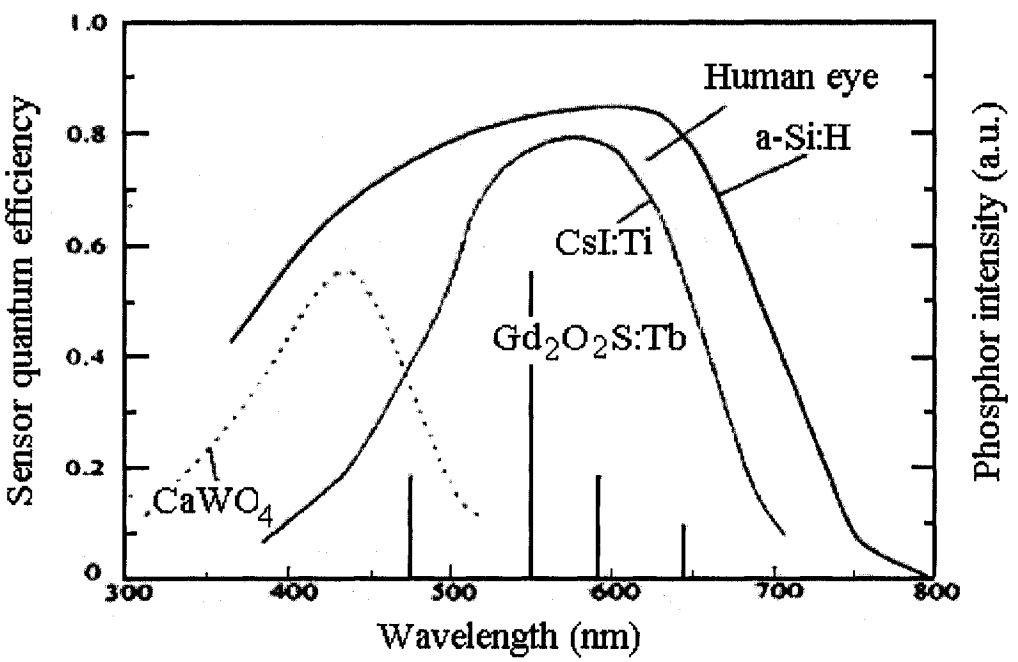

Figure 2.6: Spectral response for selected phosphor materials. Adapted from [29].

A commonly used phosphor material is P43, a commercial name of Gadolinium Oxy-Sulphide with Terbium doped (Gd_2O_2S (Tb)) compounds. It has a light decay time of few hundred microseconds, which severely limits its maximum counting rate. Other materials, such as plastics and the higher-Z bismuth germinate, $Bi_4Ge_3O_{12}$ (BGO), have well defined roles in x-ray scintillators [26]. However, Gd_2O_2S:Tb has several characteristics convenient for x-ray imaging. The light emission spectrum, which has its main peak at 550 nm, roughly confirms to the spectral sensitivity of an a-Si:H photodiode as shown in Figure 2.6. This material is neither poisonous nor deliquescent and chemically stable [27]. The thickness of the phosphor layer is determined by the trade-off between detection efficiency and spatial resolution [28].

2.7 Medical applications

Indeed, digital radiology promises portable, versatile, and easy going imaging technology. However, digital radiography has started to make inroads. Once an image is digital, it can easily be made available in multiple locations simultaneously. It can be transmitted over long distances in real-time. Digital images make possible computer-assisted diagnosis. Digital images, video sequences and even volumetric data sets are easily linked to a patient's electronic record. Many medical modalities, such as CT, PET, SPECT, MRI and ultrasound are inherently digitals.

The oft-touted advantages of digital radiography tend to stress its faster throughput and easily accessed to archived resource. Also the ability to permit digital storage and communication within the hospital and beyond facilitated with computer-aided diagnosis and "second opinions" to the remote users. Perhaps most importantly, the

possibility of improving image quality without increasing patient x-ray exposure by virtue of enhanced detective quantum efficiency.

Complex imaging procedures such as dual energy and tomographic data acquisition, which improve the busy clinical environment by capturing the images in digital means, especially once it used in mammography and fluoroscopy. Technological advances of second generation and already in process of hybrid FPD systems should solve many current issues. But the question is "how much they can do", answer is "certainly better". They are certainly worth consideration for replacement or new implementation of an imaging suite for even pediatric-fluoroscopy [30].

2.8 Summary

This chapter attempted to expound some important use of hydrogenated amorphous silicon and the way they work. Advances pertaining to commercialization are frequently not published and the critical advances relate to process yields. As an initialization of device level technology, the general description and some primitive theory of amorphous semiconductors are discussed. In addition, present status of development of flat panel detectors and their clinical applications in the world have been surveyed, and future trends are also explored. A broader look into FPD for various medical use and radiological advancement are taken under microscopic focus. It's our opinion, flat-panel detectors are poised to be a unifying concept in x-ray medical imaging as they promise to greatly simplify the acquisition, interpretation, storage, and distribution of x-ray images, all in a same token.

Chapter 3: Hydrogenated Amorphous Silicon Band Physics and p-i-n Layers Deposition Techniques

3.0 Introduction

This chapter describes overall background information on the physical properties of hydrogenated amorphous silicon (a-Si:H). Since transient response extractions are intimately related to the carriers transportation, an imperative part in this chapter is therefore discussed on theory of carrier conduction in amorphous silicon. A clear understanding of the band structure, follow suit irradiated pattern, and resultant energy band models is a prerequisite for entering to device level modeling.

Table 3.1: Electrical properties; a comparison between crystalline silicon and amorphous silicon.

Parameters	c-Si	a-Si:H
Structure	Diamond	Random network
Band gap energy (eV)	1.12	1.6 ~ 1.9
Band transition	Indirect	Direct
Interatomic distance (Å)	2.35	2.35 ± 0.07
First bond angle (°)	109.47	109 ± 1 0
Density (gm/cm^3)	2.3	~2.25
Resistivity (Ω-cm)	$<10^5$	$<10^9$
Electronic mobility ($cm^2V^{-1}S^{-1}$)	1350	1 ~ 2
Hole mobility ($cm^2V^{-1}S^{-1}$)	480	0.003 ~ 0.0007
Permittivity	11.9	~11.9
Electron diffusion length (μm)	300	<10
Hole diffusion length (μm)	200	~0.1
Average life-time of electrons (S)	2.5×10^{-3}	10^{-6}
Average life-time of holes (S)	2.5×10^{-3}	10^{-6}

A theoretical framework for understanding the materials properties can be derived by applying quantum mechanical analysis to the bonding arrangement of the atoms.

However, band-model for amorphous semiconductors can be plagiarized by comparing their similarities to crystalline counterpart and thorough observation of their electronic and optical properties all in a same token. Physical properties of a-Si:H are reviewed and compared with those of crystalline solids in Table 3.1.

3.1 Fundamental concepts of amorphous semiconductors

The anarchy of the atomic structure is the main feature, which distinguishes amorphous from crystalline structure. Because the atom orientation in solids dictate the physical properties and thereby tell apart whether the solids would be semiconductor, amorphous, or something deviated products. Widely known Bloch's theorem is direct consequence of the periodicity and describes the electrons and holes by the wave functions, which are extended in space with quantum states defined by the momentum. The structural disorder influences the electronic properties in several ways, which are discussed latter in this chapter. Structural defects such as broken bonds and the possibility of alternation bonding configurations are synthesized; eventually those broken/alternative bonds lead the metastability phenomenon.

3.2 Atomic structure in Amorphous Solids

This section explains the general atomic structural band views in amorphous solids. An Amorphous solid is one in which there is no long-range order in the position of the atoms. But lack of this long-range order in amorphous materials makes it difficult but not impossible to determine its exact band model. Fortunately there have been few theoretical band models available already, which facilitate us to describe the local

structure of an amorphous material in terms of degree of order. This structural ordering has a definite hierarchy: short-range, intermediate-range and long-range order [31, 32]. A solid consists of a three dimensional network of atoms interconnected by atomic bonds. These bonds consist of interactions between the wave functions of the outer shell, or valence electrons of the atoms when they are brought close together to form a solid.

In semiconductors, atomic bonds are formed when two or more atoms share their valence electrons to complete the sub-shells of each atom. This type of bond is known as a covalent bond, and the number of nearest neighbors for a given atom in the solid is known as the coordination number of that atom. This key information should provide an underpinning basis for further study of the structure of hydrogenated amorphous silicon. Since the subject of crystalline semiconductors has been more extensively pursued and is indeed better understood. Therefore many parallels and distinctions between crystalline and amorphous semiconductors will be walked around.

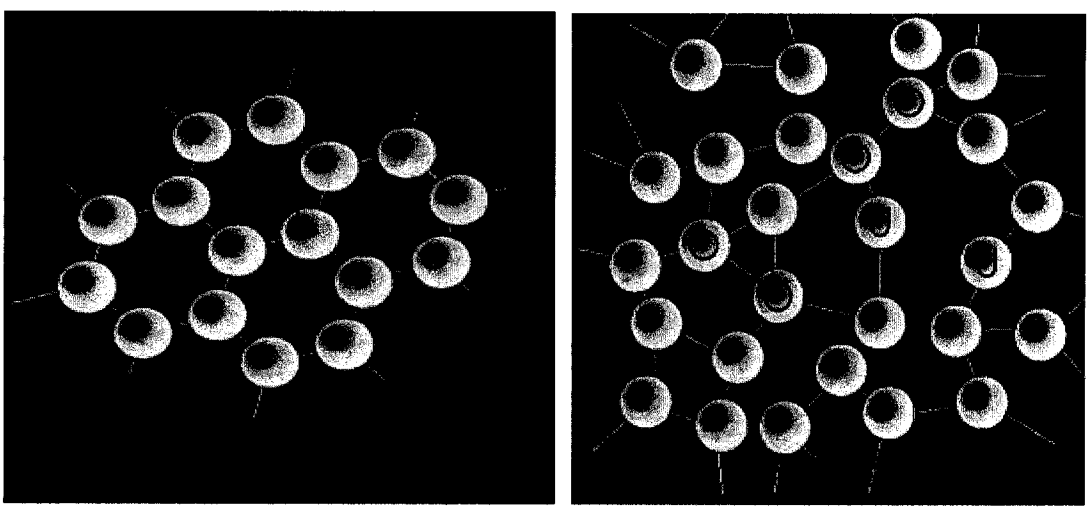

Figure 3.1: A two-dimensional representation of a three-fold coordinated atomic structure is shown for (a) Hypothetical crystalline semiconductor and (b) Amorphous semiconductor. Adapted from [24] and *et al* Bud J Fogal MSc thesis, (2005).

The crystalline and counterpart amorphous bonding arrangements for semiconductors are illustrated two-dimensionally in Figure 3.1. The black-shaded dots in the two diagrams indicate the equilibrium positions about which the atoms oscillate. In a crystal, all of the bond lengths and angles are identical throughout the material disregards surface dangling states. The result is the periodic structure depicted in Figure 3.1 (a). An amorphous solid, on the other hand, has slight detour predominantly in the bond angles which completely destroy the renditional periodicity for distances after a few atomic radii or vice-versa. This sort of disorder is known as topological disorder.

However, the disorder in the network introduces localized electronic traps, where the electron wave function is localized to particular states in the semiconductor. The valency requirements are satisfied for each individual atom in the structure, and each atom is normally bonded to the same number of nearest neighbors. The energy location and density of these localized trapped states have an acute impact on the electronic and optical properties of amorphous semiconductors. An elementary defect of an amorphous semiconductor may be considered so called coordination defect where atom has less or more bonds than that of the balance morphology. Under-coordinated atom is depicted by inserting letter 'U' on the atom and 'O' for over-coordinated defect in depicted in Figure 3.1 (b).

3.3 Amorphous semiconductors band models

The band model is an important tool in solid-state physics that can be used to explain the electronic and optical properties of semiconductors. It is an exciting time to undertake theoretical studies of amorphous semiconductors. Since the pioneering work of

Anderson [33] and Mott [34], considerable efforts have been taken place on the observation of electronic localization in disordered solids. In the parlance of amorphous semiconductors, the nature of the carriers localization are determined by the microscopic structure of the band-tail and mid gap states as well as the dependence of this structure as on the energy of the gap states.

In a single atom system, quantum theory insinuates that the energy of the carriers is quantized into discrete energy levels or states. When atoms form a solid, the electron energy states associated with the individual atoms combine in such a way to form almost continuous bands of allowable energy states. These band states are described by a well known function called the density of states, which denoted by $g(E)$ and demarcate the number of carrier states per unit energy per charge at energy E. As mentioned before the first attempt headed for expansion the theory of crystalline semiconductors to encompass amorphous semiconductors was taken by pioneer Mott [34], who distinguished that in all crystals the electronic structure has certain complete features:

- The individual electrons are described by Bloch wave functions that are extended, with long-range order both in phase and amplitude, and
- The corresponding energies fall into bands of allowed levels that are separated by energy gaps with sharp edges.

According to the N. F. Mott, the Bloch wave functions for the amorphous solid have long-range order in their amplitudes, but only short-range order in their phases. The lack of long-range order in the phases of the wave functions smears the sharp band edges of the crystal replacing them with tails of localized states in the amorphous semiconductor. Translational and compositional anarchy were assumed to cause

fluctuations of the potential of sufficient magnitude to produce localized states, which extend into the energy gap of the material. These localized states were not allied with imperfection, and assumed to be a product of the randomness of the potential. The transition from localized to comprehensive states leads to an abrupt change in the mobility of charge carriers in the material.

The density of states model for an amorphous semiconductor as predicted by Mott is illustrated in Figure 3.2(b), which is quite analogous to its crystalline counterpart as shown in Figure 3.1(a). The prevalent features of the band diagram in Figure 3.2(a) are the two bands of allowed energy states separated by a precise forbidden gap. The lower band is fully occupied by the electrons involved in the covalent bonding of the semiconductor and is called the valence band. The upper band of states, however, is almost completely free of electrons. When an electron acquires sufficient energy to surpass the band gap, it becomes free to contribute to an electrical current and the band widely known as conduction band in semiconductor physics.

The band model originally proposed by Mott and latter adapted by CFO model, where CFO stands for three famous names (Cohen, Fritzsche, and Ovshinsky) of those who were presented the model as depicted in Figure 3.2 (c) [35]. The greater degree of disorder assumed in the CFO model would lead to band tails, which extend throughout the mobility gap of the material and overlap nears the Fermi level. The structure of amorphous semiconductors also contains atoms that are coordinated differently from the normal structure bonding (NSB) of the network. Since the connectivity of the amorphous network is not well defined on a local basis, obvious defects may subsist in the structure

such as dangling bonds, chain ends, vacancies, interstitials, substitutional impurities and may lead unusual electronic configurations.

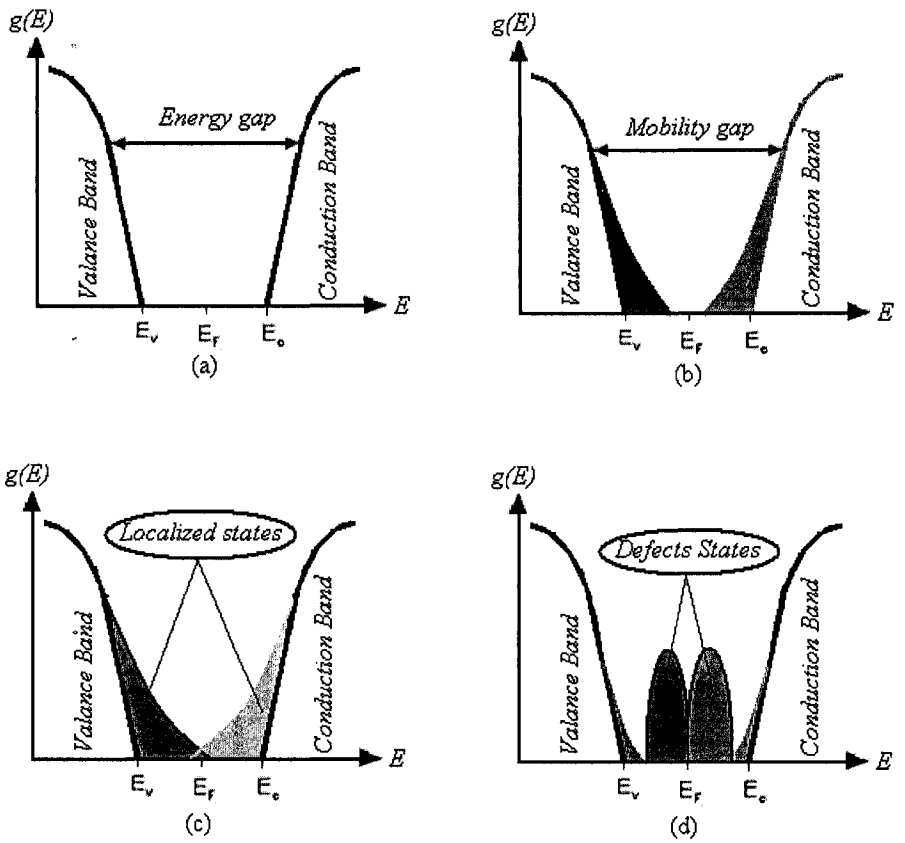

Figure 3.2: Amorphous density of states reported models (a) Crystalline Model (b) Mott model (c) CFO model (d) Marshall and Owen (MO) model.

Figure 3.2(d) depicted the density of states model proposed by Marshall and Owen (MO) with localized mid-gap states commence the defects [36]. This model suggested that the position of the Fermi level is decisive by bands of accepters and donors in the lower and upper halves of the mobility gap respectively. The hydrogenation of amorphous silicon serves to significant reduction of the number of localized defects. Therefore, hydrogenated bonds or band structures have also been discussed for better understanding of amorphous morphology and engineered use.

3.4 Hydrogenation impacts on highly disordered a-Si:H

The way of manufacturing of hydrogenated amorphous by plasma deposition techniques and its subsequent product is not always perfectly structured, rather ambiguous i.e., the fabricated amorphous is very much process dependent. Plasma deposition from SiH_4 gas heavily diluted in H_2 also results in nc-Si:H films where nanocrystals are either abutted against each other or embedded in an amorphous matrix. Chemical annealing has been proposed as a mechanism where H aids crystallization by annihilating the strained Si–Si bonds in the a-Si:H film [37, 38].

The chemical reactions and transport phenomena observed during the molecular dynamics (MD) simulations (see Figure 3.3) of H impingement on a-Si:H films include: (i) H adsorption onto the surface; (ii) Surface H abstraction by the impinging H atoms; (iii) Insertion of H into strained Si–Si bonds; (iv) H diffusion into the bulk substrate/film; (v) Sputtering of surface H atoms; and (vi) Desorption into the gas phase of H from surface silicon hydrides with over-coordinated Si atoms [39].

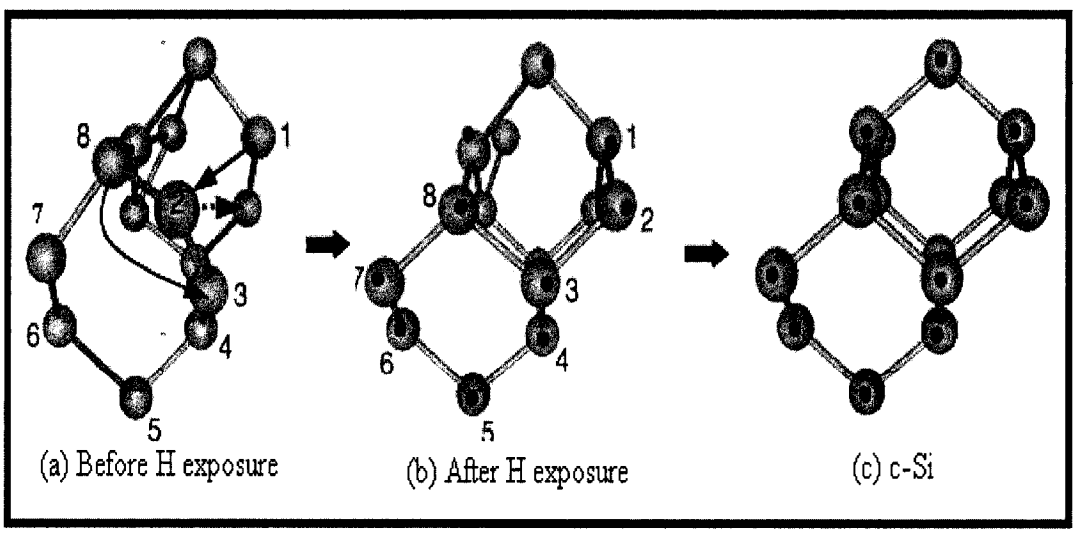

Figure 3.3: Hydrogenation effect in a-Si films (simulated) and structural evolution.

The structural evolution in the transformed regions as a function of the H-exposure time reveals that the amorphous-to-crystalline transition is mediated by relaxation of strained Si–Si bonds as a result of H insertion into these bonds. During diffusion through the film, H inserts into strained Si–Si bonds, forming intermediate bond-centered Si–H–Si configurations [40, 41]. After the H moves away from the bond-centered location, the strained Si–Si bonds break or relax, then undergo local structural rearrangements that result in bond lengths and angles closer to those of c-Si.

3.5 a-Si:H band model: n-type, p-type and p-i-n structure device

The observation of electronic doping development of amorphous semiconductor set the stage for developing of hydrogenated amorphous silicon electronic devices. The disorientation of atoms in amorphous materials has an effect on the electronic states in many ways. The density of states distribution is widened compared to its crystalline counterpart by tailoring the states, which are referred as localized states. For the amorphous material, it is replaced by an energy-dependent density of states distribution *N(E).*

The tight binding model illustrates the splitting of molecular orbital in the bulk material. The s and p states combine to form the sp3 hybrid orbital of the tetrahedral silicon bonding as shown in Figure 3.4. These states are split by the interactions involved in bonding to produce the valence and conduction bands. Nevertheless, the silicon orbital which is not involved in bonding (for instance dangling bonds), are not split by the bonding interaction and lead to states lying in the forbidden gap and thereby evolves

defects. After keen observation of Figure 3.4, one can easily found two distinct differences, which may explain and concludes as follows [42]:

- In crystalline silicon, the tight-binding bonds of yield distribution of states diagrams are so specific in such a way that s, s-p, and p states are quite distinct, where as, in amorphous silicon, those states become blurred together.
- In amorphous silicon, the band tail states extend into the mobility gap and these band tail states have a profound effect on the amorphous material. Due to presence of hopping states in mobility gap, the transition between valance band to conduction band no longer discrete in amorphous, rather followed successive trapped-release transition fashion, which eventually conserve photoelectronic use.

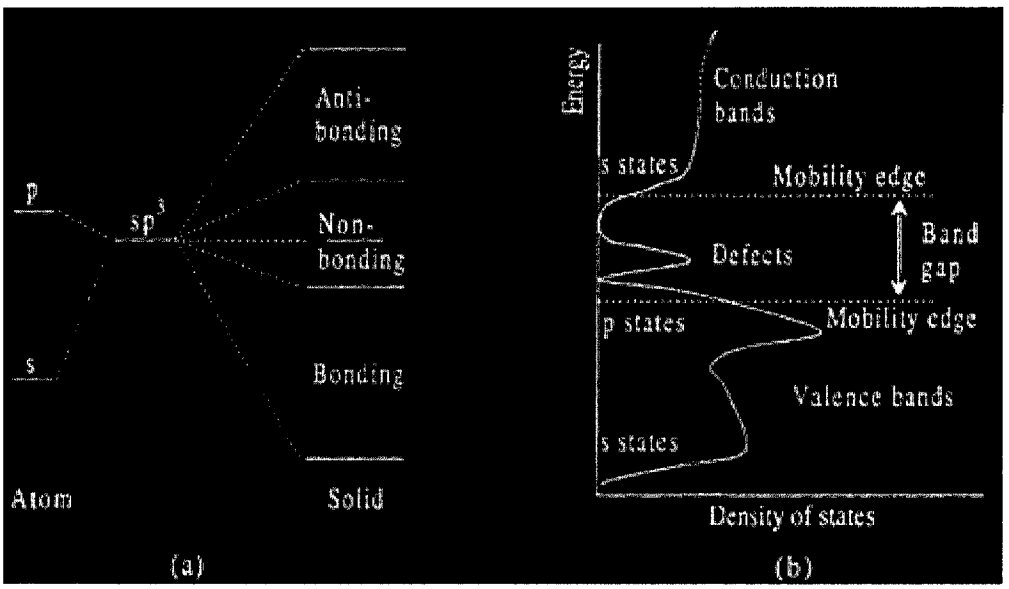

Figure 3.4: The tight binding model applied to amorphous silicon [43]. The molecular orbital model appears in (a). The density of states distribution arising from the molecular orbital is shown in (b).

Although there is still debate how amorphous silicon actually bonded, the most researchers and their experimental data indicate that the Figure 3.4 is a fair estimation,

especially for low defect density of states so far. This situation anticipated previously discussed 8-N rule for bonding. The common feature is that the lowest energy departure from the ideal network takes form of a charge pair of defects. These are $(p_4^+ + D^-)$ in singly doped a-Si:H and perhaps $(p_4^+ + B_4^-)$ in compensated a-Si:H. However, the chemical bonding arguments expressed by the 8-N rule do not allow singly occupied states, rather consequently low Fermi energy evolved.

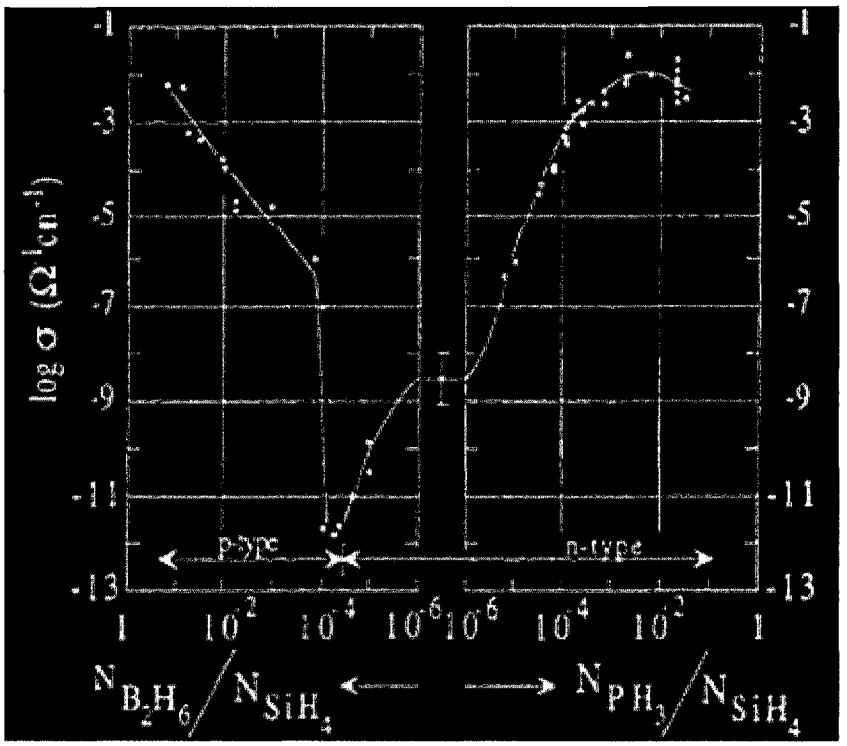

Figure 3.5: The room temperature conductivity of p-type (on the left) and n-type (on the right) samples of a-Si:H. The central part of the graph refers to compensated material (Spear and LeComber 1975).

There are basically two mechanisms for the motion of charge at non-zero temperatures: hopping in localized states and transport via extended states. For n-type samples with moderate levels of phosphorous doping, the transport is predominantly by

electrons in extended states [40]. Eventually, the conductivity is said to be thermally activated leading to the conclusion that transport is occurring mainly through extended states and for moderate levels of doping, the conductivity is obviously thermally activated. Figure 3.5 compares the room temperature conductivity of various n- and p-type a-Si:H samples [41, 44].

The p-type samples got lower conductivity than n-type, mainly because the wider valance band tail keeps E_F further from the mobility edge. For very small variation in doping level, substantial change in the magnitude conductivity is reported [24]. The Figure 3.6 (a) shows a typical p-i-n structured a-Si:H band model and Figure 3.6 (b) showed its generalized density of states (DOS) with trappings as used in imaging pixel sensors. However, instead of abrupt band edges, a-Si:H has broadened tails of states extending into the forbidden gap as depicted Figure 3.6 (b).

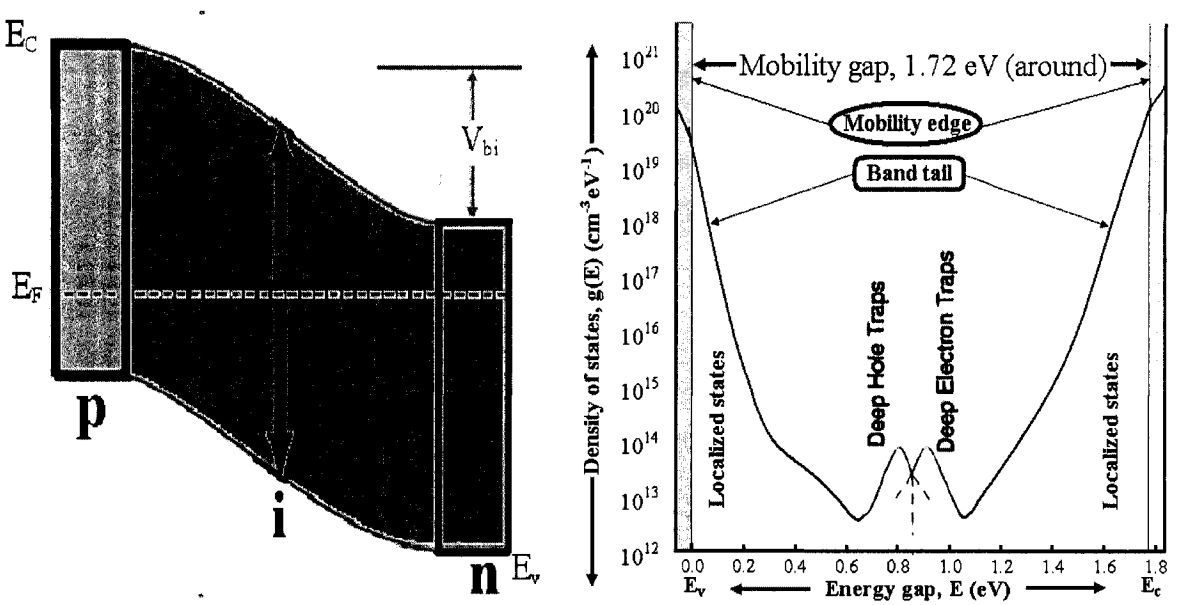

Figure 3.6: (a) Schematic band diagram for a-Si:H p-i-n photodiode (b) Density of states in side mobility gap of a-Si:H.

These band tails originate from the long range bonding disorder, and affect the electronic transport in the material. Tunneling transitions occur in these localized states, which provide for hopping conduction in the band tail and the coordination defects generate deep defect states inside the band gap. The deep defects change the electronic properties of the material by controlling the trapping and recombination of carriers. Customarily, the inclusion of 10% hydrogen in the film is considered as an optimum ratio to achieve high quality amorphous silicon films.

In addition, external excitation such as light illumination and current flow can cause a reversible change in the density of states. This phenomenon is called 'metastability' and its the ability of a non-equilibrium state to persist for some period of time. Probably the most widely studied metastability in a-Si:H is the Staebler-Wronski effect, in which additional localized states are created by light irradiation [45]. This effect decreases the photoconductivity and increases the dark conductivity of a-Si:H, meaning the dark current increase by increasing conductivity, which (dark current) is not expected in imaging technology. The easiest and popular technique to remove metastable degradation effect is annealing by the sample in temperature between 150 ~200°C.

3.6 Deposition techniques for a-Si:H

While a-Si:H yields good results at relatively higher x-ray energies with thicker active layer, but the detection efficiency degrades remarkably once reducing active layer that are obvious for flat panel use. Therefore, a bit compromise and trade-off optimizations are involved. But no alternative solution on inherent properties, except the improvement of deposited film quality and hence meet up future challenges.

3.6.1 Growth Mechanism of a-Si:H

Plasma Enhanced Chemical Vapor Deposition (PECVD) techniques are generally deployed for thin film active layer fabrication. PECVD yields low defect density and has become the industrial standard. Although the principle of the deposition is quite simple; the physical and chemical process which take place are exceedingly complex, and the difficult to identify the dominant reaction paths from the many possibilities. Silane (SiH_4) is decomposed in the chamber in the presence of plasma. The process pressure is set by a control system to maintain the plasma. Ions and other reactive species in the plasma condense on a heated substrate (200°~300°) to form an amorphous film with incorporation of hydrogen in the film. A schematic of the plasma source used in the PECVD experiments is shown in Figure 3.7 and adapted from [46].

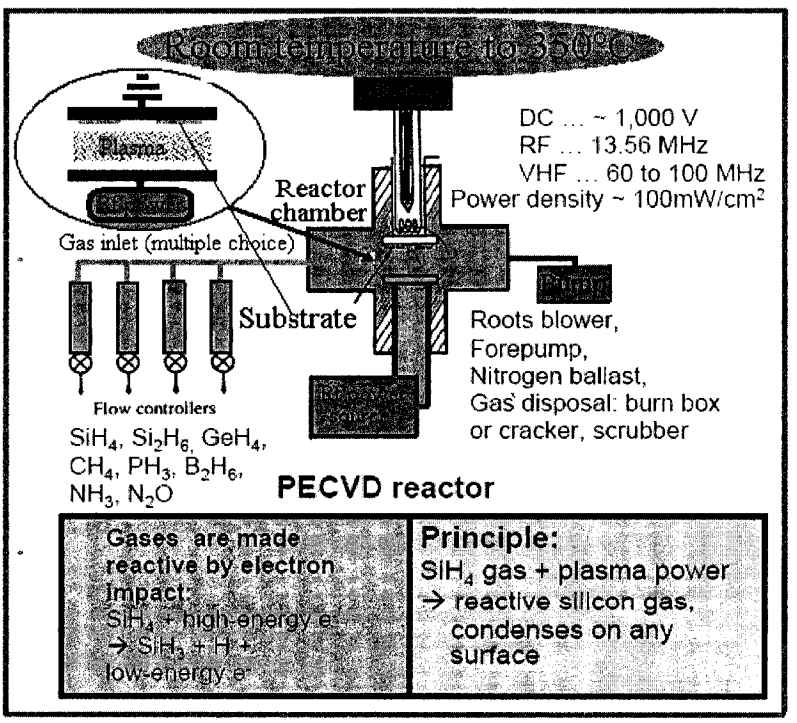

Figure 3.7: Layout schematic of Plasma Enhanced CVD (PECVD) techniques for amorphous silicon deposition.

The growth of a-Si:H can be categorized as under [47] :

- Gas-phase process: they engross radicals in the glow-discharge plasma and radicals to the film-growing surface. The gas-phase process determine the arriving species on the film growth surface, and can be controlled by many external parameters such as the type of source gas, gas pressure, gas flow rate, power frequency, and power density.
- Surface reactions on growing surface: It is controlled by temperature and the arriving species, which determine the resulting micro-structure of the films. There are several successive reactions; main reactions associated with film growth are given as under:

  $SiH_4 = SiH_3+H$; $SiH_3 = SiH_2+H$; $SiH_2 = SiH+H$; $SiH = Si+H$

Table 3.2: Operational measures/geometry of various events in formation of a-Si:H [48].

Events	Defect density	Hydrogen Concentration	Deposition Rate
Temperature ↑ (200°~ 300°C)	Minimum at 250°C	↓	↑
Rf power density ↑	↑	Maximum at about 10 mW/cm^2	↑ (with high gas concentration)
Gas concentration (SiH_4+Ar)/SiH_4↑	↓	↑	↑
Process pressure (0.1 ~ 0.5 torr) ↑	↓	↑	↓

Although the deposited intrinsic a-Si:H is not really an ideal intrinsic semiconductor. Its dark conductivity activation energy is less than half of the optical gap and it shows a slightly n-type electrical behavior due to the density of tail stated near the

conduction band and more electrons available as a result. The effect of deposition parameters on i-a-Si:H quality and rate are given in Table 3.2.

Table 3.3: PECVD deposition parameters for amorphous silicon.

Layer Type	n^+-Layer	i-Layer	P^+-Layer
Source Gas (SG), and flow rate	SiH_4 : 40 sccm PH_3 : 8 sccm	SiH_4 : 40 sccm	SiH_4,: 40 sccm B_2H_6: 15 sccm CH_4 : 90 sccm
SG pressure	300 mTorr	300 mTorr	300 mTorr
RF power	5 Watt/cm^2	7 Watt/cm^2	5 Watt/cm^2
Heater temperature	320°C	320°C	250°C
Growth rate	27 nm/min	38 nm/min	27 nm/min

Argon (Ar) dilution is also included with low concentration. The deposition temperature is about 250°C and an rf power density is about 10 mW/cm^2 for low defect density and high hydrogen concentration in the process. The deposition pressure is about 0.1 ~ 1 torr to minimize the voltage necessary to maintain required plasma state. It maintain adequate defect density about 10^{16} cm^{-3}, the hydrogen concentration should be maintained within the range around 10% ~ 14% [49]. For silicon deposition the feedstock is of SiH_4 and other gas species as given in Table 3.3.

3.7 Layers characterization in a-Si:H p-i-n photodiode

A p-i-n structure photodiode comprised multiple layer interfaces as shown in Figure 3.8. The metals that are used in p-i-n photodiode are Molybdenum (Mo) and Indium Tin Oxide (ITO). The amorphous semiconductor is sandwiched between those metals. The fabrication process of schottky interface starts with the sputter deposition of Mo on a glass substrate, which acts as the bottom electrode. Followed by molybdenum

sputtering, PECVD employed to be deposition n+ a-Si:H on top of bottom electrode. Here creates first schottky diode. Due to structural advent and added doped amorphous layer, those diodes act as an ohmic contact, or simply we referred it as schottky interface.

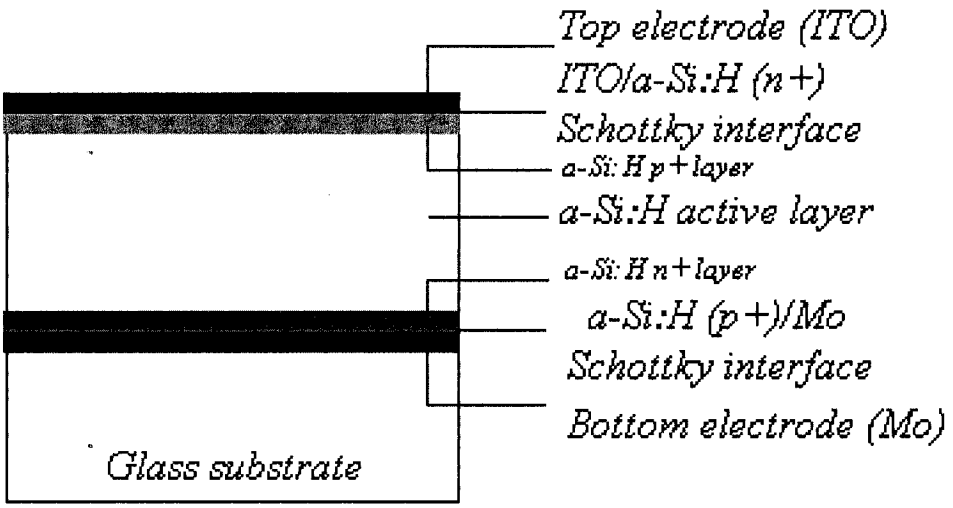

Figure 3.8: Schematic diagram of a-Si:H p-i-n diode interfaces.

On continuation amorphous silicon deposition in order to fabricate p-i-n photodiode, a-Si:H and p+a-Si:H are immediate layers deposited consecutively in a single pump down at 260°C by controlling reactant species gas through gate valve operation as shown in Figure 3.7. The final metal Indium Tin Oxide (ITO) deposited on top of p+a-Si:H layer for top electrodes and creates second schottky interface. It is deposited by sputtered techniques and act as top electrode (Figure 3.8). The inherent properties of ITO are optically conductive and electrically as well. Therefore, it is very useful and popular option in indirect x-ray imaging technology.

The top electrode material selections should be based on matching ability to the amorphous silicon and permissible ability to light absorption, holes ejection, and the

intrinsic mechanical stress. In ITO/a-Si:H Schottky interface, light photons are absorbed in the a-Si:H and the generated e–h pairs are collected by the contacts. There are three transport mechanisms underlying the reverse current in metal/a-Si:H contacts [50][51]. Those are mainly named as thermionic emission, thermally assisted tunneling, and field emission. Thermionic emission refers to transport of thermally activated carriers over the top of the Schottky barrier into the a-Si:H conduction band where the conduction band edge intersects with the interface. Thermally assisted tunneling refers to transport of carriers tunneling through the Schottky barrier. Field emission refers to the direct transport of carriers from the Fermi level of the metal to the conduction band of the a-Si:H [52].

The leakage current density considering all these contributions (emission) have already available in previously reported works [53, 54]. Nevertheless, secondary ion mass spectrometry (SIMS) can be implied to measure diffusion of oxygen into a-Si:H, though it is inevitable even when the ITO is deposited at room temperature. The oxygen atoms inside the a-Si:H layer act as donor-like defects and increase the density of ionized defect states, which consequently increase the leakage current and reduce the photosensitivity.

The dark current of the annealed sample is much larger than that of other samples and increases exponentially with bias voltage. The values of the density of surface states and the density of defect states increase approximately by an order of magnitude after annealing at 260°C, which is indicative of oxygen diffusion in these devices. Photodiodes based on ITO/a-SiNx:H/a-Si:H MIS structure, with a thin a-SiNx:H between the ITO and the a-Si:H layers, are an alternate solution to prevent the diffusion of oxygen [55, 56].

3.8 Summary

This chapter endeavors some imperative bond structure of hydrogenated amorphous silicon and deposition techniques. The a-Si atomistic structure, band theory, doped structure, and conductivity of amorphous semiconductors has been illustrated. The structural stimulation and bond realignment by hydrogenated effects has been discussed and configured thoroughly. A band model for individual doped impacts on a-Si:H p-i-n device and some essential feature of the electrical transports in n-type a-Si:H was also discussed. Crucial aspects of the p-i-n band model and doped engineering of a-Si:H photodiode were introduced. The deposition techniques related to a-Si:H p-i-n photodiode fabrication in layer basis have been addressed. For deposition of intrinsic hydrogenated amorphous silicon, PECVD techniques are recommended, and the doped hydrogenated a-Si can be deposited adding subsequent doping gases in one single machine run. On the other hand, for electrodes depositions by sputtering techniques has discussed. The top electrode ITO selections and its characteristics have also been discussed in terms of the opto-electrical measure. The fabrication issues include the film growth mechanisms, the optimization of process variations on the quality film and relevant events are discussed and will be shared later in appendix G for realization of p-i-n photosensor in limited manner.

Chapter 4: Numerical Modeling of photodiode transient photoresponse in a-Si:H pixel sensor and Model Based Customized simulator design/verifications

4.0 Introduction

Diagnostic radiographic imaging is one of the cornerstones of today's revolution in medical science and technology. With the drive towards portable and multimedia radiographic imaging into medi-equipment era, researchers are increasingly faced with the challenge of bringing the x-ray vision infrastructure directly to the medical professionals providing seamless access to vast quantities of information. Whether it is the transfer of an image signal from a digital camera to a laptop computer or the communication of data within a massively parallel computer, there is an urgent need to develop the versatile sensor devices for x-ray imaging. The next wave of change, however, will derive from the merging of medical imaging with multimedia technology [57].

Crystalline and polycrystalline semiconductors are main materials used in the standard CMOS technology. Amorphous are rarely used in these technologies. On the other hand, in the standard CMOS technology, there is no amorphous layer (such as amorphous silicon) option in Cadence Virtuoso layout environment; but those materials are emerging and proven materials for x-ray detection medical imaging purposes. So, when researcher/manufacturer attempt to deal with these sorts of materials, they have no other choice rather lab experiments on trial and error basis. As a result they have to spend a lot of times, efforts and money to meet certain design goals. In that context, we would like to present a novel simulation techniques, a material based customize simulator that

can be used to manipulate design parameters of a device in various mode of operation so that one can start their fabrication before available distinct designed model portfolio. Main objective in this chapter is to model a photosensor for x-ray imaging pixels that are characterized by novel customized simulator and described detail guidelines in fabrication process for the amorphous silicon (hydrogenated) photodiode. Also, we consider thin film transistor (TFT) and storage capacitor integration with a-Si:H photodiode so that a versatile transient photoresponse can be ready for digital image processing.

In medical diagnosis, usually requires high-quality video imaging. Low delay and high bandwidth are crucial to remote diagnosis treatments for health professionals, those who use teleradiology technology. Indeed medical diagnosis requires high-quality video imager as the systems are to support clinical decisions and professional upgrading required access to a wide array of highly visual material. Easy and rapid access to a reservoir of rich archival, visual information is critical to successful use, especially in clinical decision-support systems with professional upgrading. Therefore, further study and suggestion are being included for the possibility of broadband based tele-radiology so that the professionals could get access on it from anywhere anytime in the world [58]. But front-end technology not yet been ready. Our efforts are to contributing upon those frond-end supports so that the systems can initiates.

4.1 Device orientation

Thin a-Si:H p-i-n photodiodes coupled to suitable TFT and storage capacitor with scintillators are modeled in here to be suitable for detecting charged particles,

carriers, and x-rays. An important and relatively easy way to characterize photosensor devices is to measure the photocurrent while they are into a sensing device. Our presented device model is shown in Figure 4.1 and it is based on several transport mechanisms, like drift through the intrinsic region and tunnelling at the p-*i* interface.

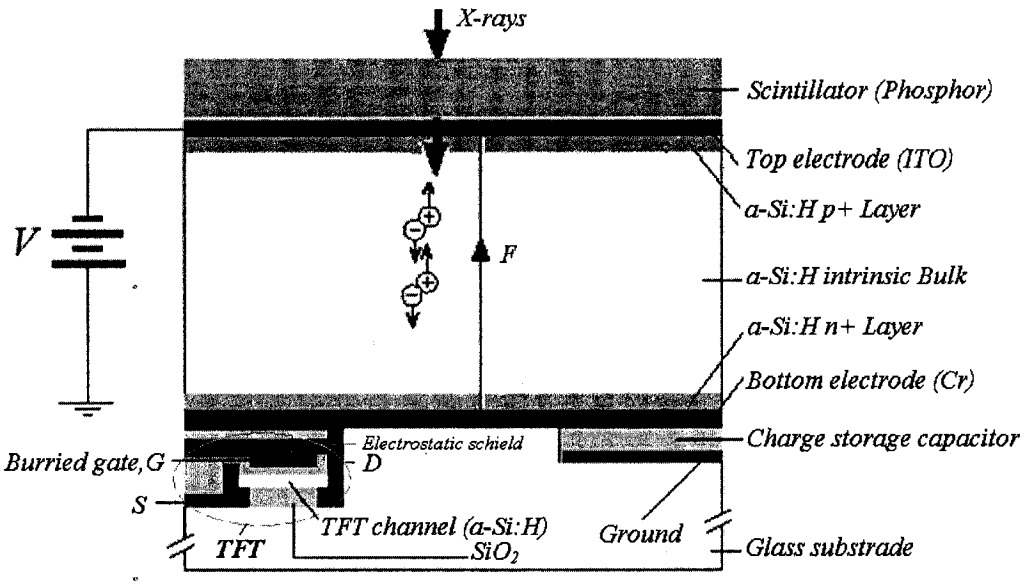

Figure 4.1: Proposed model for a-Si:H x-ray imaging pixel unit.

This device model uniquely ensured about 100 % fill factor (FF). The fill factor indicates the size of the light sensitive photodiode related to the surface of the pixel. Because of the extra electronics required around each pixel, therefore the "fill factor" tends to be quite small, especially for active matrix sensors which have more per pixel circuitry. For instance, switch TFT, storage capacitor, and the bias lines etc all are integrated into one pixel. In our device model, the switch TFT and storage capacitor are placed underneath of the photodiode so that all the incoming light photons can be interfaced with photodiode at first and thereby enhance the FF. This approach is adapted

from reported work but in prototype manner, because reported model could not ensure good FF, al least understandable from Figure 1.5 [15].

At present, it is generally accepted that the photocurrent at reverse bias is driven by generation of electron-hole pair processes in the intrinsic region considering the defect density uniform all over the active (intrinsic) region. But the density of defect states is not spatially uniform due to the non-satisfied dangling bonds. The defect states play a dominant role in the electrical properties of a-Si:H. There is substantial evidence that thermal equilibrium processes determine the density of dangling bond states [59, 60]. The defect density is correlated to the Urbach energy [61], which described the defect creation mechanism involves the breaking of weak Si-Si bonds.

The calculation of the DOS in a-Si:H requires a thorough analysis of all chemical reactions involved in the conversion of weak bonds into dangling bonds. Due to the disorder of the amorphous network, the dangling bond states can take place in a range of energy levels, resulting so-called 'defect pool'. Many researchers have worked on the development of a defect-pool model [62, 63]. One of the most precise descriptions presented by Powell and Deane [64] and thereby demonstrated the important role of hydrogen in the equilibration process. In our work, we have been follow suit similar model to calculate the defect distributions to optimize overall responses.

4.2 Design physics of a-Si:H Photodiode in x-ray imaging pixel arena

The potential use and principle have already been described in chapter 2 and 3. One particular design of arrayed structures under development consists of a regular two-dimensional pattern of pixels. Each a-Si:H pixel integrated with a photodiode, a TFT pass

transistor and a storage capacitor, which detects the incident post object informative x-ray photons indirectly.

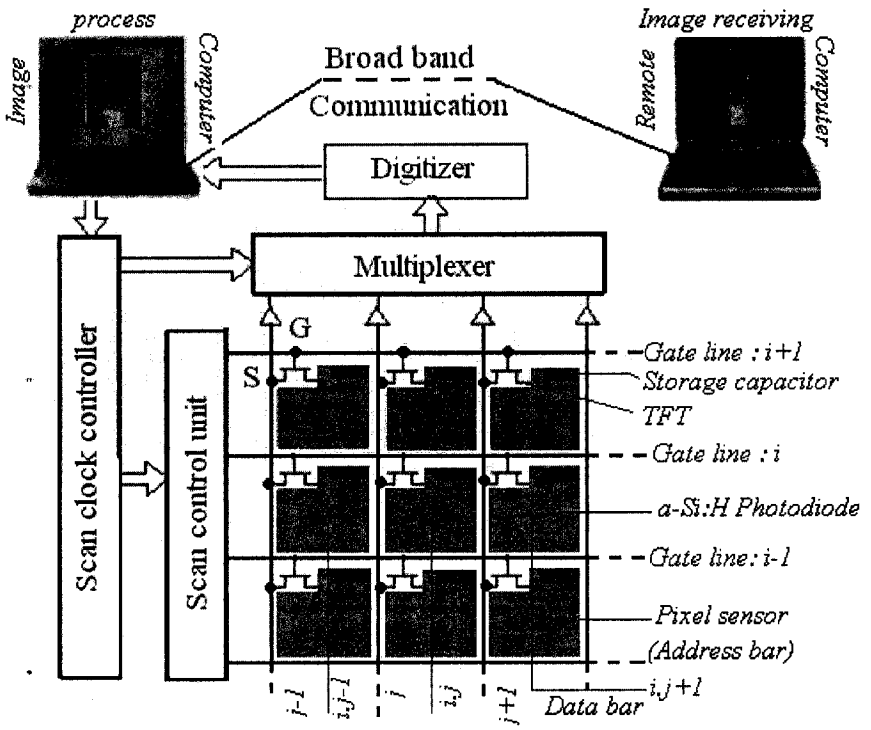

Figure 4.2: Active Matrix Array (AMA) with self-scanned peripheral electronics and remote analysis option. Adapted from [10, 22].

The a-Si:H pass TFT allows readout of the charge information stored in the photodiode. Currently this design structure as arrayed system on chip (SoC) allows us to realize real-time digital x-ray imaging over a large area with resolution as high as possible. A useful strategy in the development of such a-Si:H arrays are characterization of the properties of the individual devices which make up the arrays, namely the a-Si:H photodiode and TFT. Device characterization helps determine the degree to which the arrays are viable for x-ray imaging applications and also enables optimization of array design and operation.

In this research work, measurements of the noise and radiation-damage properties of a-Si:H photodiodes and TFTs are not presented. But full investigations on photoconductive transient photoresponse (rise and decay) and its optimization have been conducted inclusively at per single pixel sensor with overall outcome basis. Trapped carriers distribution is a vital phenomenon to make available utmost temporal response and therefore investigation on trapped carriers and their distributions in the mobility gap are also taken into consideration in this work. The design calculations were performed at varying parameters basis for transient photoresponses similar to those anticipated for particular pixel in operation as shown in Figure 4.2. Amorphous silicon photodiode array consists of multiple photodiode elements, formed in a matrix arrangement in one package. But this research is limited to analysis of transient response in a-Si:H detector photodiode at x-ray image detection regime and pixel array for image formation indeed.

4.3 Numerical model for a-Si:H Photodiode in integrated pixel arena

Numerical modeling of amorphous silicon photodiode is the back bone in designing of large area flat panel x-ray medical imaging module. The following numerical model for amorphous photodiode is based on conventional continuity equations with hydrogenated amorphous silicon perspective and derived from several quantum equations. These analytical equations later on being used in code writings for novel customized simulator so that soft-hand manipulation can be conducted to make available optimized parameters for fabrication. In the photodiode model, we have considered a-Si:H based p-i-n type structure that are sandwiched between two parallel

plate electrodes and biased with a negative voltage V across the conductor terminals to establish an electric field in the i-layer.

The doped p- and n-layer thicknesses are usually very small compared to the a-Si:H i-layer thickness. The nominal thickness of i-layer is 0.5 –1.5 μm whereas the thickness of p and n-layer is approximately 20~30 nm. The photodiode operates under reverse bias condition. The reverse bias voltage drops almost entirely across the intrinsic layer. The depletion layer widths of the thin sheets of negative and positive charges in the p and n sides are negligible compared to the intrinsic (i) layer thickness, d. The photodiode is illuminated from the p-layer side and the incident photons are absorbed exponentially across the photodiode. In general, a-Si:H has relatively high density of localized states or traps in the mobility gap as compared to doped p-layer. The photogenerated carriers in the p-layer recombine or trap immediately because of practically zero electric field in p-layer and high density of localized states or traps in the mobility gap of a-Si:H. The photogenerated electrons and holes that are generated in the i-layer drifts through the entire i-layer and constitute a photocurrent in the external circuit. The integration of this photocurrent is the collected charge or the image signal.

For simplicity, we consider that there have been a continuous distributions of localized states as a series of discrete levels in the mobility gap of a-Si:H. These discrete levels are placed 50 meV apart, and thus there are 34 levels in the bandgap of about 1.72 eV. Seventeen levels in the upper-half of the mobility gap are assumed to be acceptor-like (negative when filled by electrons and neutral when empty) while the remainder are donor-like (positively charged when empty and neutral when filled by electrons). The bandtail densities fall off exponentially from the band edges with the characteristic

energies of 30 meV and 50 meV for conduction and valence band tails, respectively. The mid-band density of states is assumed to be constant for intrinsic a-Si:H.

4.4 Model calculations for photodiode transient photoresponse in a-Si:H pixel sensor

The schematic diagram representing the equivalent circuit of a photoconductive detector is shown in Figure 4.3. A photoconductor layer is sandwiched between two large area parallel plate electrodes. A current integrating amplifier is connected to the bottom electrode and measures the collected charge by integrating the induced x-ray photocurrent (the integration time is longer than that of the exposure time).

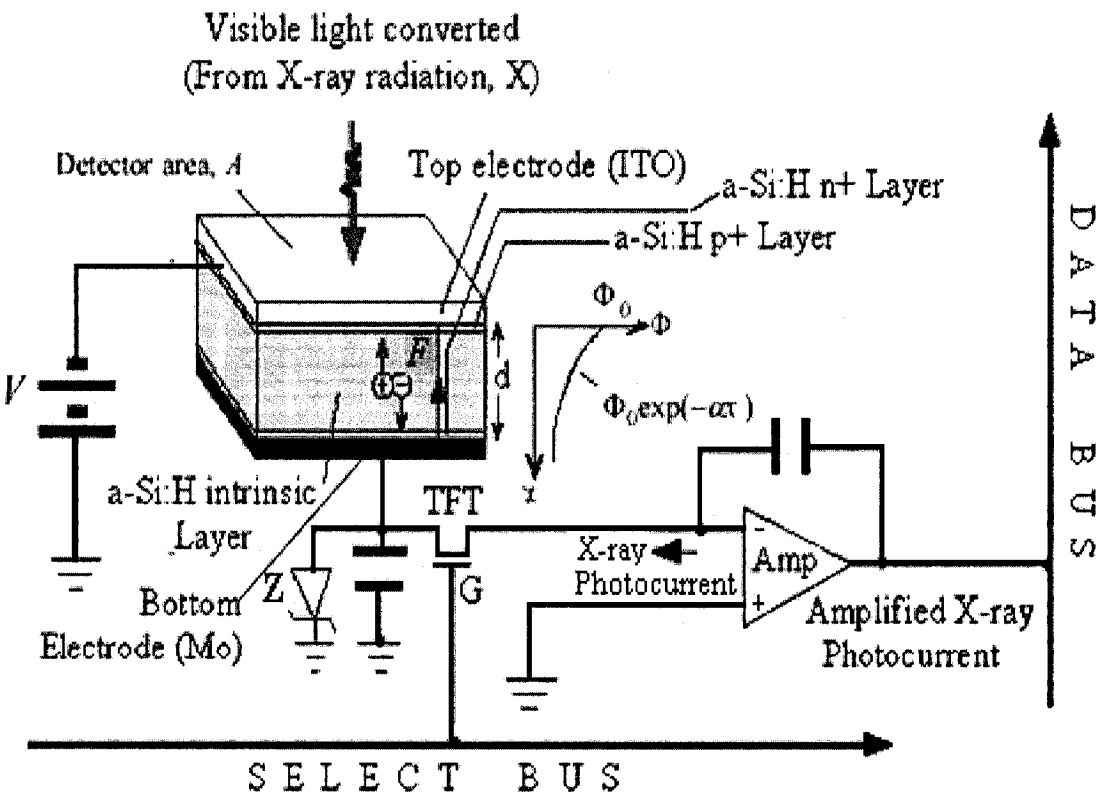

Figure 4.3: Equivalent schematic of a-Si:H photodiode in image detector.

The lateral dimension of the photoconductor thickness is d. The radiation-receiving electrode (top electrode) is biased with a voltage V to establish an electric field F in the photoconductor. The biasing voltage can be positive or negative. It is assumed in Figure 4.3 that the x-ray converted light illuminating electrode is negatively biased. The generated electrons and holes are drifted in directed by the applied field and give rise to a transient x-ray photocurrent. The integration of this photocurrent is constituted the collective carriers. The charges can be stored by integrating over time of period in storage capacitor. In order to safe operation of TFT and to avoid over voltage, a Zener (Z) diode is attached parallel with storage capacitor in each pixel so that any high potential occurrence can be grounded indeed. An amplifier has been connected with the photodiode to understand the total pixel operation, but is not included in our model calculations.

In p-i-n configured a-Si:H photodiode, thermally generated carriers constitute a continuous flow of dark current under reverse bias and the dark current is usually negligible compared to the x-ray photocurrent. For simplicity, the thermally generated carriers are not considered to study the transient photocurrent response. Similarly the diffusion of carriers is negligible compared with their drift because of high applied fields across the photoconductor. In the following, the continuity equation for both holes and electrons, trapping rate equations, and the Poison equation (or Gauss's equation in point form) are being numerically solved in the i-layer during illumination to determine the shape of photocurrent rise and trapped charges in the photodiode [65]. The light induced generated carrier's continuity behavior and transport mechanism inside the mobility gap is illustrated in Figure 4.4.

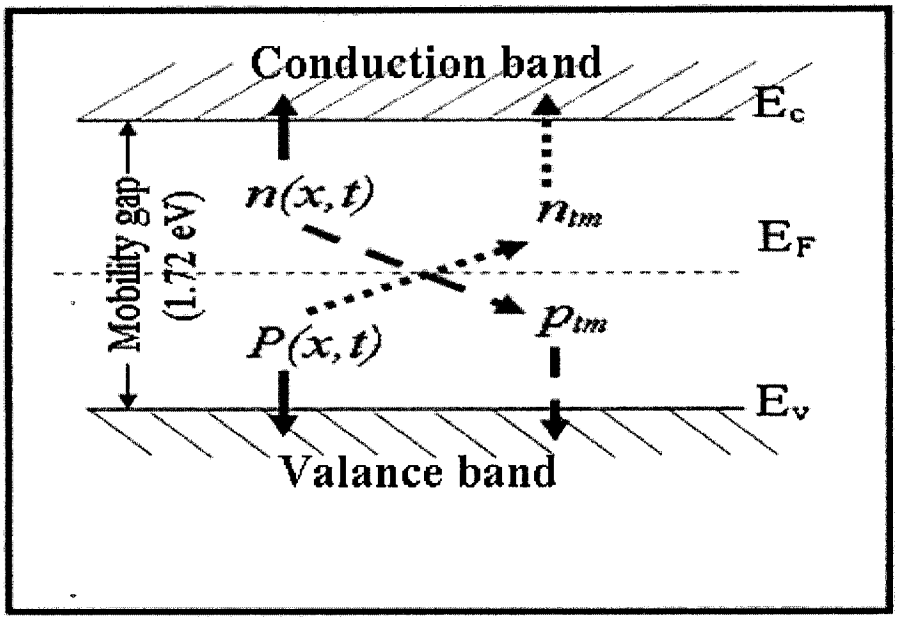

Figure 4.4: Light induced generated carrier's transport mechanism in a-Si:H.

Defining $p(x, t) \approx p$ as the free hole concentration and $n(x, t) \approx n$ as the free electron concentration at point x' at time t, the continuity equations at negative bias for electrons and holes are:

$$\frac{\partial n}{\partial t} = \mu_e \frac{\partial (nF)}{\partial x} - \sum_{m=18}^{34} C_{em} n(N_m - n_{tm}) - \sum_{m=1}^{17} C_{em} n p_{tm} + \sum_{m=18}^{34} \frac{n_{tm}}{\tau_{rem}} + G \qquad (4.1)$$

$$\frac{\partial p}{\partial t} = \mu_h \frac{\partial (pF)}{\partial x} - \sum_{m=1}^{17} C_{hm} p(N_m - p_{tm}) - \sum_{m=18}^{34} C_{hm} p n_{tm} + \sum_{m=1}^{17} \frac{p_{tm}}{\tau_{rhm}} + G \qquad (4.2)$$

The subscript e and h represent electrons and holes respectively. The first 17 trap levels in the lower half of the gap (i.e., m =1 to 17) are donor-like while the remainders (i.e., m =18 to 34) are acceptor-like. The trapping rate equations for electrons and holes at a trap level m are given by:

$$\frac{\partial n_{tm}}{\partial t} = C_{em} n(N_m - n_{tm}) + C_{hm} p n_{tm} - \frac{n_{tm}}{\tau_{rem}} \quad ; m = 18,....34 \tag{4.3}$$

$$\frac{\partial p_{tm}}{\partial t} = C_{hm} p(N_m - p_{tm}) + C_{em} n p_{tm} - \frac{p_{tm}}{\tau_{rhm}} \quad ; m = 1,....17 \tag{4.4}$$

Where,

x' = The distance between p-i interface to a particular EHP generation position. The generation nature is random, therefore the position is not shown in figure 4.4.

$x = x'/d$, where x varies from 0 to 1 as a fraction of diode intrinsic thickness d.

$F(x, t)$ = Applied electric field.

μ_e = Mobility for electrons.

μ_h = Mobility for holes.

C_{em} = Capture coefficients for free electrons.

C_{hm} = Capture coefficients for free holes.

$G(x)$ = Electron hole pair (EHP) generation rate.

α = Linear attenuation coefficient of the photoconductor.

τ_{rem} = Characteristic release times for the mth electron traps.

τ_{rhm} = Characteristic release times for the mth hole traps.

N_m = Initial unoccupied trap density at the trap level m.

$n_{tm}(x,t)$ = Trapped electron densities at mth trap level.

$p_{tm}(x,t)$ = Trapped holes densities at mth trap level.

The trapped electron and hole densities at space x and time t are given by,

$$n_t(x,t) = \sum_{m=18}^{34} n_{tm}(x,t) \quad and \quad p_t(x,t) = \sum_{m=1}^{17} p_{tm}(x,t) \tag{4.5}$$

The Poisson equation is given by

$$\frac{\partial F}{\partial x} = \frac{e}{\varepsilon}\left(N_i + p + p_t - n - n_t\right) \tag{4.6}$$

Where, N_i is the initial space charge in the sample. The initial unoccupied trap density at the trap level m is given by,

$$N_{tem} = g(E_m) f_0(E_m)\Delta E; \qquad m = 1 \ldots. 17, \tag{4.7a}$$

$$N_{tpm} = g(E_m)[1 - f_0(E_m)]\Delta E; \qquad m = 18 \ldots.34, \tag{4.7b}$$

Where g(E_m) is the density of states at energy E_m, f_0 is the Fermi function before illumination, and ΔE is the interval of the discrete trap levels ΔE = 50 meV in our calculations and can be taken less than 50 meV for precise results once adequate processor speed are available in computer.

When no electric field is present, the release rate for trapped electrons and holes are,

$$\frac{1}{\tau_{rem}} = \nu_{em} \exp[(E_m - E_c)/kT], \qquad \text{Where } \nu_{em} = C_{em} N_c \tag{4.8a}$$

$$\frac{1}{\tau_{rhm}} = \nu_{hm} \exp[(E_v - E_m)/kT], \qquad \text{Where } \nu_{em} = C_{hm} N_h \tag{4.8b}$$

Where, ν is the attempt-to-escape frequency, k is the Boltzmann constant, T is the absolute temperature, and E_c and E_v are the conduction and valence band edges. The attempt-to-escape frequency ν_{em} and capture coefficient C_{em} are related by a detailed balance relation $\nu_{em} = C_{em}N_c$, where N_c is the effective conduction-band density of states. Similarly $\nu_{hm} = C_{hm}N_v$, where N_v is the effective valance band density of states. When an electric field is applied, the potential barrier is lowered by the Poole-Frenkel effect and/or carrier tunneling through the barrier, and hence enhances the carrier release rate.

The release of an electron or hole from a neutral defect, D^0, leaves a charged state,

$$D^0 \rightarrow D^+ + e; \quad D^0 \rightarrow D^- + h \tag{4.9}$$

The Coulomb interaction gives a Poole-Frenkel effect with a barrier lowering $\Delta E_{PF} = \beta_{PF}\sqrt{F}$, where $\beta_{PF} = \sqrt{e/\pi\varepsilon}$. On the other hand, the carrier emission from charged defect states,

$$D^+ \rightarrow D^0 + h; \quad D^- \rightarrow D^0 + e, \tag{4.10}$$

However, it does not experience a Coulomb interaction, rather enhance the carrier release rate by tunneling through the barrier with a barrier lowering of $\Delta E_L = FR_T$, where R_T is the tunneling length. It is important to mention here that the Poole-Frenkel effect is effective only for the Columbic interaction. On the contrary, tunneling through the barrier can occur independently during carrier release from both charged and neutral defects mentioned above. Moreover, under thermal equilibrium condition, the trap levels are identified with the D^0 center observed by electron-spin resonance [66]. Therefore, the trapped electron and hole states are most likely D^- and D^+ states. Thus the field-enhanced carrier emission is possibly dominated by the tunneling mechanism. The electron-hole pair (EHP) generation rate is given by,

$$G(x) = \Phi_0 \alpha e^{-\alpha x'} = \Phi_0 \alpha e^{-\alpha x d} \tag{4.11}$$

$$G(x) = \Phi_0 \alpha e^{-\frac{x}{\nabla}}; \Delta = \frac{1}{\alpha d} \tag{4.12}$$

Where Φ_0 is the incident photon flux per unit area and α is the linear attenuation coefficient of the photoconductor. For particular carrier, we consider the position is x′

and in generalized form, the carriers traverse the distance, x'=xd, where x varied from 0 to 1. The necessary initial conditions before illumination are,

$$p(x,0)=0, \quad n(x,0)=0, \quad p_{tm}(x,0)=0, \quad and \; n_{tm}(x,0)=0. \tag{4.13}$$

The boundary condition for electric field is given by,

$$\int_0^d F(x,t)dx = V \tag{4.14}$$

After EHP generation due to illumination, electrons move towards the bottom electrode and holes move towards the top electrode under negative bias. Therefore, just after (or shortly after) x-ray exposure, the free electron concentration at $x = 0$ and the free hole concentration at $x = 1$ are zero since the carriers would have started drift.

The photocurrent rise density is given by

$$j(t)=\frac{e}{d}\int_0^d F(x,t)[\mu_e n(x,t)+\mu_h p(x,t)]dx \tag{4.15}$$

This will be ultimate signal for image detection extracted from individual pixel.

4.5 Traps Carriers Release (decay) Current

Immediately after the end of illumination, a transient current associated with thermal emission of the non-steady-state trapped carriers flows in the external circuit. Assuming that the carrier lifetime is longer than the transit time so that the re-trapping and recombination processes may be ignored, the current due to electrons liberated from the traps within dx at the distance x from the radiation-receiving electrode is given by [67].

$$dJ_n(t) = e\sum_{m=18}^{34}\frac{n_{tm}(x,t)}{\tau_{rem}}\left(1-\frac{x}{d}\right)dx = e\sum\frac{n_{tm0}(x)}{\tau_{rem}}\exp(-t/\tau_{rem})\left(1-\frac{x}{d}\right)dx \quad (4.16)$$

Where, n_{tm0} is the trap density at trap level m at the end of illumination. Integration of equation (4.16) over the space-charge layer yields;

$$J_n(t) = e\int_0^d \sum_{m=18}^{34}\frac{n_{tm0}(x)}{\tau_{rem}}\exp(-t/\tau_{rem})\left(1-\frac{x}{d}\right)dx \quad (4.17)$$

Similarly, the expression for the holes constituted current is given by

$$J_p(t) = \frac{e}{d}\int_0^d \sum_{m=18}^{34}\frac{p_{tm0}(x)}{\tau_{rhm}}\exp(-t/\tau_{rhm})xdx \quad (4.18)$$

Then the total current after illumination to be observed is, $J(t) = J_n(t) + J_p(t)$

Or,

$$J(t) = e\int_0^d \sum_{m=18}^{34}\frac{n_{tm0}(x)}{\tau_{rem}}\exp(-t/\tau_{rem})\left(1-\frac{x}{d}\right)dx + \frac{e}{d}\int_0^d \sum_{m=18}^{34}\frac{p_{tm0}(x)}{\tau_{rhm}}\exp(-t/\tau_{rhm})xdx \quad (4.19)$$

This will be the residual (decay) current drawn from individual pixel.

4.6 Numerical basis for simulator code writings

The numerical calculations as formulated in section 4.5 is based on a photodiode and the diode's active layer is sandwiched between two large area parallel plate electrodes. The x-ray radiation is incident over a phosphors layer (not shown in figure 4.3) and the phosphors layer are being converted x-ray photons to visible light which further incident on the p-i-n photodiode with an area A and the electric field F is established by applied bias voltage V. The established field, $F=V/d$, where d is the active layer thickness. The capacitor can be stored drifted charges for an interest of time. The x-

ray photocurrent is then amplified to obtain a permissible analog response to be well fitted in digital world for further reshaping and digitization.

The customized simulator code was written in matlab program followed by finite difference method (FDM) and it only taken care of one single pixel by FDM strategy one can solve 2-D differential gradient either by eliminating the differential equation completely (steady state problems), or by rendering the partial differential equations (PDE) into an equivalent ordinary differential equation, which is then solved using standard techniques such as finite differences techniques. The simulator basis finite difference numerical calculations and strategy are illustrated in APPENDIX-E and APPENDIX-F.

4.7 Design parameters optimizations strategy

We made available customized simulator followed by background equations as modeled in section 4.5 and the simulator code were written based on the same model equations as well. Therefore, the simulator itself a soft-hand model device and is operable in soft-hand environment with desired parameters to realize efficient device before fabrication. Although the simulator has full access capability to manipulate all possible parameters, we were not gone through for all of them in this thesis. Rather we concerned and tested on crucial parameter that affect the device performance directly. For instance active layer thickness (d), applied field (F), dose or generation rate, and x-ray exposure time that is directly involved into p-i-n photodiode performance.

In principle, p-i-n structured a-Si:H photodiode has a depleted intrinsic region with high electric field implication that serves to separate photo-generated electron-hole

pairs. Increasing the level of illumination increases the number of charge carriers generated and thus increases the level of current. So the photodiode has two types of nature: optical and electrical. The modeling of photodiode requires mixed nature modeling concept

4.8 Simulator functionality tests on model a-Si:H pixel sensor and design manipulations at short range x-ray exposure

To model simulation and soft-hand experiments, we already presented a model to interpret the steady-state and the dynamic detection limits of a-Si:H x-ray imaging pixel sensor in 2-D regime (Sections 4.5 and 4.6). An equivalent electric circuit was derived and the predicted values are determined by soft-hand experimental in the following tests for 2-D active matrix regime with different operable parameters. Here simulation time was kept intentionally low in order to maintain low-time costs and just for tests that conducted on one single parameter while others parameters were remained typically constant to verify simulator workability. However, full-pledged experiments to be optimized as mentioned above on all critical parameters are reported in chapter 5.

4.8.1 Simulator test at varying Photodiode active layer thickness

The minimization of dosage requires the permissible absorption depth such that the most of the radiation is absorbed within the active layer thickness, d. This means the captivity of EHP is depends on adequate d, but the collection solely depends on the field. However, when d is increased, there is an increased probability that the freed carriers will be trapped as they drift across greater distances to reach the respective electrodes, i.e., the

sensitivity may become Schubweg-limited. Note, the mean free path length is also called Schubweg; for each type of charge carriers can be expressed as the product of the mobility μ, the electric field strength F and the life-time τ, as $\delta = \mu\tau F$. The combined mean free paths of electrons and holes, $\delta = (\mu_e\tau_e + \mu_h\tau_h)*F$, is the mean distance a hole and an electron can separate. This distance is referred to as the collection distance [68].

The collection distance and the efficiency ∇Q are related according to Ramo's theorem. On the other hand, the transit time of electron and holes are inversely proportional to the field and directly proportional to the diode thickness. So, when field decreases or diode thickness increases, the transit time increases as well by the relation $t_e = d/\mu F$. When transit time increase, the trapping probability of the electrons or holes will be increased accordingly. The thickness were varied from 0.5 μm with keeping all other parameters fixed (such as, applied fields 2 Volt-μm^{-1}, charge generation rate $10^{14}cm^2s^{-1}$ and exposure time 16 μs) and eventually any increment of d beyond Schubweg limits results the photoresponse disappeared.

After keen observation, it was found that the photocurrent was disappeared at about d=1580 nm. The photocurrent got back again when we decrease the intrinsic thickness only by 0.7 nm from 1580 nm at a minimal (threshold) ratio of 'Schubweg/d' around 44.32 as shown in Figure 4.5, experimental data are tabulated in appendix A. The threshold ratio is a boundary measure when photocurrent about to disappear depending on optimal d and F. At a threshold limits, further increase of d or decrease of F results no photocurrent in amorphous photosensor. Therefore, an a-Si:H photodiode with 1 μm thickness, the required Schubweg ($\mu\tau F$) value should be at least 44.32 times than that of the active layer thickness (d) in order to maintain device functionality in active.

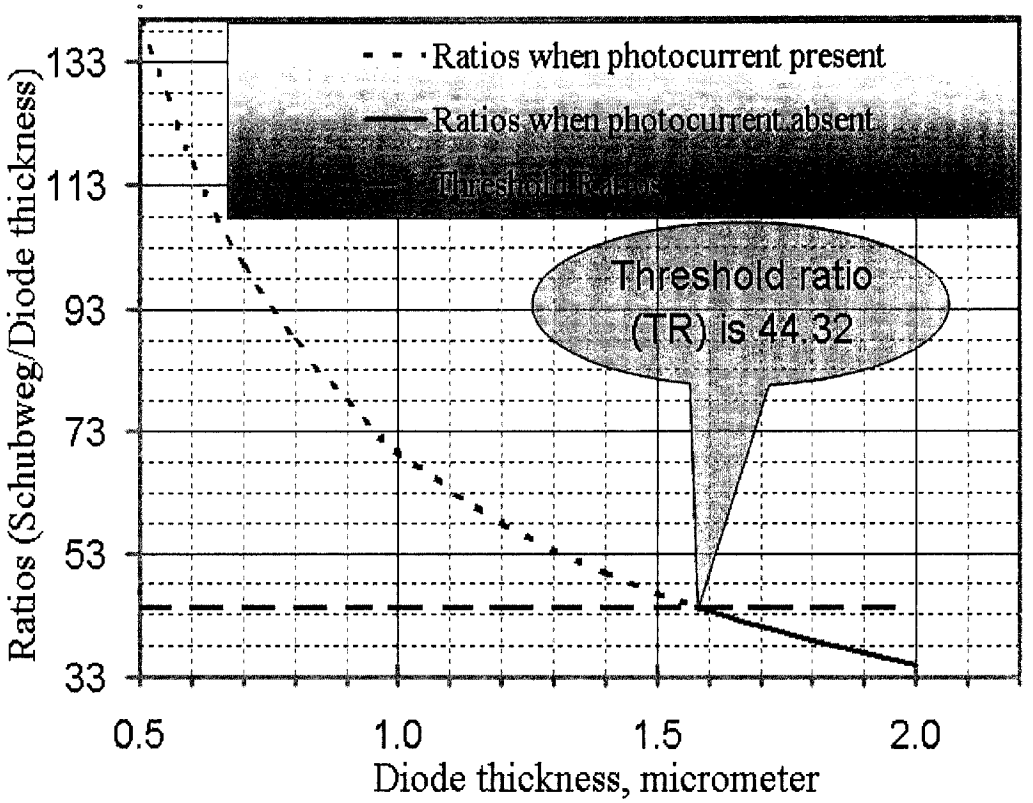

Figure 4.5: 'Schubweg/d' ratio *versus* Photodiode thickness (d) at constant applied field ($2x10^6$ Volt/Meter).

With the same set-up, further we explored the response availability by nominal fields varying techniques. As the photocurrents were absent at 1580 nm, we then investigated whether insufficient field is responsible for missing response or not. We started to increase a traceable amount of fields and found the photocurrent back again i.e. while increased the field only by 0.839 mVolt-μm^{-1} in addition to previous field 2 V/μm, the photoresponse traced. Also, observed that the reduction of applied field by about 0.3×10^{-6} Volt-μm^{-1}, the photocurrent once again disappeared from the same set-up and the experimental data are tabulated in appendix B.

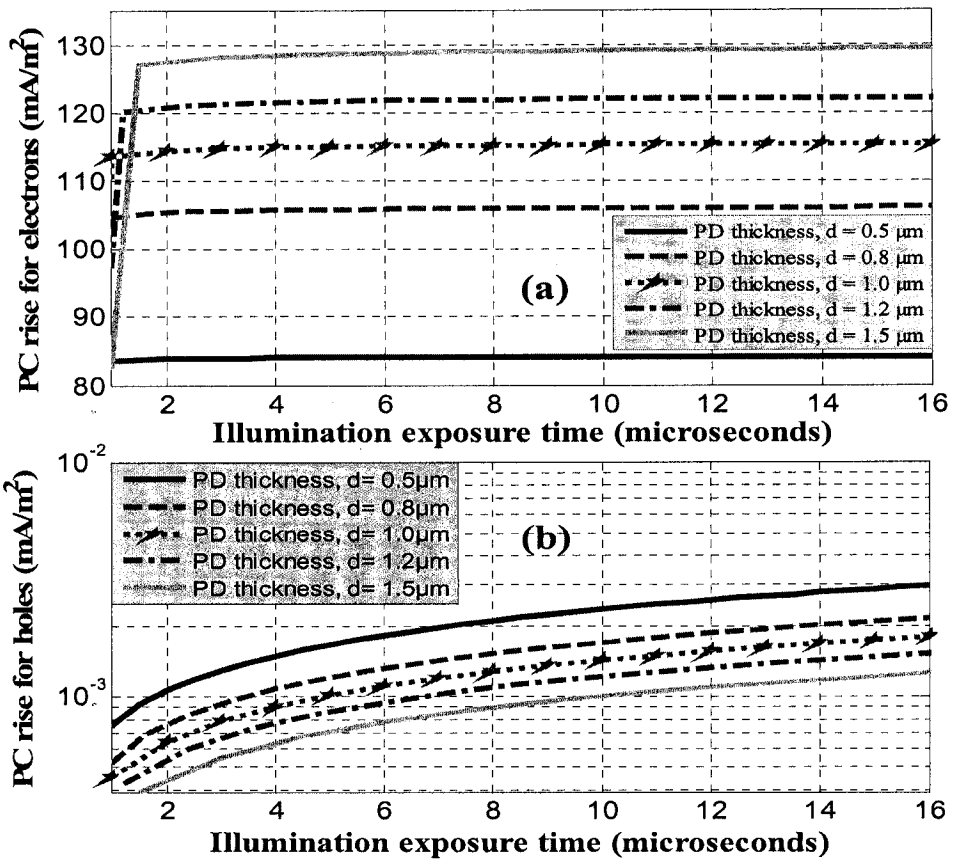

Figure 4.6: The photocurrents (PC) in a-Si:H photosensor with different photodiode thickness (d). The major fixed parameters are (i) applied field is 2 V/μm, (ii) Illumination exposure time (short) is 16 μs and (iii) EHP generation rate, Q_0 is 10^{14} $cm^{-2}s^{-1}$. (a) Electrons current (b) holes current.

The electrons and holes that were generated by irradiation in a-Si:H photoconductors were not collected by the electrodes in equal magnitudes within time of interest as shown on Figure 4.6. Mobility of electrons is higher than that of holes, therefore, for a fixed period of exposure time, the electrons will reach faster to the electrode, which constitutes a dominant contribution to the overall photoresponse rise. As hole drifts slowly, consequently the un-collected holes always would be in the active layer.

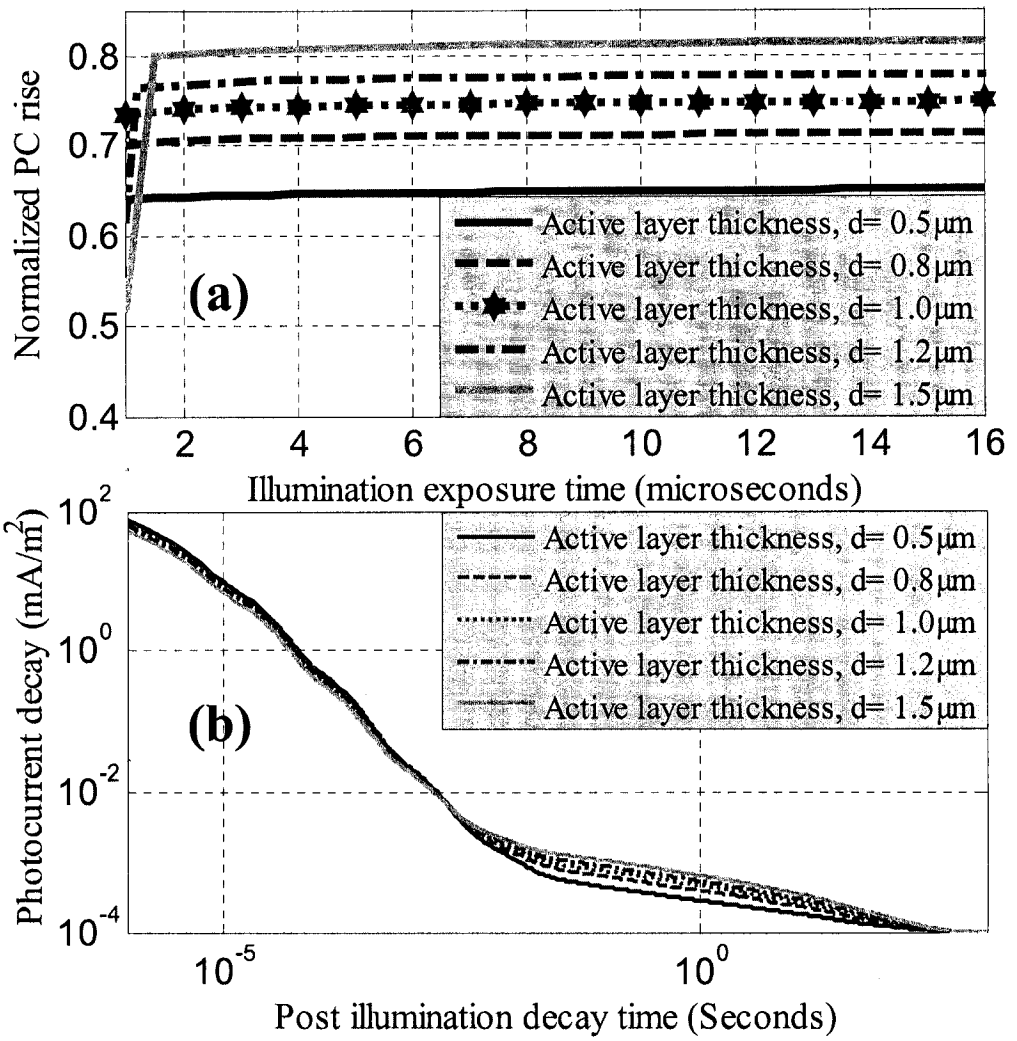

Figure 4.7: The photocurrent (PC) at varying diode thickness for applied field 2×10^6 V/meter (a) Normalized PC rise, and (b) Post illumination PC decay.

When the supply of the carriers stops by scanning clock or by non-activated addressed TFT, the under way carriers are no longer contributes to the temporal image response. Rather trapped in deep trapping levels or sited temporarily in the localized states, which release later in post illumination time span from localized states, caused the decay current enhancement. In diagnostic x-ray imaging, those un-collected carriers are caused a severe problem, for instance temporal artifact or ghosting, which may causes a

shadow of the previous image. In overall, it makes the current image realization more complex and limits the system usability, become unsuitable for fluoroscopic applications.

On the other hand, the residual current is dominated by holes in regular sensor operation because of low inherent mobility and those phenomena have already been explained. Moreover, scenario became more complex when the operation is conducted with insufficient field or a thick (very large) photodiode. In that case, transit time (t_e=d/(μF)) become very large and become comparable to mean free path of the carrier lifetime.

The simulated photocurrents showed in Figure 4.7(a) in normalized measure. In normalized measure, the magnitude is re-assessed to a desired scale, usually in percentage to make available comparative measure with highest possible magnitude. The experiment results showed that the photocurrents increase when active layer thickness (d) increases. But beyond d = 1.573 μm, we experienced the photocurrent are disappeared. It signify that the generated EHP is no longer available for photocurrent and that can be happened either by carriers deep trapping in to deep traps center or recombination of the electron-hole themselves. The trapped carriers that are deeply trapped and are released later on post illumination time of span, constitute a residual (decay) photocurrent (see Figure 4.7(b)). Although the decay current do not vary significantly with active layer thickness initially, but the measure still dictates that the residual current increases with active layer thickness and decay trend is potentially recombine/deep trapped mode. However the measurement with higher illumination time are strategically important for further investigations and therefore are discussed inclusively in chapter 5

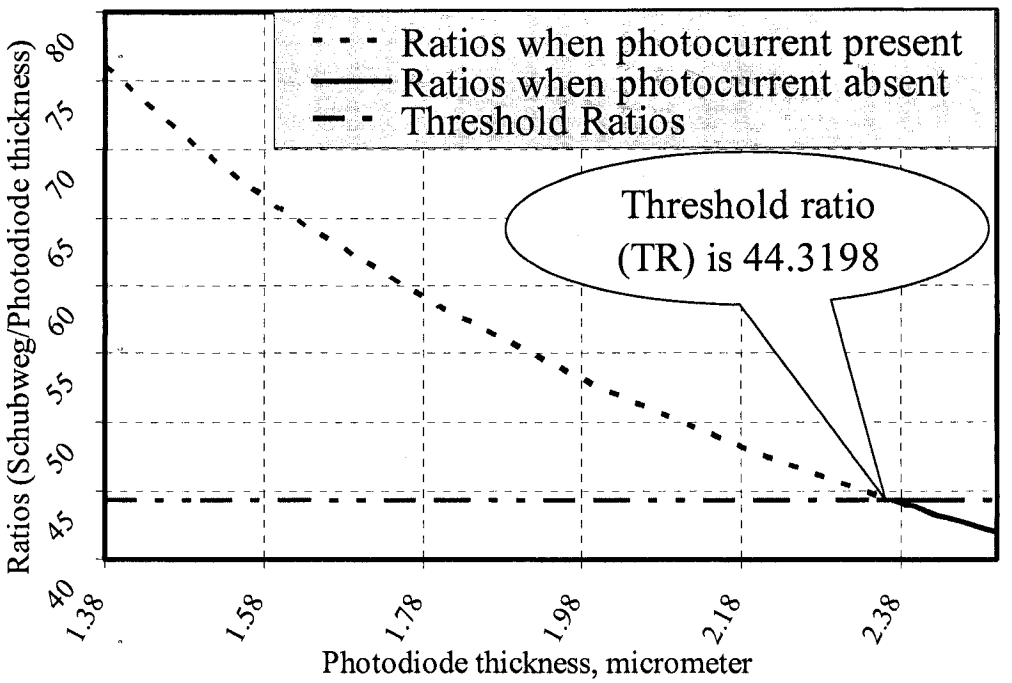

Figure 4.8: 'Schubweg/d' *versus* Photodiode thickness (d) at constant applied fields ($3x10^6$ Volt/Meter). Under the threshold ratios, photodiode would not work as a photo sensor. All experimental data are tabulated in appendix C.

We extended our investigation further on higher diode thickness with constant field at short x-ray exposure fluence and vice-versa. Recall results from appendix A, initially we considered our p-i-n photodiode intrinsic thickness is 1 μm, with an applied electric field of $2x10^6$ Volt-meter^{-1} and experienced no photoresponse beyond d = 1.573 μm. Now we are increasing the active layer thickness to 2 μm and obviously $2x10^6$ is not sufficient. Therefore, the electric field further increased to $3x10^6$ Volt-meter^{-1}. We started to increase the bulk thickness and the photocurrent disappeared once again at 2.3691 μm (Appendix C). The photoresponse further appeared once the thickness reduced by 0.1 nm to d = 2.3690 μm and or by increment of field a little bit (appendix D), which are shown in Figure 4.8.

In these experiments the threshold 'Schubweg/d' ratios remains almost the same as previous experiments (figure 4.5). Instead 44.32, we got the transition Schubweg/d ratio 44.3198 as shown in Figure 4.8. After careful examination, we concluded that this is a defined guideline that inclusively provides what should be thickness-field combination in order to maintain threshold limits for a-Si:H photosensor implications. At least our experiments forecasted the ratio of 'Schubweg/d' should be around 45 for pixel in operation.

4.9 Summary

Image quality is intimately linked to the precise and accurate acquisition of information from the x-ray beam transmitted by the patient and the quality of image mostly depends on the x-ray imaging pixel sensors. These sensors uniquely are all about photoconductors or photodiodes dominated in imaging technology. In this chapter, numerically solved custom a-Si:H photodiode model and model based customized simulator has been developed and deployed successfully. By exploiting those soft-hand advantages, crucial photodiode modeling has been accomplished and tested simulator functionality indeed. To examined model considerations pertinent to thin film a-Si:H pixel sensor for transient outcome by the photodiode have been configured and reviewed. The simulation results extracted by the customized simulator have shown a good agreement with the conventional results. Later extensive experiments have been conducted for detailing model consideration in chapter 5.

More importantly, in the model both electrons and holes contributions have been considered to measure transient photoresponse. Therefore, it is more accurate and

authentic for transient model characterization. The available researches are based on either electrons or holes contributions and the presented duel contributed model approach is the first time ever citation so far. It is to be mentioned here that the presented customized simulator not only workable for a-Si:H pixel sensor, rather it is a generalized tools that can be implied in any other material's made photosensors. Because it is designed based on the continuity equation and the variables are only the typical data inputs.

Chapter 5: Pixel Photodiode (PPD) Fabrication Techniques, Parameters Optimization, and Results Analysis

5.0 Overview

a-Si:H pixel photodiodes (PPD) coupled to suitable scintillators is shown to be suitable for detecting charged particles, carriers, and x-rays. In an active-matrix addressing scheme, each pixel has a switch and a detector device for the pixel function. Amorphous silicon TFTs are the most common switching elements in these applications. Figure 5.1 shows a prototype image sensor pixel, which consists of an a-Si:H TFT, a storage capacitor and a p-i-n photodiode. This prototype architecture promises very good fill factor which discussed already in previous chapter.

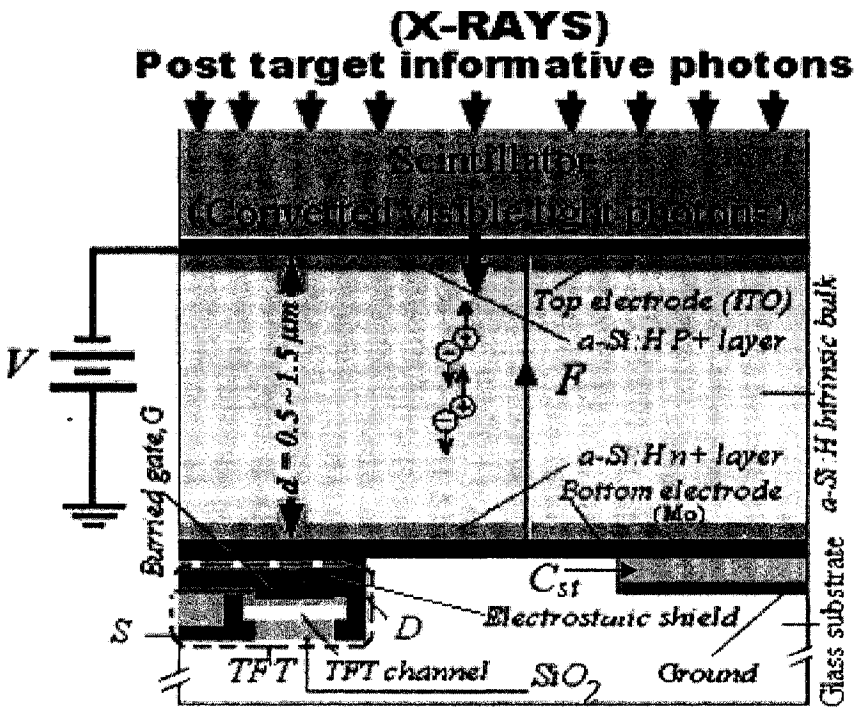

Figure 5.1: a-Si:H pixel model architecture for diagnostic medical X-ray imaging use. Pixel is comprised with TFT, Photodiode and a storage capacitor, but photodiode modeling is under focused.

In this section, soft-hand optimization techniques are employed for optimal pixel operation. Follow suit theoretical model calculations and short range exposure experience based on customized simulator as implied in section 4.8, here further implemented the same strategy inclusively with practically viable optimized parameters, so that a real time device can be materialized. However the analysis is limited to crucial design parameters, for instance applied fields (F), active layer thickness (d), EHP generation rate and the exposure (illumination) pulse duration.

5.1 X-ray image sensing pixel photodiode (a-Si:H) model optimization and results analysis

Electron-hole-pair (EHP) is directly proportional to the incoming converted visible photons, photon frequency as well as the materials that are used in intrinsic zone of the p-i-n photodiode. The x-ray fluence at first exposed on objects (viz. humane organs or any solids), then informative (obstructed) x-ray photon reached to scintillator surface and proportionate visible light photons evolve from scintillator exposed on photodiode surface. A 3-D brief depiction of 4×4 pixels are illustrated in Figure 5.2.

The EHP generation rate in photodiode, generally referred as dose (Q_0 $cm^{-2}s^{-1}$), is dependent on several parameters. As mentioned before, primarily it depends on the incoming x-ray photon frequency, x-ray photon energy, conversion capability of scintillator, absorption capability of light photon absorbing materials (viz. a-Si:H in the intrinsic zone in photodiode), and the time allowed to expose on the sensors. Once EHP generated in reverse biased p-i-n photodiode, the carriers can be swept out easily, but the optimized extraction with feasible parameters selection is a key factor for efficient

operation of a-Si:H pixel sensors in order to produce quality image productions by active matrix flat panel system.

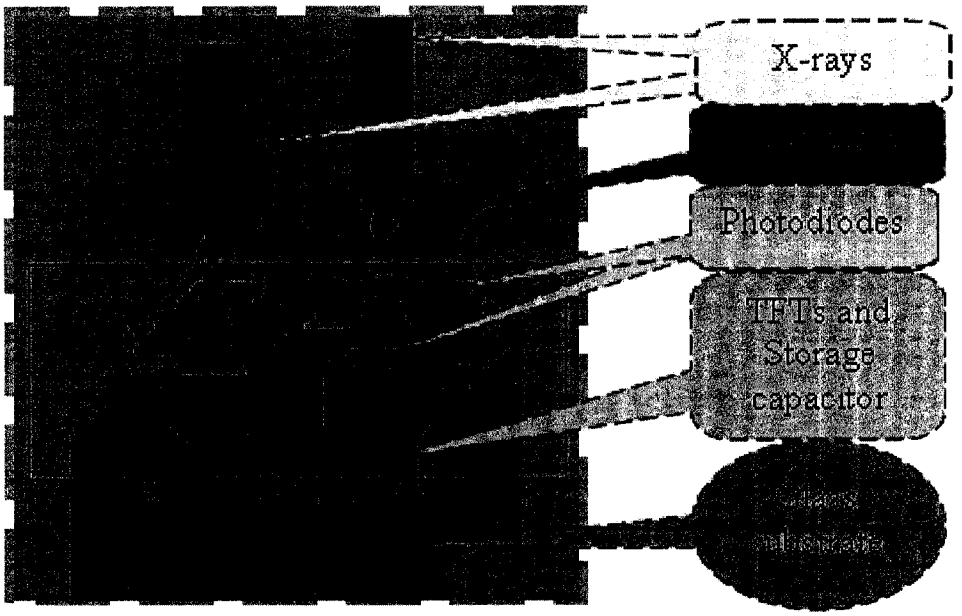

Figure 5.2: 3D X-ray image pixel sensor array by 4x4 resolutions. Actual AMFP displays unit comprised typically more than 1000×800 pixels; depends on resolution of the systems [69].

At an elevated dose operation with certain applied bias, one must keep an eye to avoid massive trapping that caused by deep trapped of the collectable carriers, which may limits the successful use of pixels. The applied field only assists to sweeping out the carriers to the external circuit but not have any direct influence to avoid trapping phenomenon unless Schubweg limitation condition is occurred. Moreover, the quantum efficiency is limited to thickness that light penetrate inside the bulk and absorption co-efficient of the intrinsic material itself. Figure 5.3 shows the quantum efficiency (QE), where active layer varied up to 1 micrometer and a relative measure with attenuation depth has been added so that an optimal efficiency can be ensured. Although the QE

predicted 96% but practically might not achieve so much as there is several adverse affect that reduces effective QE, for instance cross-talk and design precision limitations.

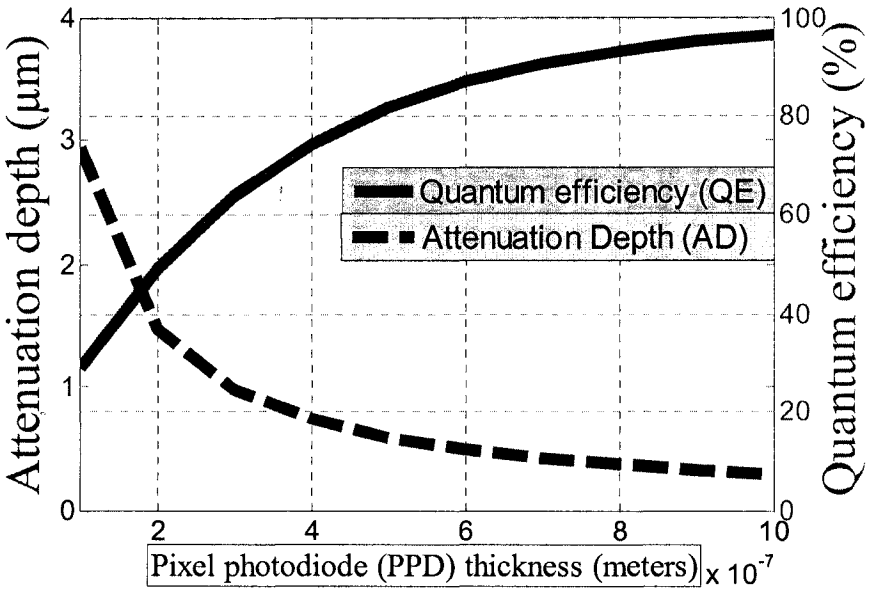

Figure 5.3: 'Quantum efficiency (%) and attenuation depth' *versus* a-Si:H Photodiode thickness (d) dependency depictions.

In figure 5.4, density of states for intrinsic a-Si:H has been depicted. For simplicity, we consider averaging states in the deep trapping zone situated in the middle of the mobility gap. This figure shows the total number of trapping available levels. Since the generation of carriers and its trapping/de-trapping activity starts simultaneously, those carriers situated in shallow states escaped from trapping states are then joined to the drifted carriers and make contribution to the resultant transient photoresponse. Some of the carriers are trapped in deep states can not escape at least within the time of interest and could not contribute to the photoresponse rise. But can be released later on in post illumination phases that constitute unnecessary decay currents results an image lag in radiology. Strategically in flat panel detectors, the carriers are being collected in

integration mode i.e. storing the generated carriers for certain time of interest in to a storage capacitor.

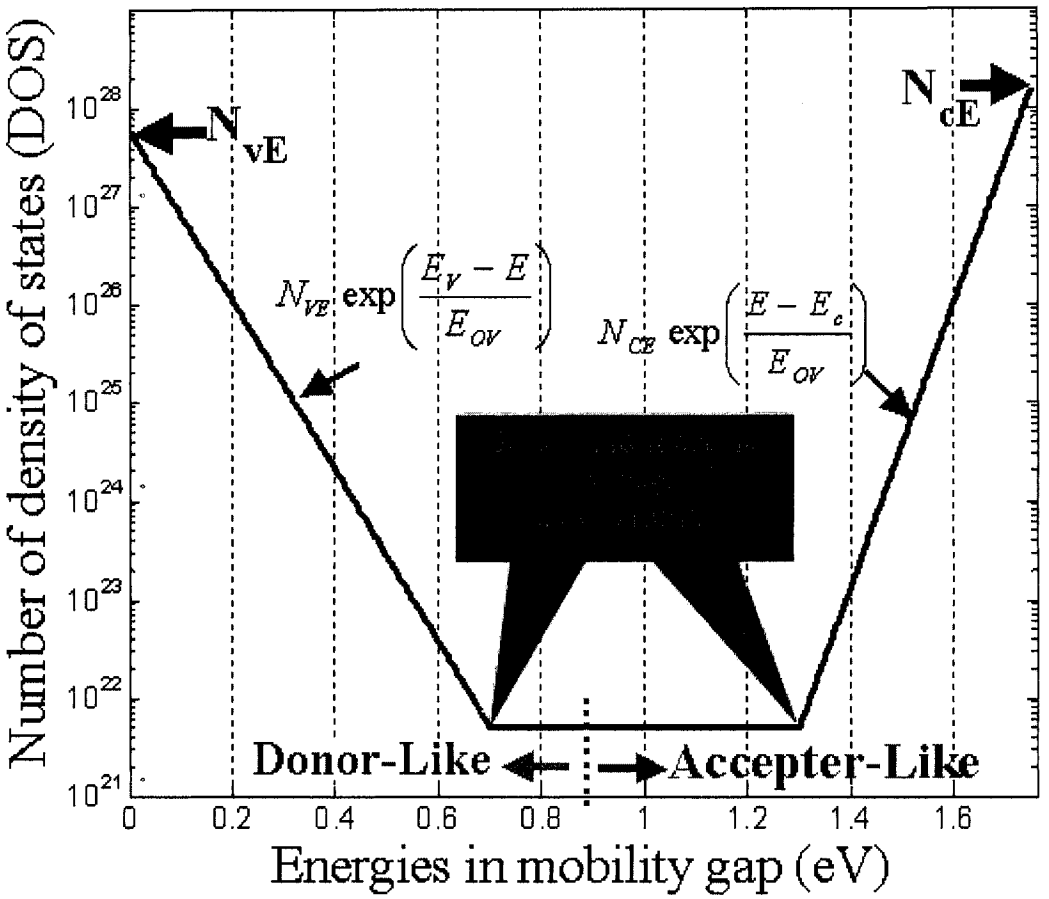

Figure 5.4: Density of states of a-Si:H. The above figure has been constructed with consideration of reported density of states (DOS) & parameters ~ $N_{CE}(E) = 1.6\times10^{28}$ m^{-3} eV^{-1} [70], $N_{VE}(E) = 6\times10^{27}$ $m^{-3}eV^{-1}$ [71], Midgap, $N = 5\times10^{21}$ $m^{-3}eV^{-1}$. Decay constants ~$E_{OC} = 0.03$ eV, and $E_{OV} = 0.05$ eV [26].

However, due to sharp exponential increase and random trapping/de-trapping behavior of the band edge carriers, we experienced difficulties to track down those carriers by conventional computer efficiently. Because, once switch the a-Si:H photodiode, its band edge carriers momentarily pass through to the conduction band stream and is understandable from Figure 5.5. As the numerical derivations were derived

based on several discrete levels, the more precise results may be surmounted by increasing the discrete levels (close to analog), but to accomplish this one should have to proceed with supercomputer for fastest possible simulation run-time.

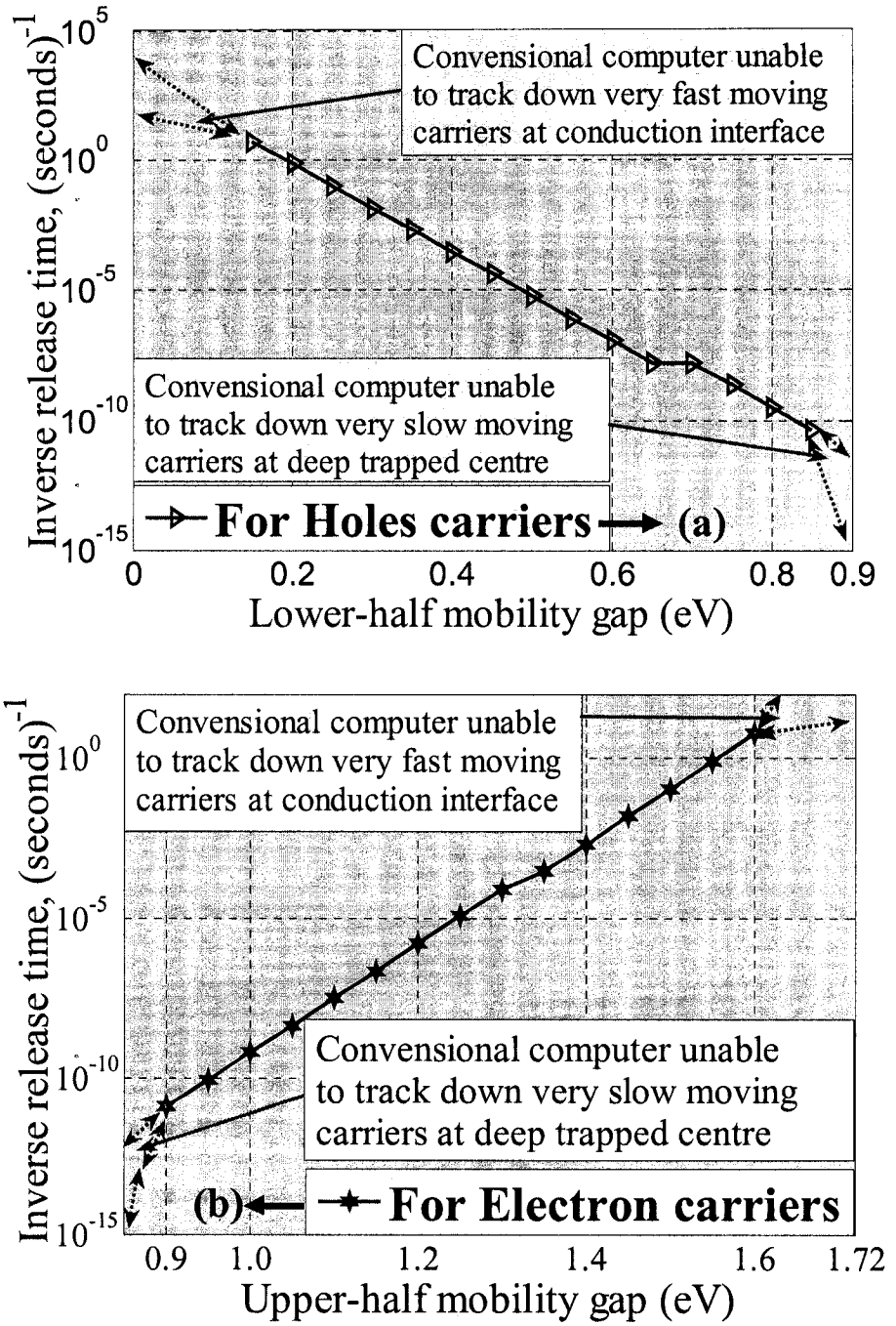

Figure 5.5: Trapped carriers release rate inversely depicted (a) Holes (b) Electrons.

After careful examination of the Figures 5.5, the sallow trapped carriers released momentarily, where as the deep-trapped carriers constituted infinite release time (about 32000 years). The slope of the curves signify that how fast trapped carriers moving out to the conduction bands from successive traps centre. Although the electron conduction band edge carriers release time depicted lower than that of holes release time; in reality we were unable to measure electron band edge carrier release time by conventional computer. We experienced run-time error once we approached to the vicinity of band edge levels. Note that these figures were simulated in mode of inverse directive in order to match up matrix elements (discrete levels) with shared programs in 2D calculations. The following analyses are based on simulative tests and comprehensive investigation to cop up optimized operative conditions of sensing photodiode in pixel arena.

5.1.1 Fields optimization for a-Si:H pixel photodiode

This section dealt with field impacts on transient photoresponse in 1 μm a-Si:H photodiode and tested the optimal bias condition that is feasible in technically and economically. The dose and exposure time were implied $Q_0 \sim 10^{14} cm^{-2} s^{-1}$ and 5 milliseconds respectfully. Practically field does not entail a serious restriction on the constituted photoresponse of the carriers since the conditions can readily be optimized by appropriate selections of pixel photodiode (PPD) thickness, applied bias and illumination time. The field responsive transient photocurrent has been evaluated by two critical measures: low field and high field conditions. This strategy made possible to optimize a field boundary condition in respect of efficient carrier collections.

In general at low field PPD (Pixel Photodiode) application, the carrier transit time τ_T is much larger than that of the carrier capture time τ_c and is comparable to the release time τ_r of trapped carriers, i.e. $\tau_c << (\tau_T = d/\mu F) \approx \tau_r$. Consequently free carriers are removed from the injected charge packet followed by a set of localized traps; finally make their way towards to the collecting electrode. When the release time become comparable to the transit time, the time derivative of the free carrier density will vanish over a long time interval i.e. the number of free carriers in the transport band will eventually reach a steady state value. Our result evident the same phenomenon as shown in Figure 5.6, where the current constituted more steady state at a lower implied fields.

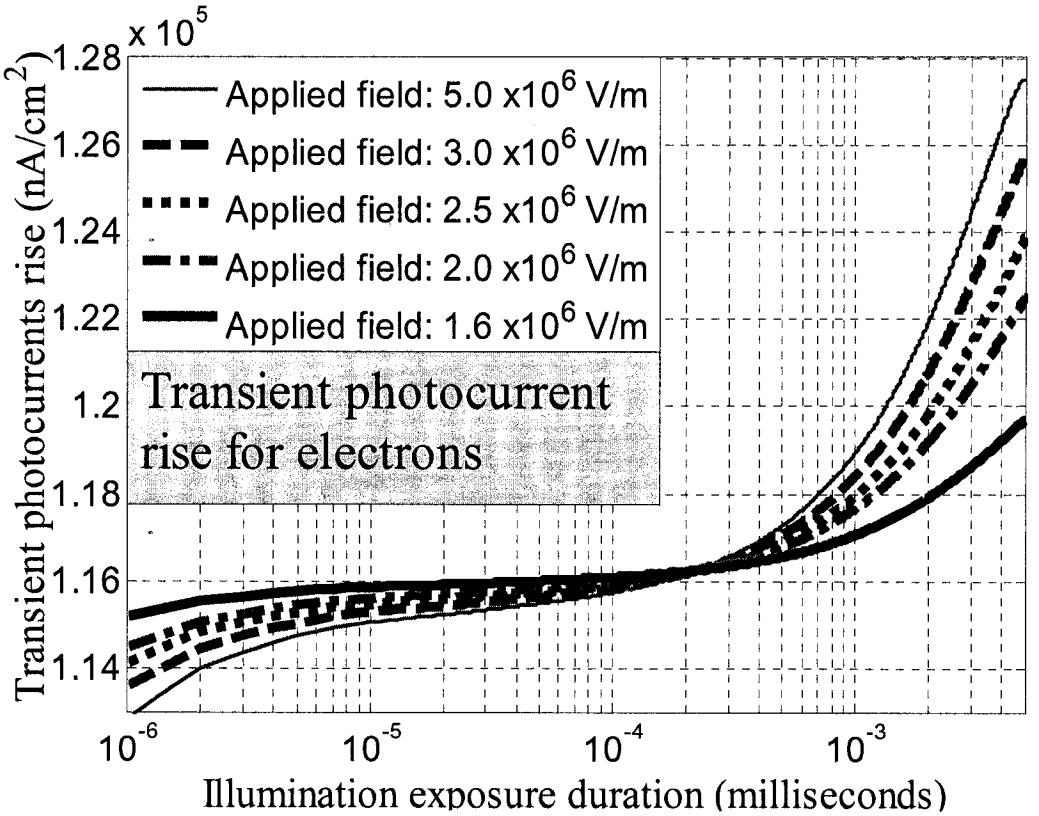

Figure 5.6: Overall transient photocurrents rise at different fields in log time scales, keeping same illumination exposure time (5 milliseconds) with generation rate 10^{14} cm^{-2} s^{-1} and diode thickness, d=1 μm.

On the other hand, when applied field '*F*' increased, the magnitude of $d/\mu F$ i.e. transit time (τ_T) decreases accordingly. If the field increased significantly, the transit time become very short and significant numbers of injected carriers traverses the entire length of the solid without becoming trapped, i.e. $\tau_T = d/\mu F << \tau_c$, Marini et al. [72]. With an applied field 5 V/μm, photocurrents are drawn sharply (near exponential mode). Within 1 milliseconds, all the responses are drawn incrementally and the final magnitudes of the responses are very close, although the inputted fields are varied from 1.6 V/μm to 5 V/μm as shown in Figure 5.6. Because field do not insist carrier generation, but insist carrier collection only.

As described already, the low field caused comparable release time to transit time and this is the pre-condition for steady state to some extend. However, the holes current increased irrespective of fields as shown in Figure 5.7. The inherent slow mobility of the holes caused continual arrivals to the electrode within the time of interests. It is to be mentioned here that in reverse biased p-i-n photodiode, the responses are mostly electrons dominated and can be realized with comparing of Figures 5.6 and Figure 5.7.

The overall photoresponses are collectively summation of electrons, holes and dark currents. From Figure 5.6, it is understandable that the current increased insignificantly with fields. But this bias voltage increment (from 2 V/μm to 5 V/μm) is not an easy task, especially when deals with active matrix flat panel imaging systems. Because the architectures of these sensors are matrix basis fabricated with millions of pixels and dimensions are several hundreds of square centimeters. The requirement cost of applied bias is huge. Therefore, it is not an economical option to increase costly applied bias once permissible response is there available. It is our understanding that 2

V/μm applied field is fair enough for 1μm PPD thickness as there is ensured ~90% photocurrent already and further exploiting modern software image compensation are recommended.

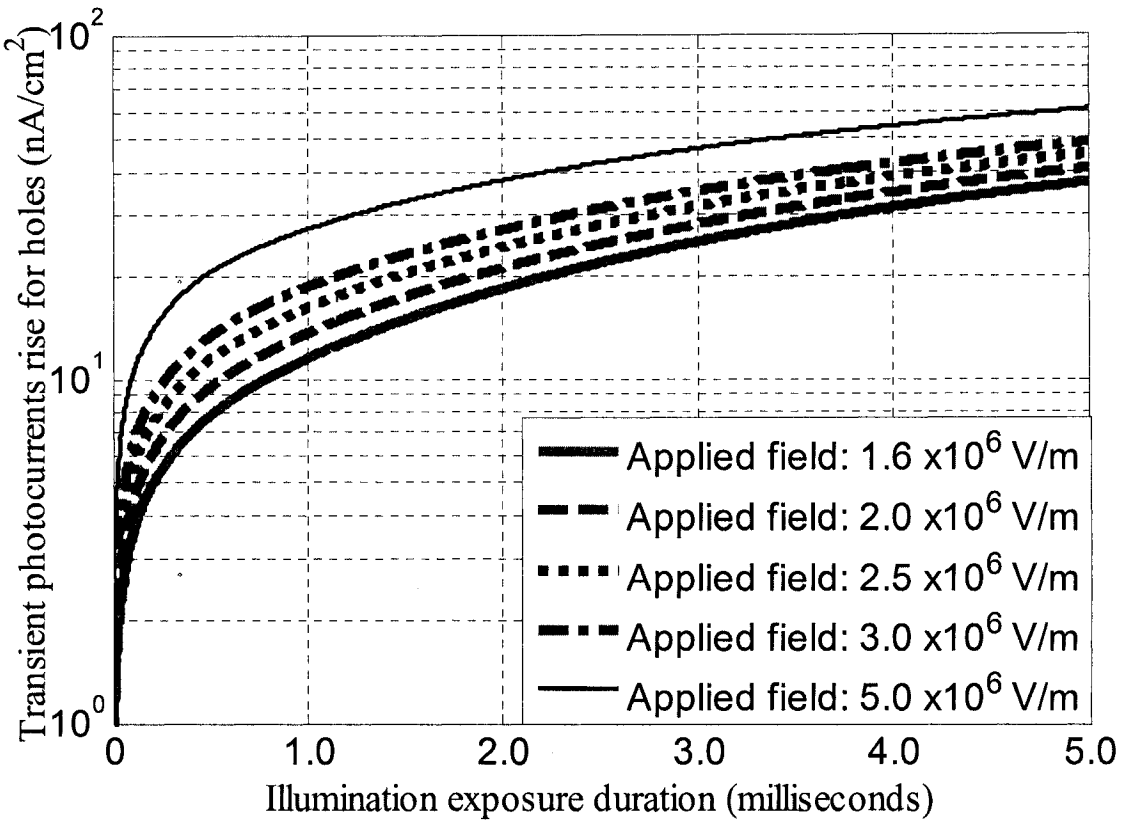

Figure 5.7: Transient photocurrents rise due to holes carrier at different fields in log scales, keeping same illumination exposure time (5 milliseconds) with generation rate 10^{14} $cm^{-2}s^{-1}$ and diode thickness, d=1 μm.

Although the above discussion got a technical basis for 5 milliseconds illumination but a longer illumination caused significant carriers trapping and de-trapping which caused fields ups and downs effects. This effect is shown in Figure 5.8, where exposure is taken 10 milliseconds. The photocurrent is significantly reduced and the trend is fully recombination mode. Eventually the photocurrent will be disappeared for further

illumination, because the recombination already become prominent over drifted current at the extended time. The field moves downward once carriers are trapped in the local traps (packet) centre and goes upward once carrier released. In principle, the photocurrents followed the field momentum results zigzag photocurrents and the lowering of photocurrent is about 4.1×10^{3} nA/cm^{2} as depicted in Figure 5.8.

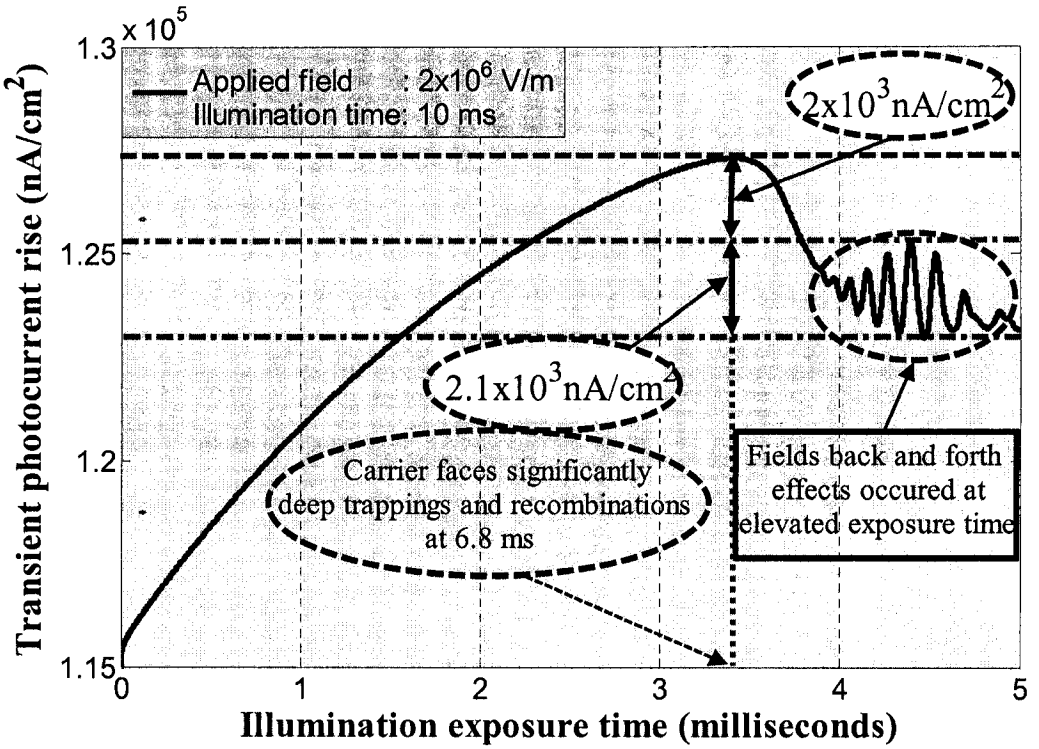

Figure 5.8: Photocurrent rise at longer illumination time with generation rate 10^{14} cm^{-2}s^{-1} and diode thickness, d=1 μm.

By physical examination in Figure 5.8, the field and therefore photocurrent suffered massive trapping/de-trapping consequences around 7.9 milliseconds, but the recombination already taken place at 6.8 milliseconds. This nature caused a noise dominated photoresponse, which is not good in any quality image productions in imaging technology. It is therefore suggested that there should be optimum exposure time for a

particular structure of PPDs, although the maximal photocurrent evident at 6.8 milliseconds, however, 5 milliseconds is a better choice for safe mode perspective.

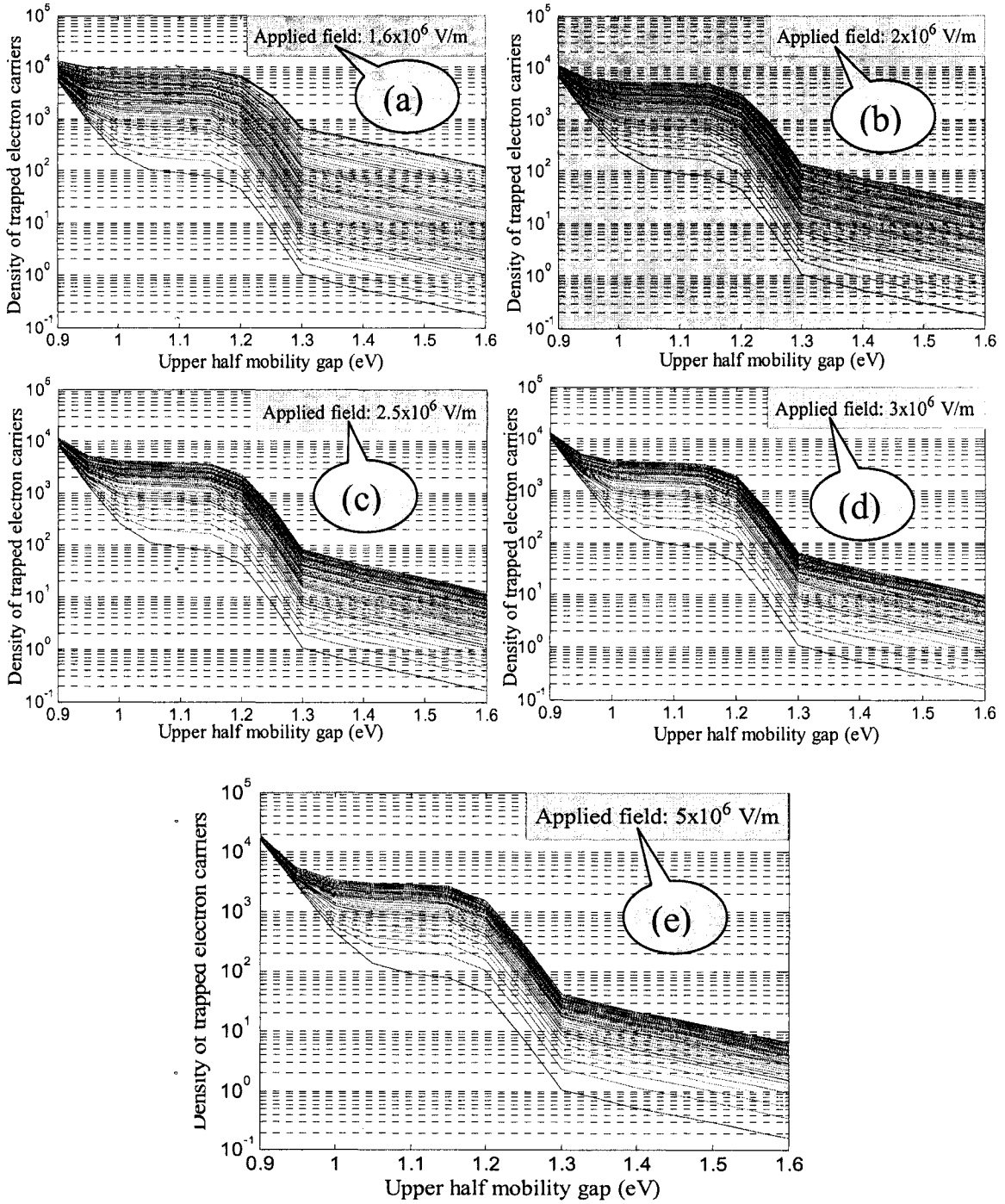

Figure 5.9: Graphical depictions of trapped electron carrier density at different field conditions in the upper half of mobility gap. The samples were illuminated for 5ms and the diode thickness is considered 1 μm with generation rate 10^{14} $cm^{-2}s^{-1}$.

More importantly, distribution of traps density of electrons have been graphically configured and shown in Figures 5.9(a)—5.9(e). As we explored the photocurrents in figure 5.6 and thereby depicted the responses increased a little bit with the fields, but how they are really mechanized inside the mobility gap at fully depleted intrinsic region. Presented simulator have the ability to depict graphical nature of trapped carrier densities for both carriers (electrons and holes) and are mapped as shown in Figure 5.9 and Figure 5.10.

Ideally the trapped carrier density should be minimum as much as possible for optimal photocurrents. After careful examination, it is explored that the dominated carriers (electrons) deep traps densities of states are decreasing with the increasing of fields, which means the carriers are swept away efficiently from the deep traps states of mobility gap that causes an adequate responses. In Figure 5.10, depicted the trapped holes distribution, where the deep trapped carriers are increased, but the band edge shallow interface trapped carriers remained almost the same. It is therefore a limited holes current contribution is realized to the response. However, those trapped holes latter on released at post illumination interval in the forms of residual currents and that causes the decay current to be dominated by holes.

In contrast between Figures 5.9 and Figure 5.10, the holes trapped carriers density is quite large than that of electrons at the same field implication. For instance, in the vicinity of deep trapping centers of Figure 5.9 (e), the deep trapped electron density is about 9×10^{3}, where as the trapped holes density as on Figure 5.10 (e) is more than 10^{6} with same implied field 5×10^{6} V/m. For amorphous silicon, $\mu_p>>\mu_e$, where μ_p is the hole mobility and μ_e is the electron mobility and therefore more holes are trapped in the

mobility gap for particular time of scan. As holes current $J_p \sim \mu_p$, and electrons current $J_e \sim \mu_e$, we experienced the electrons current dominated over holes current in total current measure.

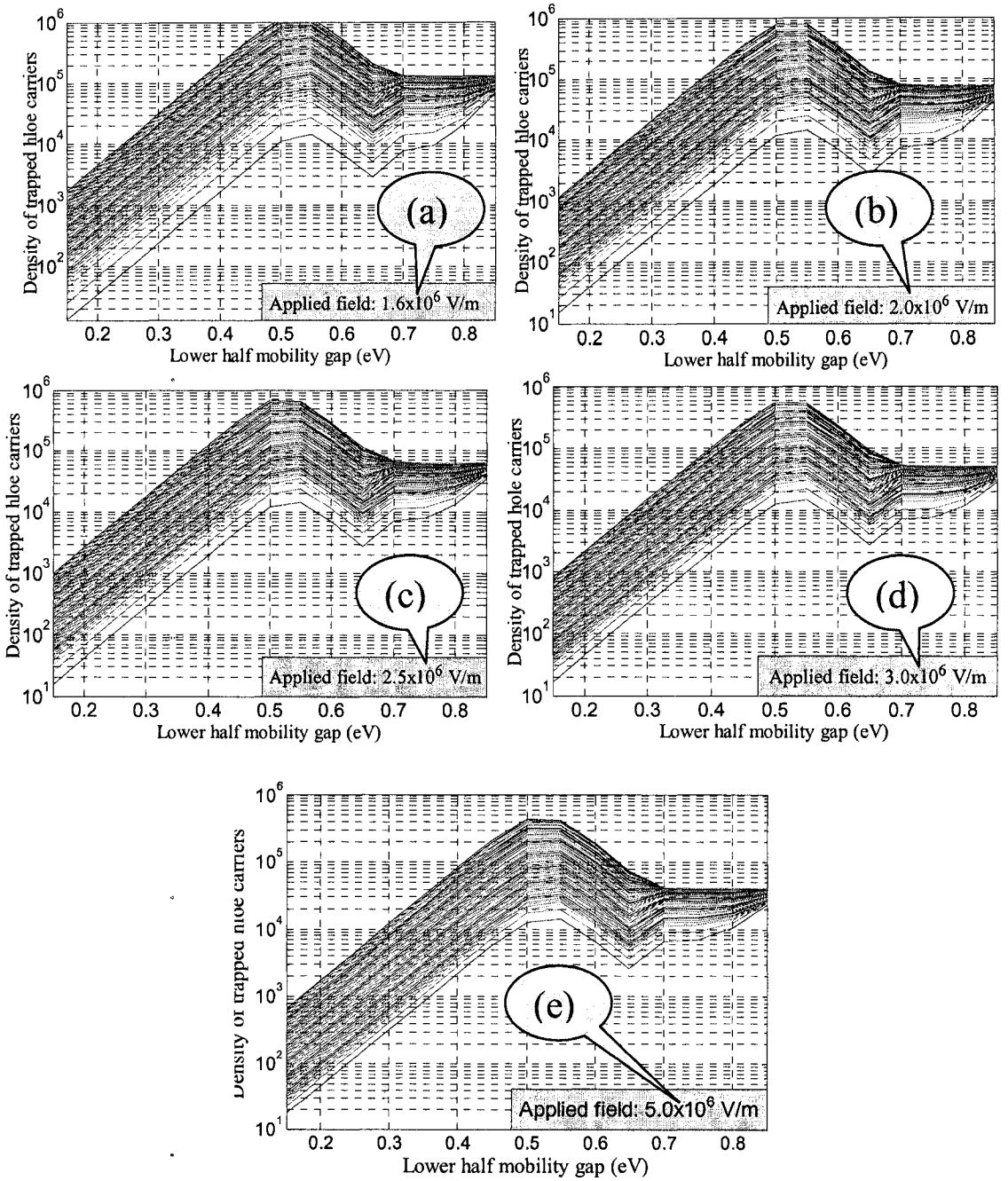

Figure 5.10: Holes traps density of states (levels) at different field conditions in the lower half of mobility gap. The illumination exposed for 5ms and the diode thickness are designed 1 μm basis with generation rate 10^{14} $cm^{-2}s^{-1}$.

In Figure 5.11, the photocurrents decays are shown at different fields. As the figure shows that the field has no significant affect to post illumination photocurrents decay, but the beauty is that all currents are met after certain time at a single line, i.e. apparently saturation occurred regardless of the field variation after about 1 milliseconds exposure. These photocurrent decays are fast enough to fluoroscopic use. During fluoroscopic procedure the detector is continually irradiated and polled by the accompanying electronics to form a real time image. Therefore, the longest carrier transit must be sufficiently short so that all charges in a pixel are collected by the time that pixel is next accessed.

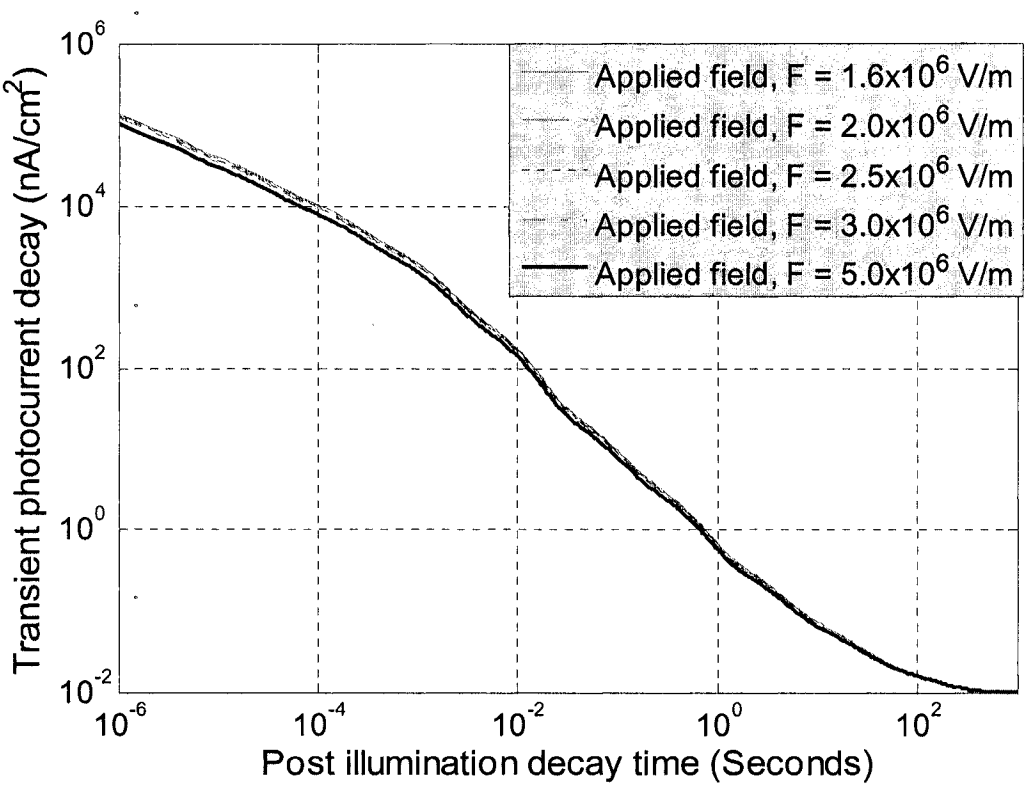

Figure 5.11: Transient photocurrents decay at different field implications. The diode was illuminated 5 ms and then turn off to visualize the decay (residual) currents. The diode thickness is designed to be 1 μm with generation rate 10^{14} $cm^{-2}s^{-1}$ basis.

5.1.2 Transient photoresponse dependency on Photodiode Thickness

As described in section 5.1.1, the transit time is a key measure to understand traps mechanism. Unlike the fields, photodiode thickness has also impacts on transit time of carriers but inversely i.e. the transit time increases with photodiode thickness. Several factors depend on photodiode thickness, for instance internal quantum efficiency, EHP generations, and transient photoresponse etc. The transit time is directly proportional to square of the photodiode thickness by,

$$\tau_T = d/\mu F \approx \tau_T = d^2/\mu V \tag{5.1}$$

On the other hand, once the free EHPs are created within the photodiode by converted visible photons. Ideally all should be collected at the electrodes to ensure exact detections of image signals. But in practice, the carriers are lost to some extent, due to recombination or by deep trappings. Recombination occurs when a drifting electrons and holes are met and recombine together. On the other hand, the carriers might be deeply trapped in the mobility gap and which was described by Schubweg ($\mu\tau f$) limited phenomenon in chapter 2 and chapter 4.

In order to maintain optimum charge collection, Schubweg ($\mu\tau F$) should be orders of photodiode thickness (d). Here, μ is the charge drift mobility, τ is the trapping time, and F is the applied electric field. By increasing the thickness, the photoconductor resistance will also be decreased according, results the same amorphous tends to behave a little bit crystalline inclined property, which degrade the photoconductive properties of the amorphous. As shown in Figure 5.12, the photocurrent increases with diode thickness, however the variation is not linear. More details are tabulated in Table 5.1.

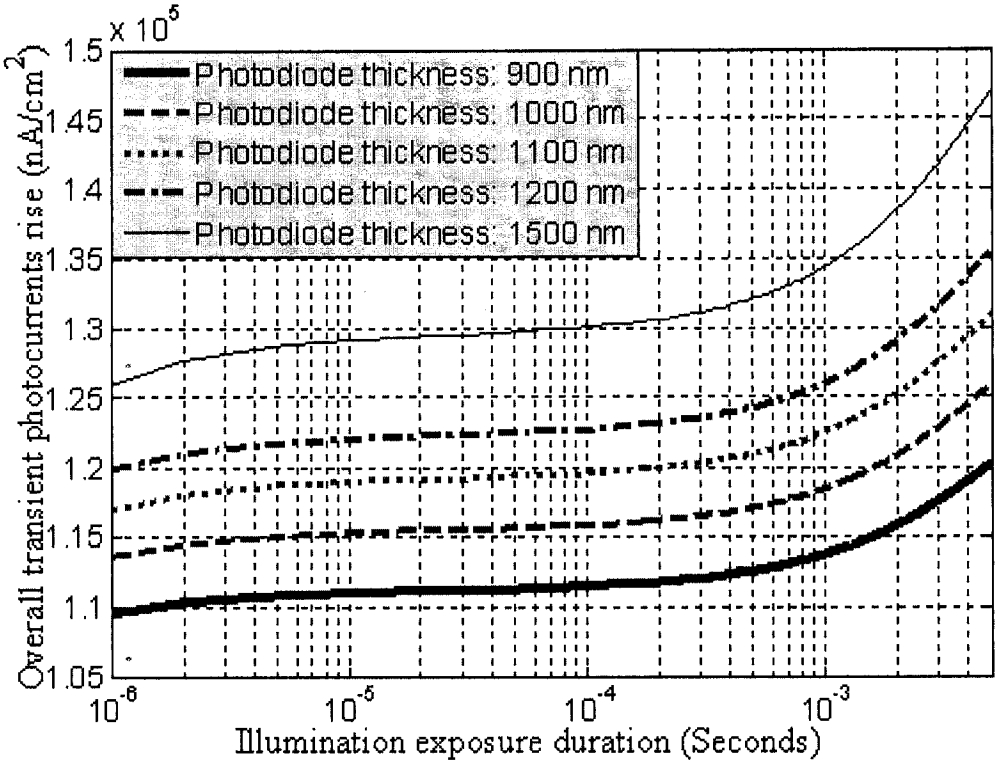

(a)

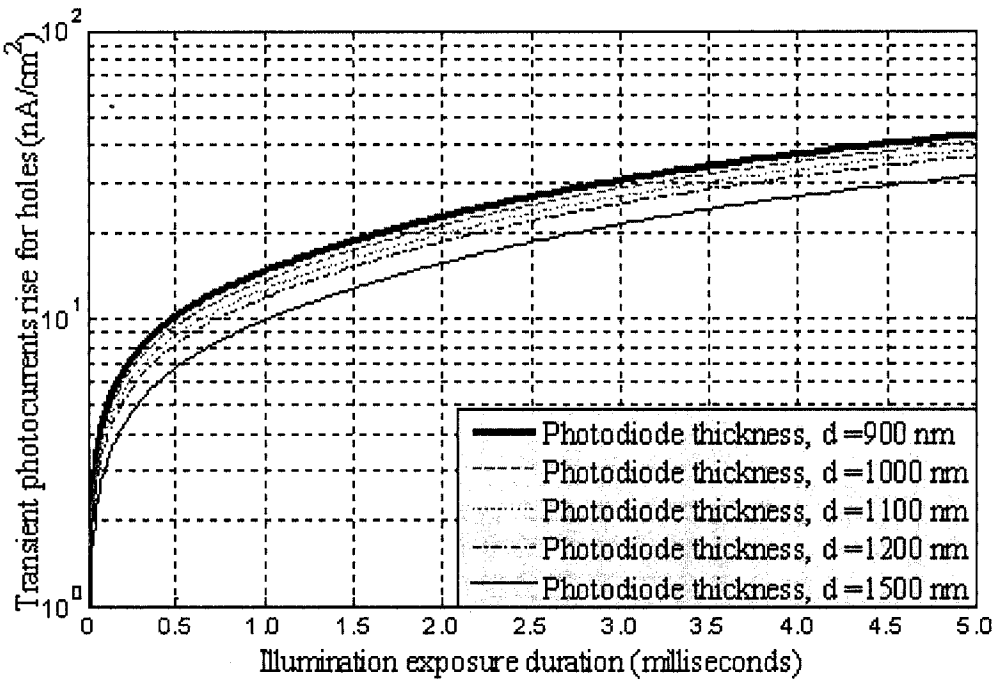

(b)

Figure 5.12: Transient photocurrents rise at different photodiode thickness (a) Overall (b) For holes only. The illumination exposed for 5ms and the applied field is 2×10^6 V/m with generation rate 10^{14} $cm^{-2}s^{-1}$.

From the table 5.1, it is evident that increasing the thickness beyond a permissible range raises a risk of loosing diode performance by massive bulk recombination as we explained in chapter 2 and chapter 4. Also the range of diode thickness should allow the incoming photons interaction within the silicon to induce EHP. Based on our results, it is suggested that 1 μm is a preferable choice for avoiding any adverse situation in the active layer of the pixel photodiode.

Table 5.1: Photodiode thickness (d) impacts on photocurrents (I_{ph}).

Photodiode thickness, d (μm)	Photocurrents, I_{ph} (nA/cm^2)	Thickness (d) variation in %	Photocurrent variation in %	Remarks
1.0	1.27×10^5	Reference (d)	Reference (I_{ph})	We consider sample thickness 1 μm
0.9	1.21×10^5	-10	-4.72	
1.1	1.31×10^5	10	3.15	
1.2	1.36×10^5	20	7.09	
1.4	1.47×10^5	40	15.75	

In Figure 5.13, the electrons traps densities within the mobility gap at various diode thicknesses are shown graphically. Careful examination reveals that the deep traps are reducing with increasing of diode thickness. On the other hand, the interface shallow trapped carrier densities are reduced insignificantly. Therefore, a large diode thickness results a higher photocurrent in the diode. If only thickness is increased without appropriate selections of fields, the transit time will be increased, and the photocurrent may not be resulted. Rather massive bulk recombination and deep traps are obvious at the end. Because for carriers collection there should be optimal Schonberg/photodiode thickness ($\mu\tau F$)/d) ratio, i.e. should maintain '$\mu\tau F >>$ d' in order to have photocurrent.

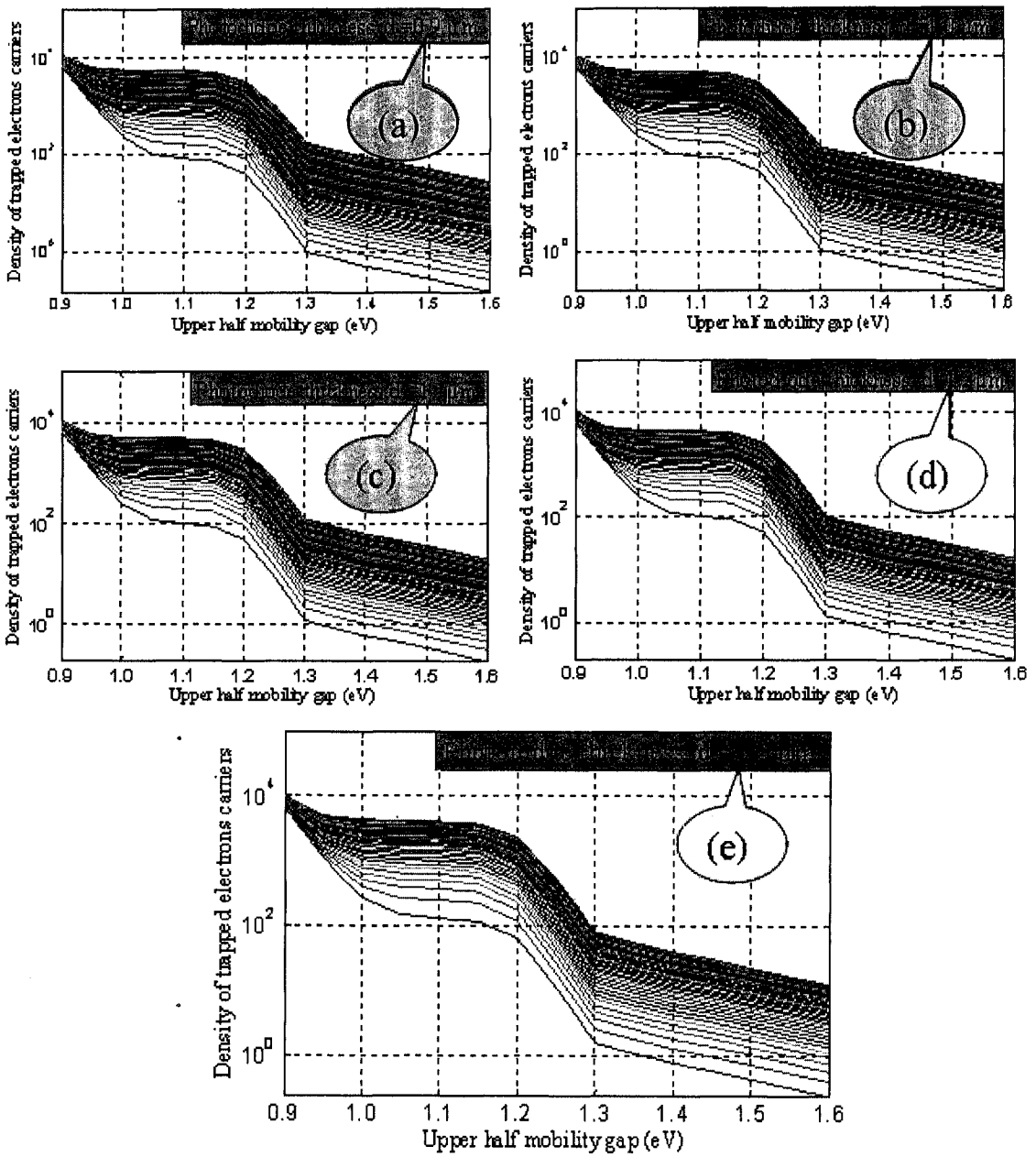

Figure 5.13: Density of trapped electron carriers in the upper half of mobility gap at different photodiode thickness. The illumination exposed for 5ms and the applied field is 2×10^{6} V/m with generation rate 10^{14} $cm^{-2}s^{-1}$.

In Figure 5.14, trapped holes carrier densities of states are shown in different photodiode thickness. By physical examination reveals that the total holes trapped carriers are increased with photodiode thickness in the mobility gap and therefore the

holes photocurrent decreases (Figure 5.12(b)) with increase of diode thickness. Because an increase of photodiode thickness results higher transit time and the probability to traps increase, especially is more obvious for slow moving carriers like holes.

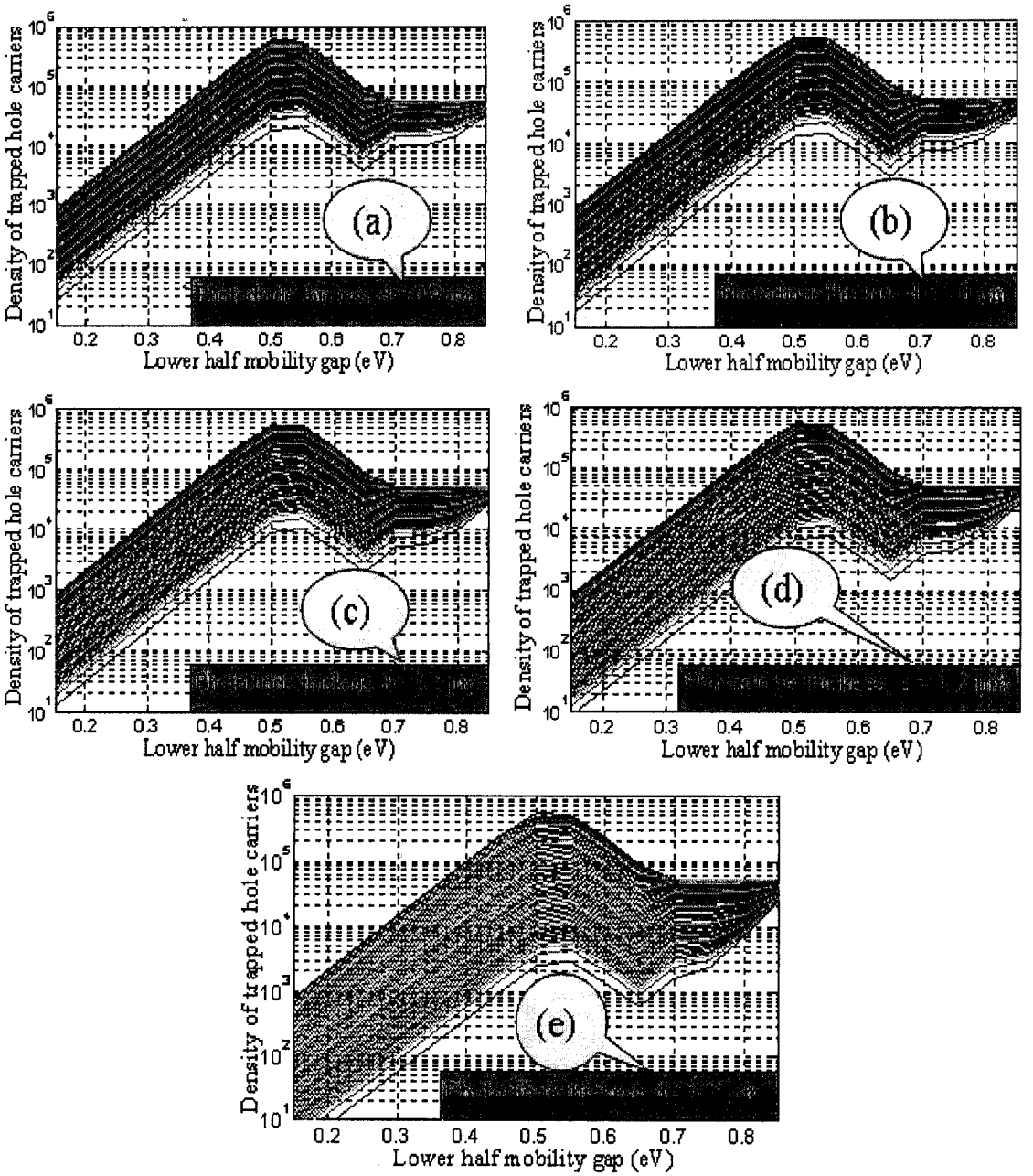

Figure 5.14: Holes traps density of states (levels) in the lower half of mobility gap with different photodiode thickness. The illumination exposed for 5ms and the applied field is 2×10^6 V/m with generation rate 10^{14} $cm^{-2}s^{-1}$.

The transient photocurrent decay is barely dependent on the thickness of the photodiode. As shown in the Figure 5.15, there is no significant difference between decays. Although the saturation in decays occurred after 1 second regardless diode thickness, however, it is fair enough to conclude that there is no obvious benefit to increase diode thickness. Rather lower possible thickness is better option to avoid any massive trapping inside the bulk until the photon stopping effectively demonstrated.

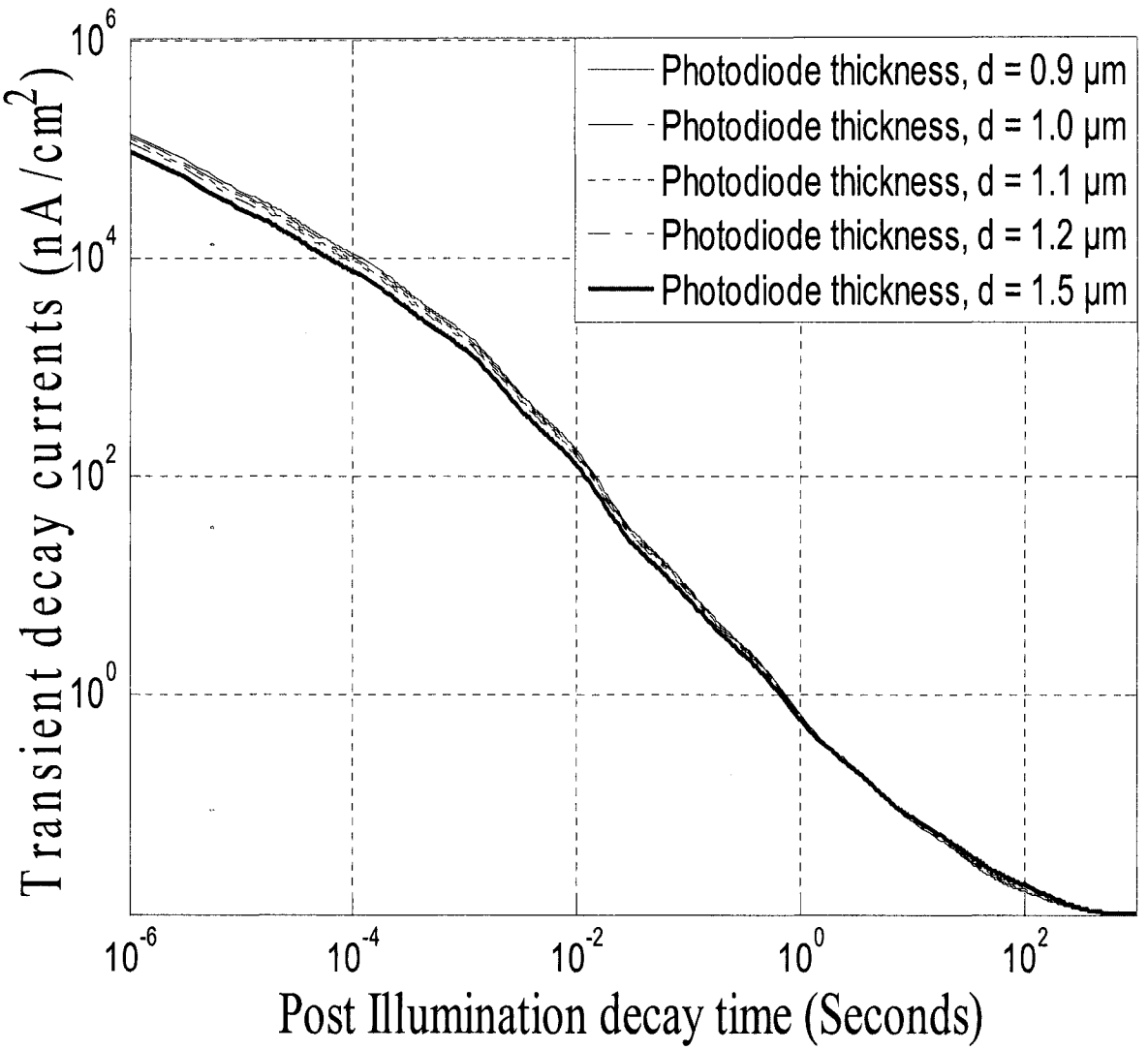

Figure 5.15: Transient photocurrents decay at different pixel photodiode thickness. The diode was illuminated 5 milliseconds at an applied field 2×10^6 V/m with generation rate $10^{14}cm^{-2}s^{-1}$and then turn off to visualize the decay currents at different diode thickness.

5.1.3 Dose impacts analysis on pixilated a-Si:H-PD

In radiology, dose term has been used in the sense of photon fluence, i.e. the energy or amount of photons per unit area received by an irradiated object during a particular exposure time. The photon fluence itself is the integral of the amount of all photons (quanta), which traverse a small, transparent, imaginary spherical target, divided by the cross-sectional area of this target. If photon fluence rate is E_p^0, then the photon fluence (H_p^0) is simply integrated over time t is,

$$H_p^0 = \int_0^t E_p^0 dt \approx E_p^0 t \therefore E_p^0 = H_p^0 / t \tag{5.2}$$

In this work, Q is symbolized for total carriers that is created by the photons fluence rate E_p^0 and carriers generation rate in the photodiode is $Q_0 = Q/(A.t) \approx H_p^0/t$ during irradiation, where A is the surface area of photodiode and t is the time that allowed to irradiate. In real life, when reverse biased a-Si:H p-i-n photodiode irradiated with appropriate photons fluence, it creates electron-hole pairs (EHP) in the fully depleted intrinsic region. The applied bias on photodiode sweep out those generated electrons and holes to electrodes results a photocurrent.

The resulted response is dominated by electron carriers as the mobility of electrons is about 10 times greater than the holes mobility. The overall photoresponses at different doses are shown in Figure 5.16 (a). The photocurrents are increased in regular fashion with doses and the holes contributions to the overall responses are depicted in Figure 5.16(b). After keen observation, we found that the photocurrent at high doses

$(8\times10^{14}cm^{-2}s^{-1})$ has suffered a massive trapping. We mentioned in earlier chapters that the amorphous silicon has no distinct energy gap, instead mobility gap inherently with traps centers presumed in amorphous solid-state physics.

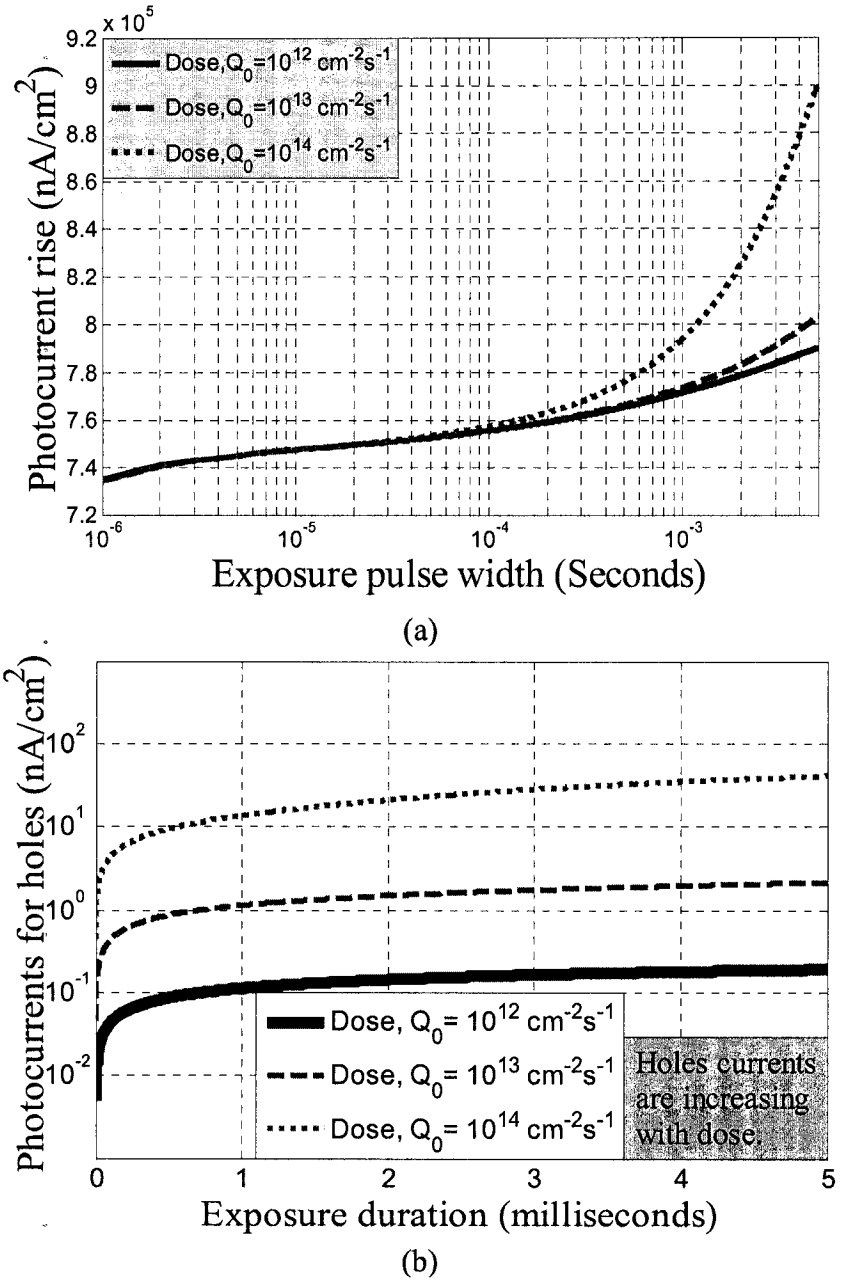

Figure 5.16: Transient photocurrents rise at different doses (a) Overall photoresponses *versus* illumination time (in log time scale) (b) Holes photocurrent (in log time scale) *versus* illumination time.

In the mobility gap, as mentioned before that there are so many traps centre or states available that can traps the carriers stochastically before reaching to the respective device terminals. Some of these traps are seated permanently at least for the time of interest, i.e. within the collection clock cycles. It is become more prominent when higher doses imposed onto a particular photoconductor having significant traps centre, like a-Si. The collectable significant number of carriers are being accommodates in the traps centers resulted an early downing of the photoresponses. However, initially shallow states fillings constitute a linear increment of photocurrents are emerged and visualized in Figure 5.17.

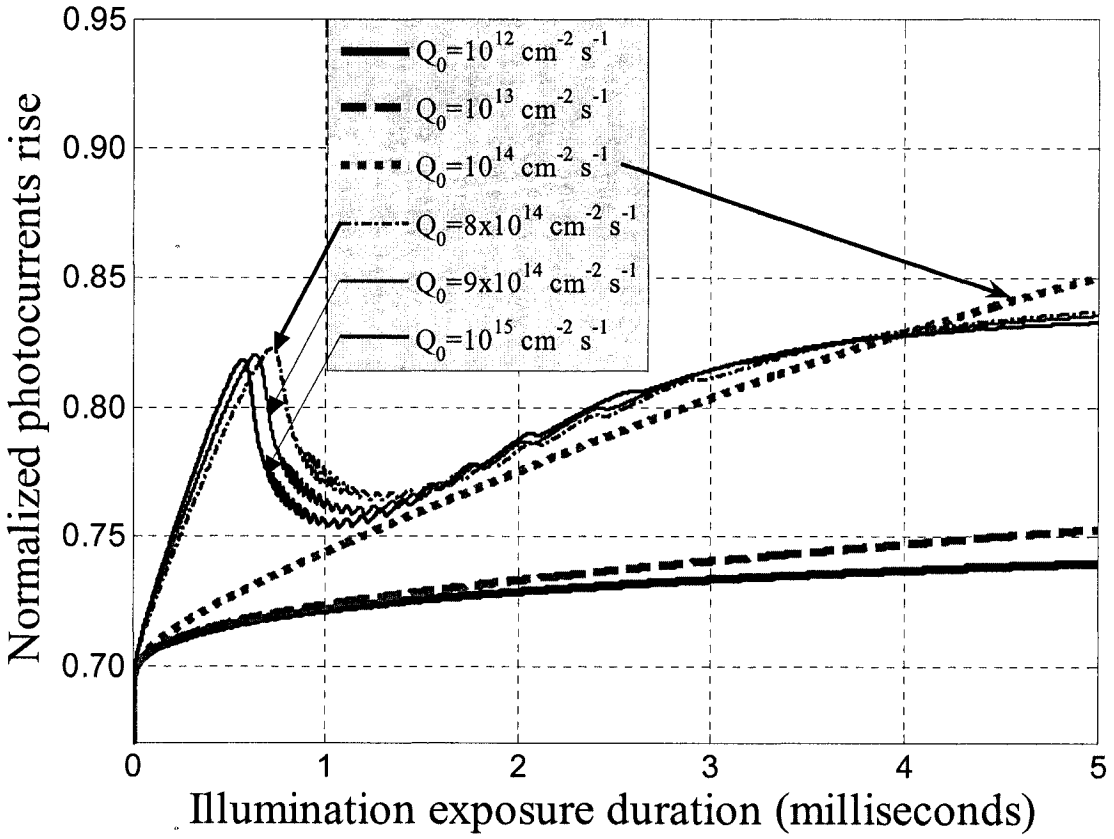

Figure 5.17: Normalized overall rise currents at different doses. An 1 μm (thickness) pixel photodiode was illuminated for 5 ms with applied field 2×10^6 V/m.

To avid any massive trapping, there should be implied a permissible dose in respect of diode features in order to ensure optimized photoresponses. As mentioned before, active layer thickness of p-i-n photodiode has a nominal contribution to the overall transient photoresponse at reverse bias condition and it is well understood once look at figures Figure 5.16(a) and Figure 5.16(b). From the Figure 5.17, it is simply understood that the photoresponse is not well in shape neither in the beginning, nor in the end of transient photoresponse at higher dose implications.

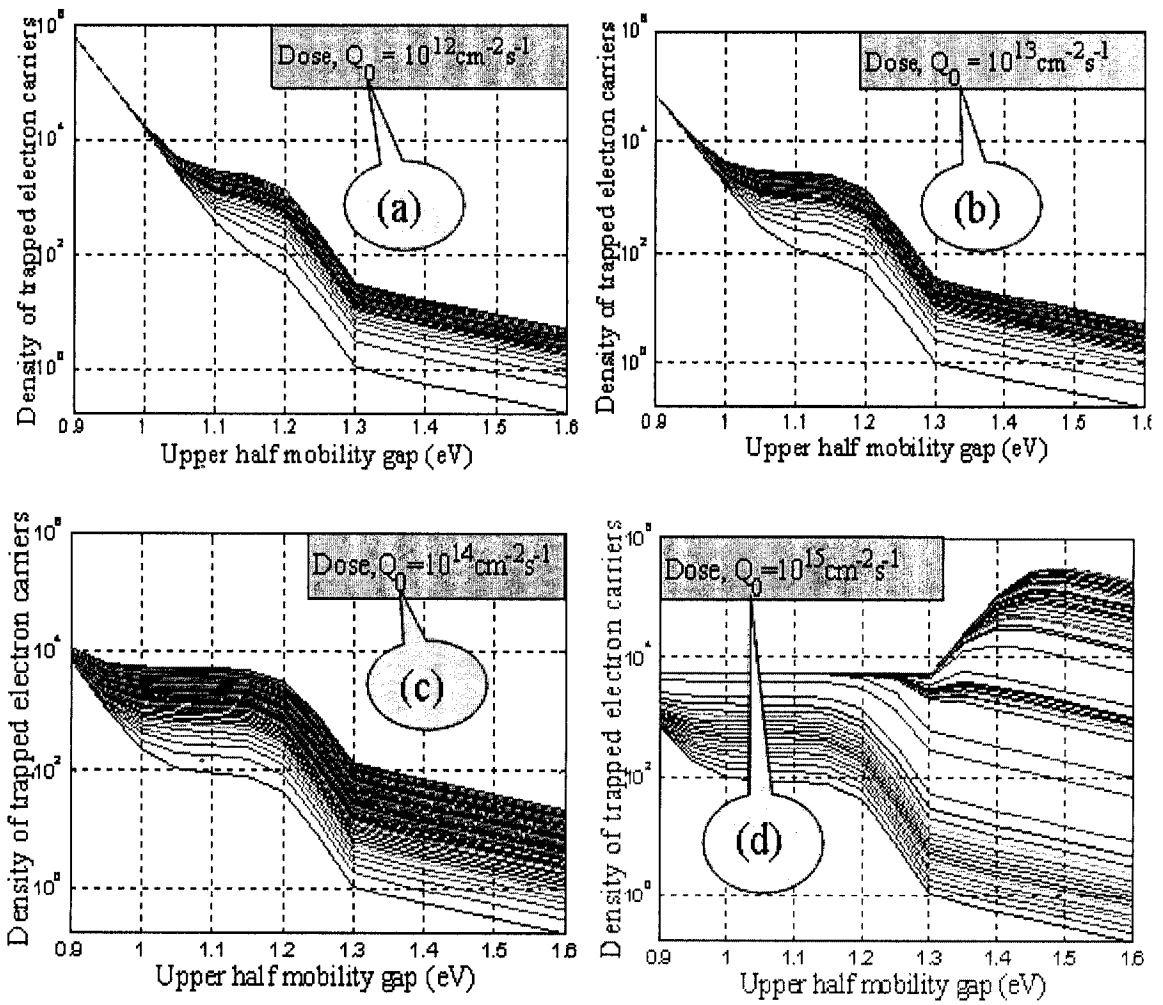

Figure 5.18: Trapped electrons density inside the mobility gap at different doses. An 1 μm (thickness) pixel photodiode was illuminated for 5 ms with applied field 2×10^6 V/m.

In the beginning, the deep-trapped carriers are kept in trapped and so does similar impacts in the final response, even its quasi-state margin is lower than that of lower dose implications. On the other hand, holes currents increases in regular fashion, because inherent low mobility holes may not reach through when faster electrons already accomplished its journey to the respective electrodes within the specific time frame. Our simulated results promoted that the dose around $10^{14}cm^{-2}s^{-1}$ is an optimal choice being ensured good temporal photoresponse for a-Si:H PPD for a particular diode (Figure 5.1) in image realization.

In Figure 5.18, the trapped electrons density is shown, where deep-trapped density are decreased substantially, however the total trapped carriers are increased in the mobility gap with higher dose implications. Although the photocurrent increased up to implied generation rate is $10^{14}cm^{-2}s^{-1}$, but the trend of trapped carriers density dictates that the photocurrent might not continue to increase to an elevated dose implications. Eventually, we found the same phenomenon once dose increase to $10^{15}cm^{-2}s^{-1}$ as shown in Figure 5.18 (d) and the current drawn to a lower magnitude than that of $10^{14}cm^{-2}s^{-1}$ dose implication as depicted in Figure 5.17.

This result is most likely due to the deep-trapped centre shifted to the mid-gap area of the mobility gap, constituted a deep-trapped like phenomenon. Because the deep trapped electron density significantly reduced in the centre and probably some deep trapped carriers tried to release from their deep pocket and attempt to or already join to the conduction stream. More likely at the moment of shallow states charges trappings-detrapping cross-over vicinity, the carriers secondarily fall back somehow to

comparatively deeper states and are unable to escape/reach to the conduction stream for at least within the time of interest.

The similarity between Figure 5.18 (d) and Figure 5.23(d) signify high dose and long exposure have the same adverse effect which will be discussed latter on in section 5.1.4. It is further defined from the Figure 5.19, where deep trapped carrier (hole) density are decreased and shallow interface increased results a limited contribution to the to the overall response. Therefore, the holes currents are increasing as depicted in Figure 5.16 (b) limitedly.

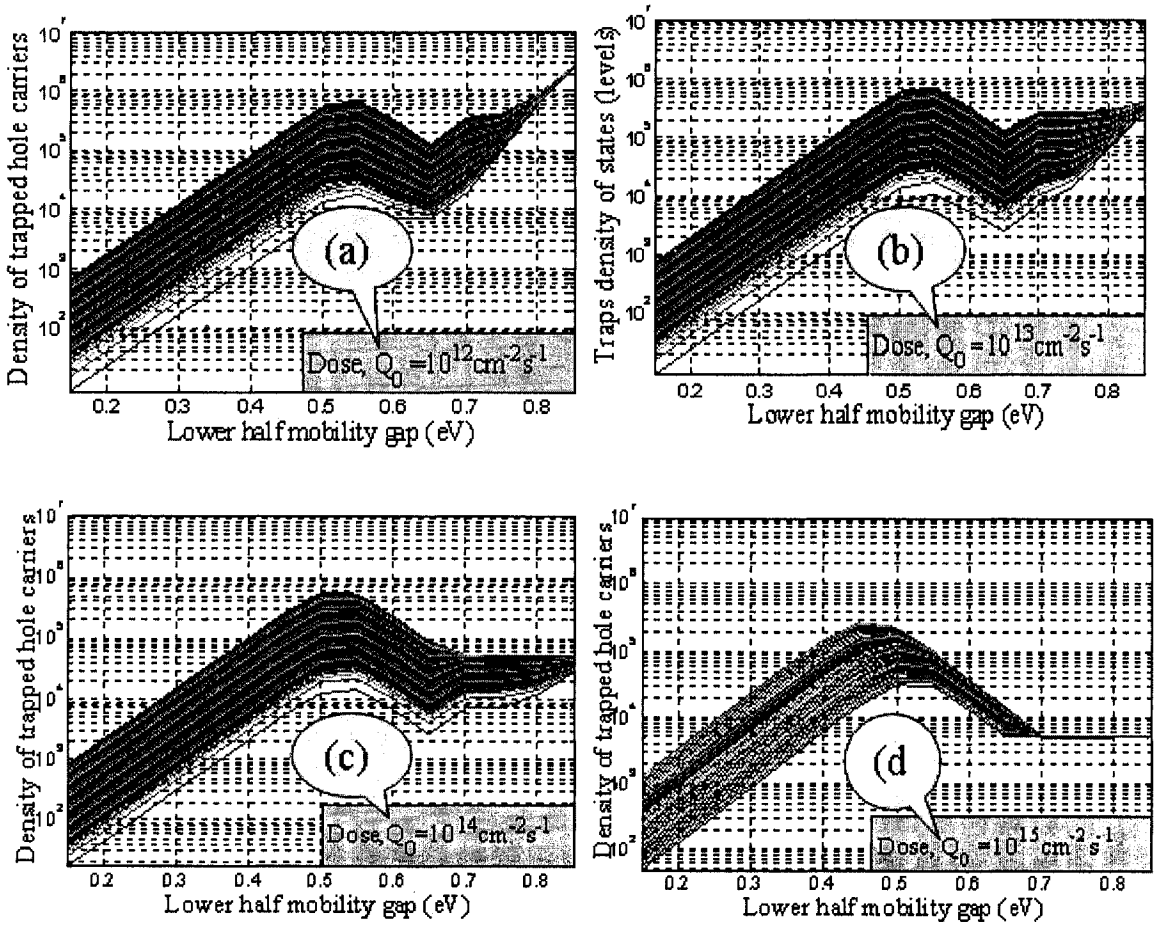

Figure 5.19: Trapped holes density inside the mobility gap at different doses, when an 1 μm (thickness) pixel photodiode was illuminated for 5 ms with applied field 2×10^6 V/m.

In Figure 5.20, the results showed the photocurrents decay for different dose conditions. Initially the decay photocurrents are decreased when dose decreases. More interestingly photoresponses are decayed reasonably faster and ended up at the same spatial time, which is good enough to fluoroscopic use in radiology. The initial decay current at dose 10^{15} $cm^{-2}s^{-1}$ has been extracted about 10^{8} nA/cm^{2}, which is one order higher than that of previous trend of enhancement. After careful examination, this extra residual current is more likely the same as trapped carriers (see Figure 5.18(d)), which caused lowering the rise current as experienced in Figure 5.17.

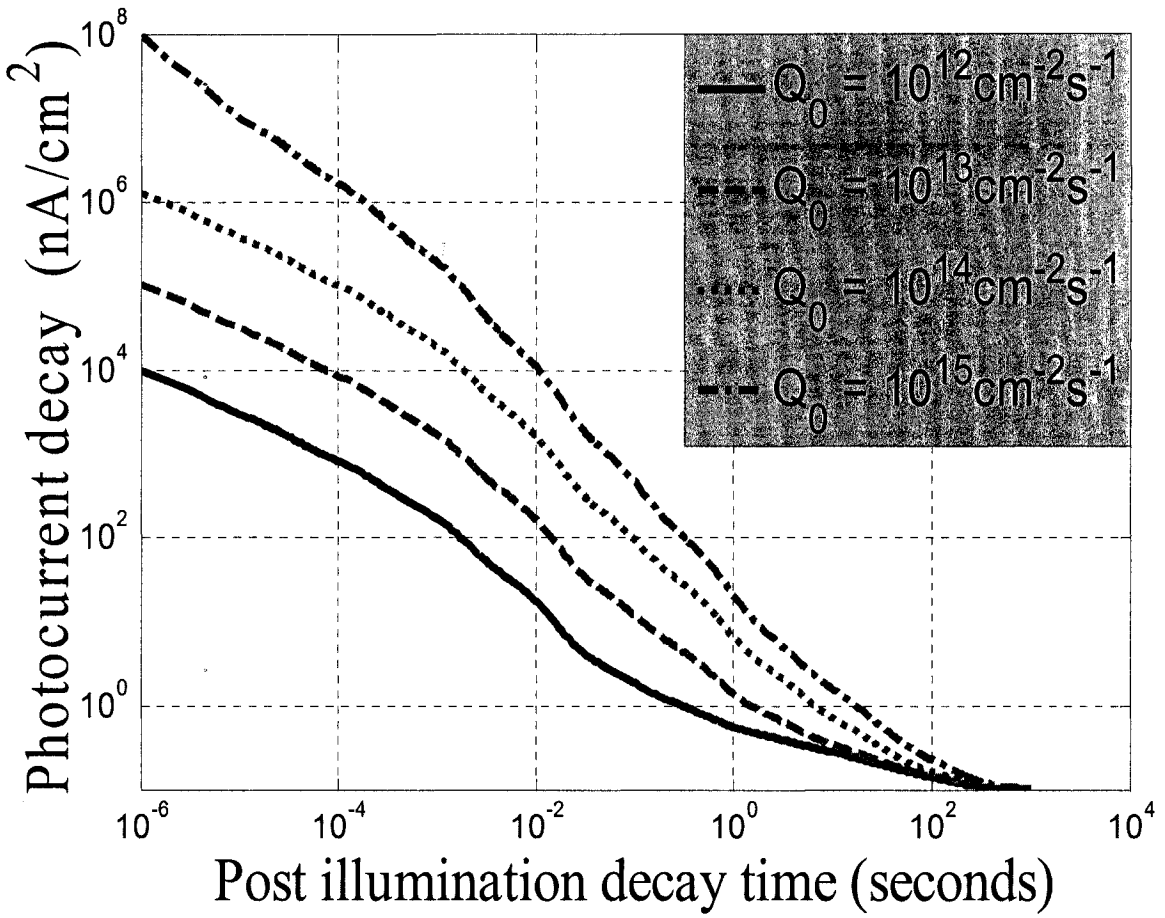

Figure 5.20: Overall photocurrents decay of a-Si:H photodiode at different doses. An 1 μm (thickness) pixel photodiode was illuminated for 5 ms with applied field 2×10^{6} V/m.

5.1.4 Exposure dependency of a-Si:H-PD at pixilated arena

The illumination time dependency to transient photoresponse is a dominant objective in designing a-Si:H x-ray imaging pixel sensor. In this section, we kept all parameters unchanged except the exposure duration (illumination time) so that the impacts of illumination time on photoresponse can be realized for AMFP pixel photodiode operation. The transient photoresponses are shown in Figure 5.21 for different exposure time.

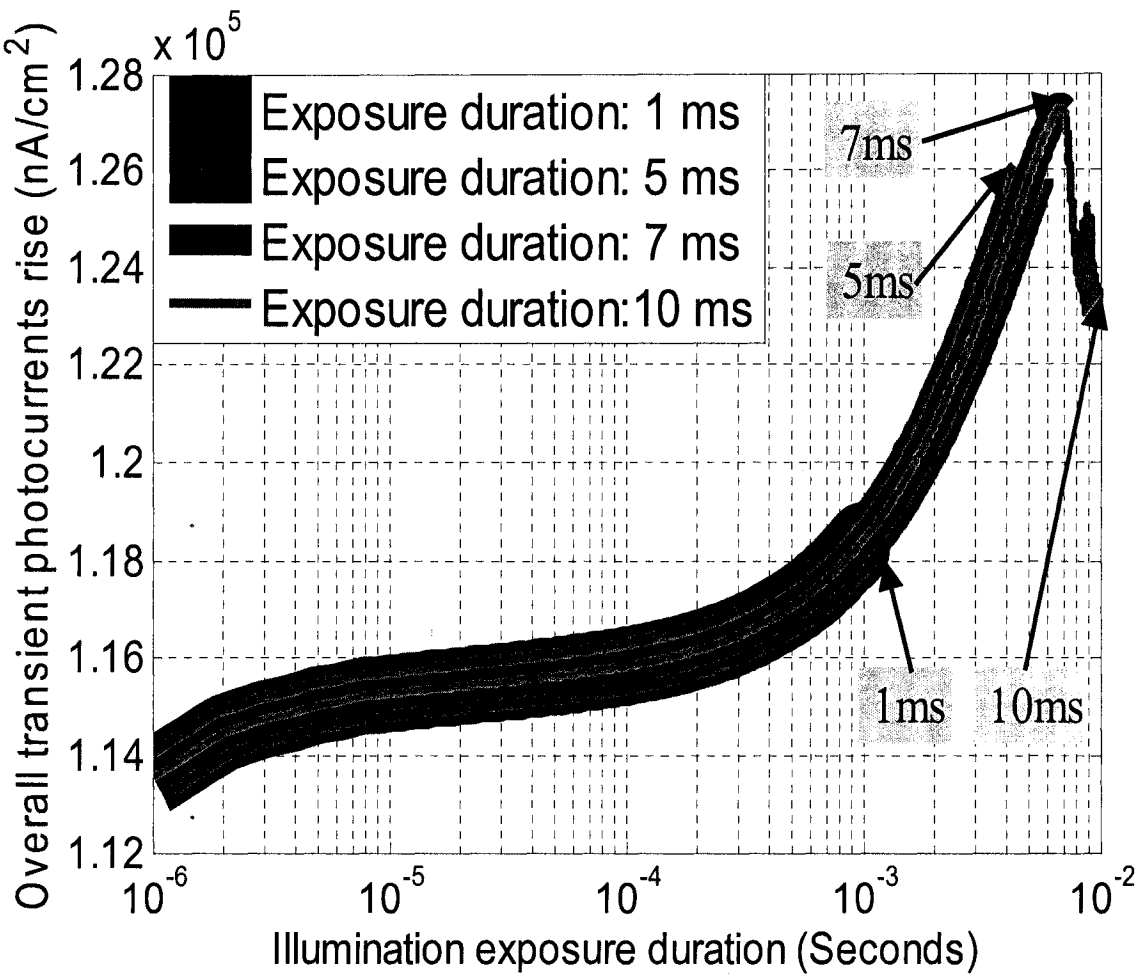

Figure 5.21: Overall photocurrents rise at different exposure duration, maintaining all other parameters unchanged. An 1 μm (thickness) pixel photodiode was illuminated at an applied field 2×10^6 V/m with generation rate $10^{14}cm^{-2}s^{-1}$.

The results ensured fair increments of photocurrents up to about 6.8 milliseconds but further extended time, the temporal response suffered massive recombination and deep-trapped like situation occurred. These phenomenon results significant noise addition into the system and emerged from Figure 5.8. Unlike previous discussion, holes contribution has no major contribution to the overall photoresponse and the ratios between overall current to holes current is about 2000 at par highest magnitude (see figure 5.22). Because the holes carriers propagated slowly as they have inherent low enough mobility with respect of electron and before reaching to the quasi-state holes current, there's arrived another session for illumination. Eventually no scope for full carrier collection being spatially time limited in high speed operation.

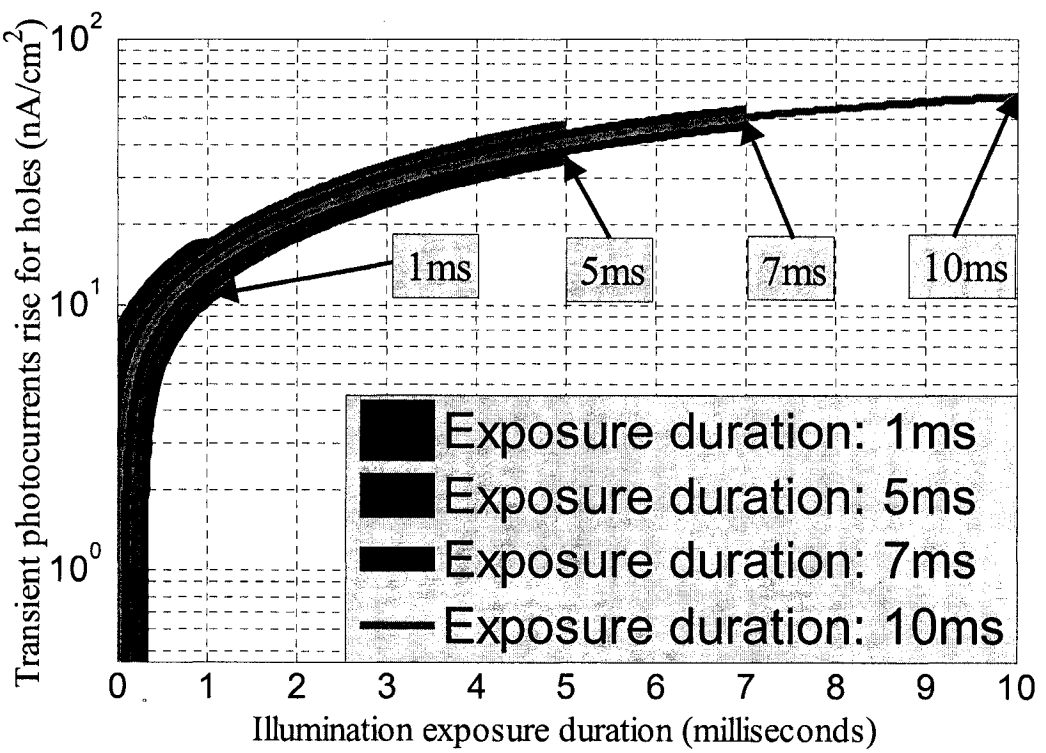

Figure 5.22: Holes responsible photocurrent rise at different illumination time. A 1 μm (thickness) pixel photodiode was illuminated at an applied field 2×10^6 V/m with generation rate $10^{14}cm^{-2}s^{-1}$.

Therefore, the holes carriers are not fully collected and not even fully contributed to the overall photoresponse within the time of switching interest and therefore we experienced decay current holes dominated (Figure 5.25 (a)). There is only option to collects all the holes carrier by increasing illumination time, but it is not feasible as there is definite possibility for massive electron carriers bulk recombination and deep trapped enhancement that already took place after 6.8 milliseconds as shown in Figure 5.21. From Figure 5.23, the traps densities of states for electron are shown.

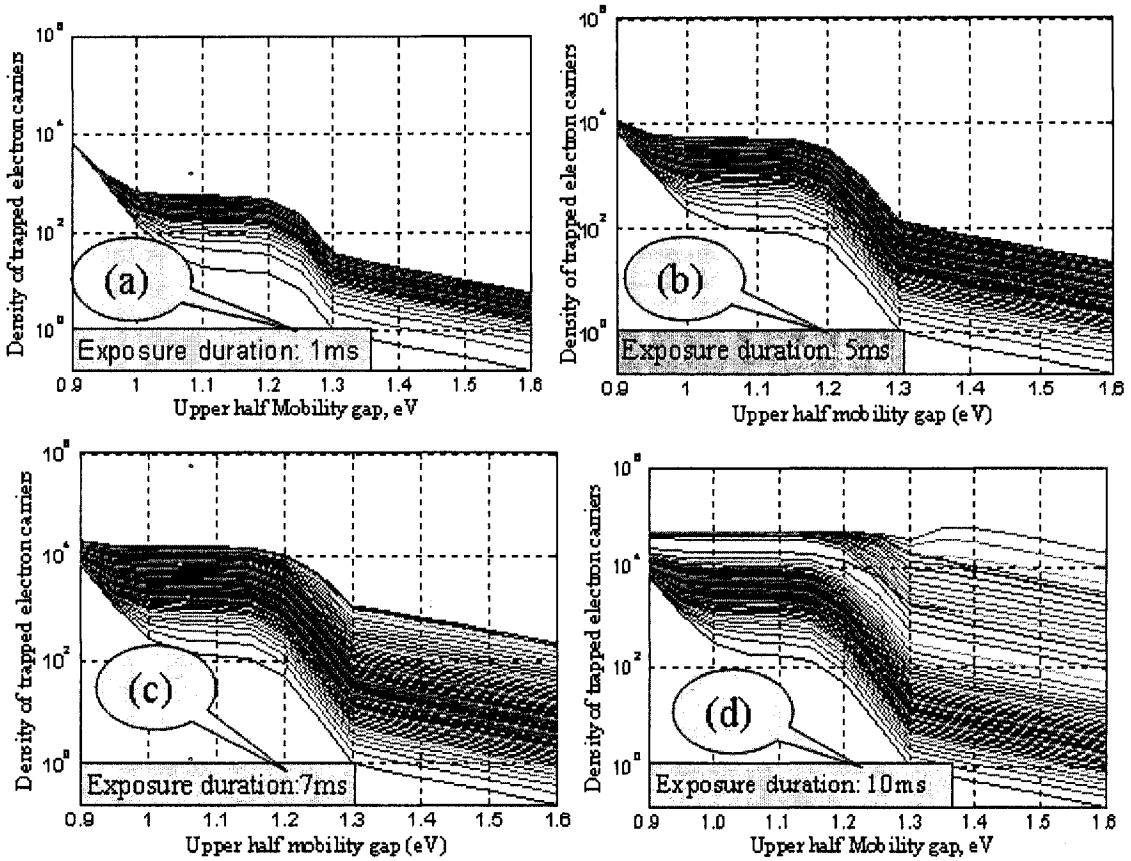

Figure 5.23: Trapped electron distribution inside the mobility gap at different illumination time. An 1 μm (thickness) pixel photodiode was illuminated at an applied field 2×10^{6} V/m with generation rate $10^{14}cm^{-2}s^{-1}$.

The deep traps electron carriers density are increasing as well as overall density, consequently a limited time of span photocurrent may increase, but later on photocurrent decrement is obvious. On the other hand, the holes deep-trapped carrier density increases, but the overall density decreasing insignificantly (Figure 5.24); therefore the hole current should be increased (see Figure 5.22) limitedly.

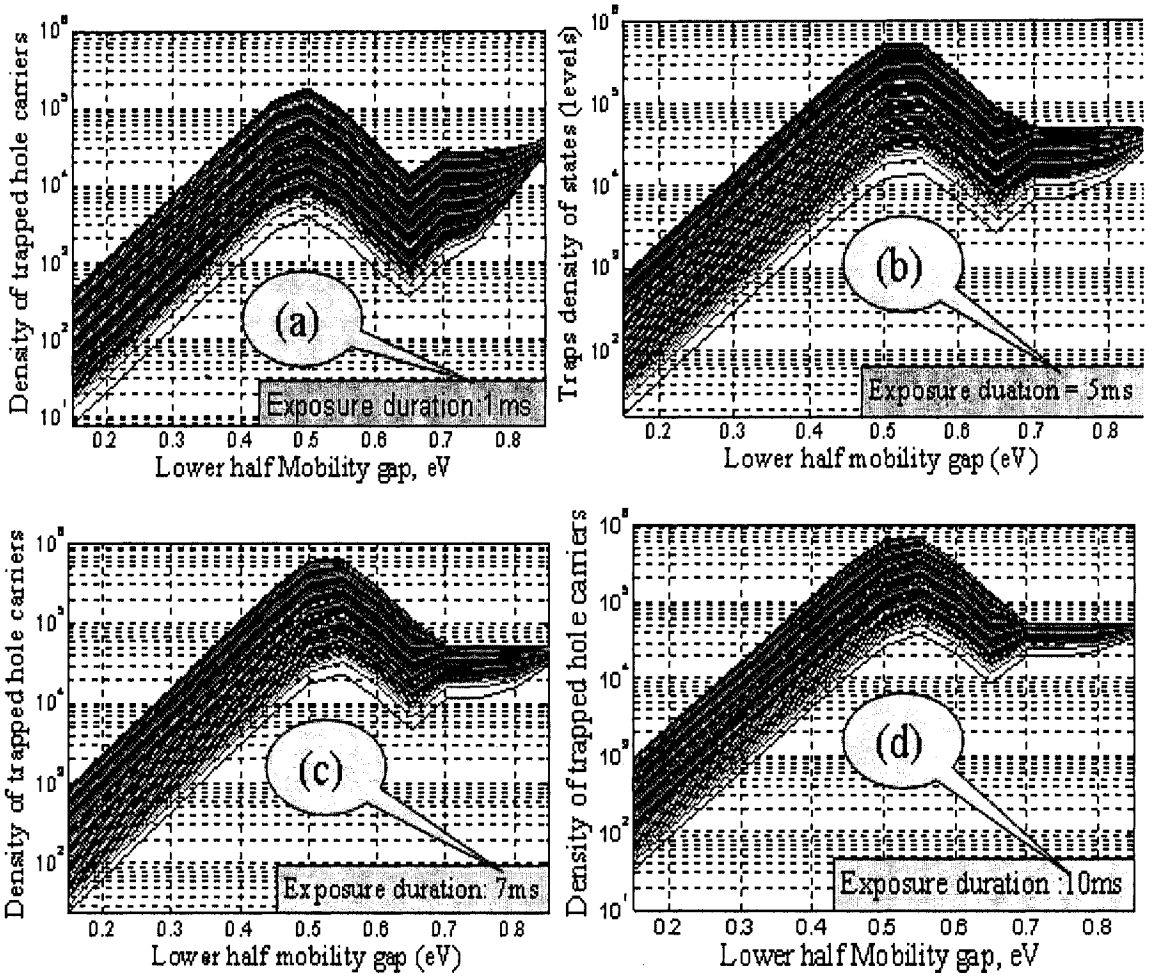

Figure 5.24: Trapped holes distribution inside the mobility gap at different illumination time. A 1 μm (thickness) pixel photodiode was illuminated at an applied field 2×10^6 V/m with generation rate $10^{14}cm^{-2}s^{-1}$.

In Figure 5.25 (b), the overall transient photocurrent (PC) decays are shown at different illumination exposure time. We found that photocurrent (PC) decay takes

comparatively less time in case of low time exposure time, and vice-versa. However for higher illumination time, all the decays showed saturated behavior i.e. all PC decays are followed close paths and the differences are not even distinguishable.

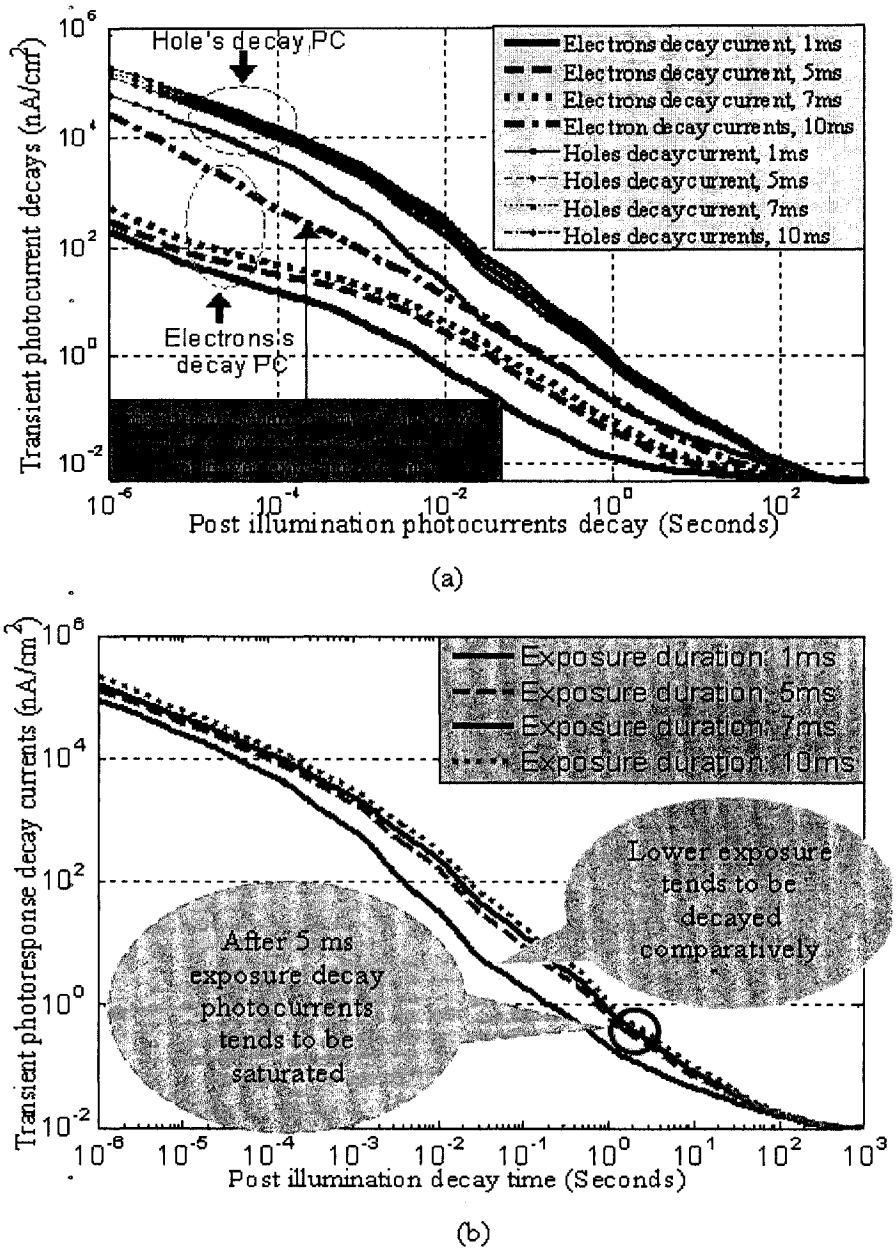

Figure 5.25: Photoresponse of a-Si:H photodiode at different illumination time (a) individual depiction of electrons and holes decay currents. (b) Overall photocurrents. An 1 μm (thickness) pixel photodiode was illuminated at an applied field 2×10^6 V/m with generation rate $10^{14}cm^{-2}s^{-1}$.

In Figure 5.25 (a), the individual carriers (electrons and holes) contribution to decay currents are shown. Most importantly the electrons decay current for 10 ms exposure got significant boost up and inconsistent with previous trends of increments. After careful examination, we concluded that this current most probably comes up from released trapped electrons (Figure 5.22), as there was significant loss that had been experienced after 6.8 milliseconds exposure. Therefore, it is understood that the photocurrent decay is limited to some extent for particular device operation by illumination time and the rise current is limited as well.

5.2 Summary

This chapter presented systematic soft-hand simulative tests on a-Si:H pixel sensor for diagnostic x-ray medical imaging. The design parameters have been optimized by customized simulator by means of soft-hand experiments in order to accomplished optimal design, in-situ characterized amorphous photodiode in integrated pixel arena. The simulator fully customized on conventional continuity equation and thereby the simulator itself has been acted as a soft-hand operable pixel sensor. The pixel photodiode has been analyzed by changing applied fields, active layer thickness, dose implications, and exposure time impacts. Finally, we concluded an 1 μm (active layer thickness) a-Si:H photodiode biased by 2 V/μm with implied dose 10^{14} $cm^{-2}s^{-1}$ should be delivered optimal photocurrents if illumination time continued over 5ms ~ 6.8 ms. In fact these are the phenomenal factor for efficient operation of pixel operation in diagnostic applications, more precisely in radiology.

Chapter 6: Summary, Conclusion, and Future Works

6.1 Summary & Conclusions

In this thesis, the models for determining optimal transient photoresponse of integrated p-i-n photodiode in a-Si:H pixel were developed for active matrix flat panel image detector by considering the combined effects of charge transport properties of the photodiode, operating conditions, and the geometry. The modeling works in this thesis are based on the physics of the particulate entity phenomena and the systematic solution of the fundamental quantum equations in the amorphous photodiode with: (1) Semiconductor continuity equation (2) Poisson's equation (3) Trapping rate equations. The modeling work has examined how the transient characteristics changed with crucial operating parameters and detector geometry varying condition in order to predict an optimal design and made available appropriate design portfolio before in-hand fabrication.

Numerical model based customized simulator code was written within matlab program facility and deployed to tests the delivered model. The simulator was designed generally to be able to handle all possible parameters optimizations in different photodetectors (viz. a-Si, a-Se, poly-HgI_2 and ploy-CdZnTe) for diagnostic applications. However, in this work we were concerned with only amorphous silicon p-i-n photodiode detectors in a-Si:H pixel arena.

The contributions and new findings in this work are summarized as follows:

- A numerical model is presented with consideration of both carriers for photodiode in a-Si:H pixel sensor and the model include the combined effects

of charge transport properties of the photodiode, operating conditions, and physical geometry. The analyses in this research have identified the important parameters of photodiode that optimize the overall pixel performances; by which can ultimately unswerving to the reduction of exposure consistent with healthier diagnosis for different operating modalities.

- A customized simulator is also written based on presented numerical model and used for optimizing model device performance to ensure maximal transient photoresponse. Although the simulator have the capability to manipulate all possible parameters of pixel photodiode, but this work was to study with critical operational measures like field, dose, diode thickness and exposure optimizations.
- A prototype pixel structure is presented in order to achieve about 100% fill factor and a fabrication techniques are illustrated in appendix G in order to realize model device.
- The soft-hand experiments reveal that the reduction of the photocurrent at low reverse bias is caused by the injection of the electrons and their recombination with trapped holes. The deeply trapped carriers also contribute to this reduction.
- Trapped carriers density is graphically presented and configured the trapping nature of either carrier as the other parameters change in both physical and operational measure.
- The photoresponses can be optimized by the change of a-Si:H active layer and the geometry of the collection electrode. The increase in photosensitivity with

graded bottom electrode can be attributed to the enhanced collections efficiency.

- The investigations divulge that the higher dose (around 8×10^{14} $cm^{-2}s^{-1}$) implication caused early deep trapping and lost significant numbers of carriers. However, these trapped carriers release in the post illuminations period and limits the device for fluoroscopic use.
- Higher exposure time also has the same adverse effect as experienced in higher dose implication. The massive bulk recombination and deep trapped are observed i.e. trapping rate higher than that of regular trend for particular diode operation.

The carriers are deeply trapped in large numbers in the mobility gap and near n^+/p^+ bottom contact, especially the contact places trapped carriers caused injection currents. Note the recombination current included bulk recombination currents are drawn in opposite way to the primary photocurrent direction. Therefore, the measured photocurrent is reduced, and the transient current after switching off illumination has opposite to the stationary photocurrent.

The transient photoresponses, and thereby imaging characteristics critically depend on the photodiode charge transport properties, active layer material, applied bias, dose, exposure duration, and the detector thickness, *i.e.*, the size of the pixel and the thickness of the photodiode. All parameters have been critically examined by customized simulator in chapter 5 and the simulator code is illustrated in APPENDIX-F. From overall depictions, it is fair enough to conclude that 1 μm photodiode detector in pixel sensor having been 2 V/μm bias promoted optimized transient photoresponse once

ensured 5~6.8 milliseconds exposure with generation rate 10^{14} $cm^{-2}s^{-1}$. Further demonstration of total functionality of pixilated array sensors by means of locally auto-adaptive real-time supervisory sensitivity control, the system would no doubt more efficient, accessible and dynamically engineered.

6.2 Suggestions for future works

We suggest to the following for the future works to extend this research further:

- Although the smaller pixels are advantageous in terms of higher resolution and optimal photoresponse, but cross-talk between neighbor pixels may deviate the results as delivered by individual case. Therefore, transient photoresponse model in active matrix array detectors can be further explored in order to realize true image detector in large area implication.
- In trapped carriers probabilistic measure in model calculations, we considered only 34 discrete levels in the mobility gap (a-Si:H active layer) with 50 meV apart. This was insufficient in consideration with successive trapping inside mobility gap. Due to computer speed limitation, we could not increase the number of track level to reach much closer to continual traps realization. Indeed, supercomputer may facilitate for extended calculations.

7.0 References

[1] M. Hoheisel, "Review of X-ray detectors for medical imaging," *Siemens- Medical Engineering Group*, Germany, ICANS 21 - Science and Technology, Lisbon Portugal, September 4-9, (2005).

[2] Dimitra G. Darambara, "The Role of Amorphous Silicon Large Area Flat-Panel Detector Technology in Future Digital Mammography," *Radiation Physics Group*, Department of Medical Physics and Bioengineering University College London, U.K.

[3] Cowen A.R., "Digital x-ray imaging," *Measurement Science and Technology*, 2, pp. 691-707, (1991).

[4] Kallergi M., "Computer-aided diagnosis of mammographic microcalcification clusters," *Medical Physics*, 31, pp. 314-326, (2004).

[5] Guler N.F. and Ubeyli E.D., "Theory and applications of telemedicine," *Journal of Medical Systems*, 26, pp. 199-220, (2002).

[6] Larry E. Antonuk, Youcef El-Mobri, et al., "A large-area 97 μm pitch, indirect-detection, active matrix, flat-panel imager (AMFPI)," Physics of Medical Imaging, *SPIE Proc.*, 3336, pp13, (1998).

[7] On-line official website (http://www.dpix.com/tech.html) ©2007 *dpiX, LLC* | 3406 Hillview Ave, Palo Alto, California 94304, USA

[8] G.P. Wecker, "Operation of p-n Junction Photodetectors in a Photon Flux Integration Mode," *IEEE Journal of solid state Circuits*, Vol. SC-2, No. 3, pp65-67, September, (1967).

[9] H. Taun, "Application of Amorphous Silicon Thin Film Transistors to Linear Array," *SPIE Vol.* 763, pp. 65-67, (1967).

[10] R. A. Street, S. Nelson, L. Antonuk, and V. Perez-Mendez, "Amorphous Silicon Sensor Arrays for Radiation Imaging," *Proc. MRS Symp. Proc.*, Vol. 192, pp. 441-451, (1990).

[11] M. Powel, I. French, J. Hughes, N. Bird, O. Davies, C. Glasse, and J. Curnan, "Amorphous Silicon Imaging Sensor Arrays," *MRS Symp. Proc.*, Vol. 258, pp. 1127-1136, (1992).

[12] L. Antonuk, Y. El-Mohri, J. Siewerdsen, J.Yokston, and R.A. Street, "A Large Area, High-Resolution a-Si:H Array for X-ray Imaging," *MRS Symp. Proc.*,. Vol. 336, pp. 855-856, (1994).

[13] R. Weisfield, "Large-Area Amorphous Silicon TFT-Based X-ray Image Sensors for Medical Imaging and Non-Destructive Testing," *proceedings of the fourth symposium on Thin Film Transistor Technologies*, edited by Y. Kuo, PV. 98-22, pp. 369-380, (1998).

[14] H. Wieczorek, "Effects of trapping in a-Si:H Diodes," *Solid State Phenomena*, vol. 44-46, pp. 957-972, (1995).

[15] SAFA O. KASAP, senior member, IEEE, and John A. Rowlands, "Direct-Conversion Flat-Panel X-Ray Image Sensors for Digital Radiography," *Procedings of the IEEE*, vol. 90, no. 4, April (2002).

[16] Ulrich Neitzel, "Status and prospects of digital detector technology for CR and DR," *Philips Medical Systems*, Germany, Vol. 114, Number 1-3, pp. 32-38, Oxford journal, (2005).

[17] Richard L. Weisfield, Mark A. Hartney, Robert A. Street, Raj B. Apte, "New Amorphous-Silicon Image Sensor for X-ray Diagnostic Medical Imaging Applications," *dpiX, LLC*, 3406 Hillview Ave., Palo Alto , CA 94034-1345, and Xerox Palo Alto Research Center, 3333 Coyote Hill Road, Palo Alto, CA; 94304.

[18] Varian Ginzton Research Center, V*arian Medical Systems*, 2599 Garcia Avenue Mountain View, CA 94043-1111, (2006).

[19] L. E. Antonuk, J. Boudry, W. Wang, D. McShan, E. J. Morton, J. Yorkston, and R. A. Street, "Demonstration of megavoltage and diagnostic X-ray imaging with hydrogenated amorphous silicon ar-rays," *Med. Phys.*, vol. 19, no. 6, pp. 1455–1466, November, (1992).

[20] M. Hoheisel, M. Arques, J. Charbal, C. Chaussant, T. Ducourant, L. Fritsch, G. Hahm, H. Horbaschek, J. Michailos, R. Schulz, M. Soahn, V. Spinnier, and G. Vieux, J. M. Marshall "Amorphous silicon X-ray detectors," *Future Directions in Thin Film Science and Technology*, Singapore, p. 112, (1967).

[21] K. Suzuki, "Flat panel displays using amorphous and monocrystalline semiconductor devices," *Amorphous and Microcrystalline Semiconductor Devices: Optoelectronic Devices*, J. Kanicki, Ed. Boston, MA: Artech House, chapter 3, (1991).

[22] J. A. Rowlands and J. Yorkston, "Flat panel detectors for digital radiography," in Handbook of Medical Imaging, J. Beutel, H. L. Kundel, and R. L. Van Metter, Eds. Washington, DC: *SPIE*, vol. 1, (2000).

[23] C. A. Klein, "Bandgap dependence and related features of radiation ionization energies in semiconductors," *J. Appl. Phys.*, vol. 39, no. 4, pp. 2029–2038, March, (1968).

[24] Street, R. A., "Hydrogenated Amorphous Silicon," *Cambridge University Press, Cambridge*, (1991).

[25] G. Wei and H. Okamoto, "Amorphous Silicon Photovoltaic X-ray Sensor," January, J. Applied Physics, Vol. 24, No. 8, pp. 1105-6, (1985).

[26] Gevay, G., "*Prog. Crystal Growth chemistry*," Page 15 & 145, (1987).

[27] Owen, A.E., Anthony J. Snell, Janos Hajto, Peter G. Lecomber, "Amorphous Silicon Memory,, *US patent 5360981*, dated November 1, (1994).

[28] Elvira M.C. Fortunato, Donatello Brida, Isabel M.M. Ferreira, H. M.B. Águas, Patrícia Nunes, Ana Cabrita, Franco Giuliani, Yuri Nunes, Manuel J.P. Maneira, and Rodrigo F.P. Martins, "Large Area Flexible Amorphous Silicon Position Sensitive Detectors," *Materials Research Society*, 506 Keystone Drive, Warrendale, PA 15086-7573.

[29] Richard L. Weisfield, "Large-Area Amorphous Silicon TFT-based X-ray Image Sensors for Medical Imaging and Non-Destructive Testing," *dpiX, LLC*, Hillview Ave. Palo Alto, CA 94034-1345.

[30] J. Anthony Seibert, "Flat-panel detectors: how much better are they?," *Journal Pediatric Radiology*, Department of Radiology, University of California Davis Medical Center, 4860 Y St., Ste. 3100, Sacramento, CA 95817, USA, 22 July, (2006).

[31] K. Tanaka, E. Maruyama, T.Shimada, and H. Okamoto, "Amorphous Silicon," *John Wiley Son*, Chichester, (1999).

[32] S.Elliot, "Physics of Amorphous Materials, (2nd edition)," *Longman Group Limited*, United Kingdom, (1990).

[33] Anderson, P.W., "Absence of diffusion in certain random lattices," *Physical Review*, 109, pp. 1492 – 1505, (1958).

[34] Mott, N.F., "Electrons in disordered structures," *Advances in Physics*, 16, pp. 49 – 57, (1967).

[35] Cohen, M.H., Fritzsche, H., and Ovshinski, S.R.. "Simple band model for amorphous semiconductor alloys," *Physical Review Letters*, 22, pp. 1065 – 1072, (1969).

[36] Marshall, J.M., and Owen, A.E., "Drift mobility studies in vitreous arsenic triselenide," *Philisophical Magazine*, 24, pp. 128 L – 1290, (1971).

[37] Kaiser, I., Nickel, N. H., Fuhs, W. & Pilz, W. "Hydrogen-mediated structural changes of amorphous and microcrystalline silicon," *Phys. Rev.* B 58, R1718-R1721, (1998).

[38] Shirai, H., Hanna, J. & Shimizu, I. "Role of atomic hydrogen during growth of hydrogenated amorphous silicon in the 'chemical annealing'," *Jpn J. Appl. Phys.* 2 30, L679-L682, (1991).

[39] Saravanapriyan Sriraman, Sumit Agarwal, Eray S. Aydil and Dimitrios Maroudas, "Mechanism of hydrogen-induced crystallization of amorphous silicon," *Nature* 418, 62-65 (4 July 2002) | doi:10.1038/nature00866; Received 4 February 2002; Accepted 15 May, (2002).

[40] Madan, A. And Shaw, P., "The physics and application of amorphous semiconductors," *Academic Press*, San Diego, P. 117, (1988).

[41] Tuttle, B. & Adams, J. B. "Energetics of hydrogen in amorphous silicon," *Phys. Rev. B* 57, 12859-12868 , (1998).

[42] Street, R. A., "Large area electronics, applications and requirements," *Phys. Status Solidi* A 166, 695-705, (1998).

[43] Street, R. A., "Hydrogenated Amorphous Silicon," *Cambridge University Press*, Cambridge, page 63, (1991)

[44] Street, R.A., "Localized states in doped amorphous silicon," *Journal of Non-Crystalline Solids*, 77 & 78, pp.1-16.

[45] Staebler, D.L., Wronski, C. R., *Appl. Phys. Lett.* 31, 292–294, (1977).

[46] R.A. Street, "Hydrogenated Amorphous silicon," *Cambridge university press*, page 19, (1991).

[47] J. Pankove, "Hydrogenated Amorphous Silicon," Semiconductor and materials:, Vol. 21, , *Academic press*, Inc., (1984).

[48] W. Luft and Y. Tsuo, "Hydrogenated Amorphous Silicon Alloy Deposition Process," *Marcel Dekker*, Inc., (1993).

[49] A. M. Amir, "Development of a Novel Etch Fabrication Technology for Amorphous Silicon Thin-Film Transistors," *Ph.D thesis, University of Waterloo*, (1995).

[50] Sze, S. M., "Physics of Semiconductor Devices," New York: *Wiley*, 1981.

[51] Rhoderick, E. H., "Metal–Semiconductor Contacts," *Oxford University Press*, (1978).

[52] Crowell, C. R., Rideout, V. L., "*Solid-State Electron*," 12, pp. 89–105, (1969).

[53] Tao, S., Ma, Q., Striakhilev, D.S., Nathan A., *Mater. Res. Soc. Symp. Proc.* 609, A12.2.1–6, (2001).

[54] Kramer, N., van Berkel, C., *Appl. Phys. Lett.* 64, 1129–1131, (1994).

[55] Vink, T. J., Nieuwesteeg, J. B. M., Oversluizen, G., J. *Appl. Phys.* 71, 4399–4404, (1972).

[56] Rothwarf, A., Pereyra, I., "*Solid-State Electron*", 24, pp.1067–1070, (1981).

[57] Wong S., Huang H. "Networked Multimedia for Medical Imaging," Wong S., Huang H. *IEEE MultiMedia* 4(2): 24-35, (1997).

[58] The Broadband for Rural and Northern Development Pilot Program, *Industry Canada/Health Canada*, Source web: http://broadband.gc.ca/pub/program.

[59] R. A. Street, M. Hack, and W. B. Jackson, "Microscopic mechanism for dopant activation in hydrogenated amorphous silicon," *Phys. Rev.* B 37, 4209, (1988).

[60] R. A. Street and K. Winer, "Defect equilibria in undoped a-Si:H," *Xerox Corporation*, Palo Alto Research Center, Palo Alto, California 94304, February, (1989).

[61] M. Stutzmann, Philos., R. A. Street, "Hydrogen chemical potential and structure of a-Si:H," *Xerox Palo Alto Research Center*, Palo Alto, California 94304, (1990).

[62] K. Winer, "Defect formation in a-Si:H," *Xerox Corporation*, Palo Alto Research Center, Palo Alto, California 94304, Phys. Rev. B 41, 12150, (1990).

[63] G. Schumm and G. H. Bauer, "Defect chemical potential and the density of states in amorphous silicon" *J. Non-Cryst. Solids*, 37&138, 315, (1991).

[64] M. J. Powell and S. C. Deane, "Defect-pool model and the hydrogen density of states in hydrogenated amorphous silicon," *Philips Research Laboratories*, Redhill, Surrey, RH1 5HA, United Kingdom.

[65] M. Z. Kabir, E. V. Emelianova, V. I. Arkhipov, M. Yunus, G. Adriaenssens, and S. O. Kasap, "The effects of large signals on charge collection in radiation detectors: application to amorphous selenium detectors," *Journal of Applied Physics*, 99, 124501, (2006).

[66] K. C. Kao and W. Hwang, "Electrical transport in Solids," Pergamon Press, London, chapter 5, (1981).

[67] R. J. Schilling and S.L. Harris, "applied Numerical Methods for Engineers using MATLAB and C," Pacific Grove, California, Brooks/Cole, chapter 9, (2000).

[68] M. Zahangir Kabir, M. Yunus, and S. O. Kasap, "Dependence of x-ray sensitivity of direct conversion x-ray detectors on x-ray exposure and exposure history," Proc. *SPIE – Int. Soc. Opt. Eng.*, 5368, pp. 170-176, (2004).

[69] *dpix brochure*, The Large Area Amorphous Silicon Company, L.L.C, 3406 Hillview Avenue, Palo Alto, CA 94304-1345www.dpix.com.

[70] Jackson, W. B., Kelson, S. M., Tsai, C. C., Allen, J. W., and Oh, S._J., *Phys. Rev. B* 31, 5187, (1985).

[71] Schiff, E. A. "S*olar Energy Materials and Solar Cells*", 78, 567-595, (2003)

[72] Martini M., Mayer J.W., and Zanio K.R., "Trapping in semiconductors – transient charge technique," *Applied State Science*, Academic Press, (1972).

[73] G. E. Forsythe and W. R. Wasow, "Finite-difference methods for partial differential equations," *John Wiley & sons, Inc.*, New York, USA, p.141-1431960.

[74] J. Crank and P. Nicolson, "A practical method for numerical evaluation of solutions of partial differential equations of the heat-conduction type," *Advances in Computational Mathematics*, 6, pp. 207-226, (1996).

[75] *Microfabrication Laboratory*, University of Pennsylvania Electrical Engineering School.

APPENDIX-A

Experiment conducted at varying a-Si:H photodiode thickness with constant applied fields. A successive track down of Schubweg/photodiode (PD) thickness ratio ($\mu\tau F/d$) by observing photocurrent status, keeping all other parameters unchanged including field $2x10^6$ V/m.

Applied field, *F* (Volt/micrometer)	**Photodiode thickness, d**		**Schubweg/PD thickness ratio ($\mu\tau F/d$)**	**Photocurrent status**
	In nanometer↓	**Increase/Decrease**		
2.0	500	-	139.992	Present
	600	↑	116.600	Present
	700	↑	99.994	Present
	800	↑	44.773	Present
	900	↑	69.996	Present
	1000	↑	58.330	Present
	1200	↑	49.997	Present
	1400	↑	44.329	Present
	1600	↑	43.747	Absent
	1580	↓	44.301	Absent
	1579	↓	44.329	Present
	1579.3	↑	44.321	Present
	1579.4	↑	44.318	Absent

APPENDIX-B

Experiment conducted at varying applied fields with constant a-Si:H photodiode thickness. A successive track down of Schubweg/photodiode (PD) thickness ratio ($\mu\tau F/d$) by observing photocurrent status, keeping all other parameters unchanged including PD thickness to 1.58 μm.

Applied field, *F*		**Photodiode thickness (d), μm**	**Schubweg($\mu\tau F$)/d (ratios)**	**Photocurrent status**
Volt per micrometer↓	**Increase/Decrease**			
2.000000	-	1.58	44.3012358	Absent
2.001000	↑		44.3234165	Present
2.000500	↓		44.3123411	Absent
2.000600	↑		44.3145562	Absent
2.000800	↑		44.3189863	Absent
2.000900	↑		44.3112014	Present
2.000850	↓		44.3200939	Present
2.000840	↑		44.3198724	Present
2.000839	↓		44.3198502	Absent
2.0008395	↑		44.3198613	Present
2.0008392	↓		44.3198546	Absent
2.0008393	↑		44.3198568	Present

APPENDIX-C

Experiment conducted at varying a-Si:H photodiode thickness with constant applied fields. A successive track down of Schubweg/photodiode (PD) thickness ratio ($\mu\tau F/d$) by observing photocurrent status, keeping all other parameters unchanged including field $3x10^6$ V/m.

Applied field, *F* (Volt/meter)	Intrinsic thickness, d		Schubweg ($\mu\tau F$)/d (ratios)	Photocurrent status
	In nanometer↓	Increase/Decrease		
$3x10^6$	1.3800	-	76.082609	Present
	1.5000	↑	69.996	Present
	1.6000	↑	65.62125	Present
	1.8000	↑	58.33	Present
	2.0000	↑	52.49700	Present
	2.2000	↑	47.72455	Present
	2.3000	↑	45.64957	Present
	2.3500	↑	44.67830	Present
	2.3600	↑	44.48899	Present
	2.3680	↑	44.33868	Present
	2.3690	↑	44.31997	Present
	2.36910	↑	44.31810	Absent
	2.37000	↑	44.30127	Absent
	2.38000	↑	44.11513	Absent
	2.40000	↑	43.74750	Absent
	2.41000	↑	43.56598	Absent
	2.42000	↑	43.38595	Absent
	2.50000	↑	41.99760	Absent

APPENDIX-D

Experiment conducted at varying applied fields with constant a-Si:H photodiode thickness. A successive track down of Schubweg/photodiode (PD) thickness ratio ($\mu\tau F/d$) by observing photocurrent status, keeping all other parameters unchanged including PD thickness to 2.37 μm.

Applied field, *F*		**Photodiode thickness (d), μm**	**Schubweg($\mu\tau F$)/ d (ratios)**	**Photocurrent status**
Volt per meter↓	**Increase/Decrease**			
3.001	-	2.37	44.31603	absent
3.05	↑		45.03962	Present
3.04	↓		44.89195	Present
3.03	↓		44.74428	Present
3.015	↓		44.52277	Present
3.012	↓		44.48847	Present
3.01	↓		44.44894	Present
3.008	↑		44.4194	Present
3.005	↓		44.3751	Present
3.003	↑		44.34557	Present
3.002	↓		44.3308	Present
3.00125	↑		44.31972	Present
3.001246	↓		44.31967	Present
3.001245	↓		44.31965	Absent

APPENDIX-E: Finite Difference Method; a Basis for Simulator Code Writing

The first step in using finite difference method (FDM), pre-processing, is constructing a finite difference model of the structure to be analyzed. There have been numbers of FDM available, among them widely used numerical techniques named finite difference method to solve partial differential equation are rigorously popular. For instance backward Euler method that is an implicit method, meaning that one should solve an equation to finds P_{n+1}. Although it is time consuming approach, however this implicit method is more stable, especially for solving a stiff equation, meaning that a larger step size (Δx *or* Δt) can be used. It is often inefficient to use the same step size all the time. So, variable step-size methods have been introduced in the simulator to avoid above mentioned disadvantage indeed. Usually, the step size is chosen such that the local error per step is below some tolerance level, that means the methods must also compute an error indicator, an estimate of the local error as well.

Let's few consideration for initial condition before exposure to make it easier calculations;

$$p(x,0)=0,\ n(x,0)=0,\ p_t(x,0)=0,\ n_t(x,0)=0,\ and\ F(x,0)=1 \qquad \text{(E.1)}$$

The boundary condition for electric field;

$$\int_0^1 F(x,t)dx = 1 \qquad \text{(E.2)}$$

Suppose we are interested in solving equations (4.1) to (4.4) and (4.6) over the space interval $0 < x < 1$, and the time interval $0 < t < 1$. For example, we compute a numerical solution by estimating p(t,x) over a uniform grid consisting of $m+1$ values of t

and n +1 values of x as shown in Figure E.1. Let Δt and Δx denote the step sizes of the variables t and x respectively.

$$\nabla t = \frac{1}{m} \text{ and } \nabla x = \frac{1}{n} \tag{E.3}$$

To simplify the final equations, let t_k and x_j denote the values of t and x at the grid points. That is,

$$t_k = k\,\Delta t, \qquad 0 \leq k \leq m \tag{E.4}$$

$$x_j = j\Delta.x, \qquad 0 \leq j \leq n \tag{E.5}$$

Let denote the computed value of $p(t_k, x_j)$. We need initial and boundary condition to get unique solution to the problem. The initial and boundary conditions for p(t,x) are:

$$P(0, x) = 0, \quad 0 < x < m \tag{E.6}$$

$$P(t, 1) = 0, \qquad t>0 \tag{E.7}$$

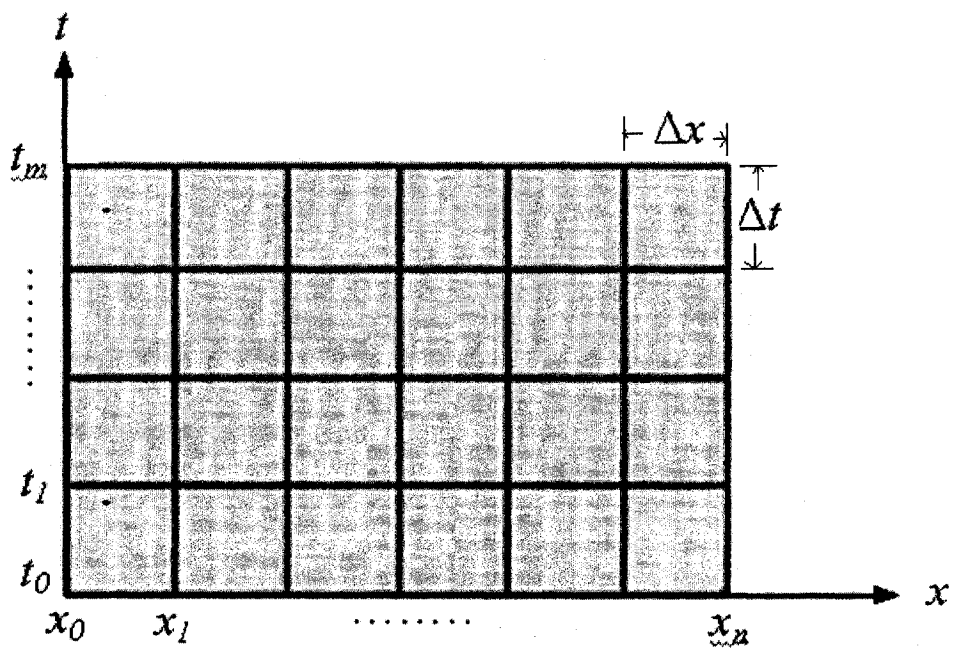

Figure E.1: Grid used to obtain a numerical solution to the equations (4.1) to (4.4) and (4.6).

Each method has some advantages and disadvantages in terms of stability, convergence and required time for calculation. In spite of some disadvantage, we choose the implicit backward Euler method to solve partial differential equations in this thesis since it is unconditionally stable [67]. In backward Euler method, the difference approximation is taken from its value from an earlier time, i.e., the difference approximation is evaluated at t_{k+1} rather than t_k Thus,

$$\frac{\partial p(t_{k+1}, x_j)}{\partial t} = \frac{p_j^{k+1} - p_j^k}{\nabla t} \tag{E.8}$$

$$\frac{\partial pF(t_{k+1}, x_j)}{\partial x} = \frac{p_j^{k+1} F_j^{k+1} - p_{j-1}^{k+1} F_{j-1}^{k+1}}{\nabla x} \tag{E.9}$$

Using t_{k+1} as the reference time in place of t_k, it is for the effect of making the Euler approximation of $\frac{\partial p}{\partial t}$ in (E.8) with a backward difference mode. Substituting equation (E.8) and (E.9) into (4.2) we get,

$$\frac{\partial p}{\partial t} = \mu_h \frac{\partial (pF)}{\partial x} - \sum_{m=1}^{17} C_{hm} p(N_m - p_{tm}) - \sum_{m=18}^{34} C_{hm} p n_{tm} + \sum_{m=1}^{17} \frac{p_{tm}}{\tau_{rhm}} + G$$

Applying Euler backward difference method;

$$\frac{p_j^{k+1} - p_j^k}{\nabla t} = \mu_h \frac{p_j^{k+1} F_j^{k+1} - p_{j-1}^{k+1} F_{j-1}^{k+1}}{\nabla x} + \frac{p_j^{k+1}}{\tau_{hmj}^{k+1}} - C_{hm} p_j^{k+1} n_{tmj}^{k+1} - C_{hm} p_j^{k+1} n_{tmij}^{k+1} + K_j^k e^{-\frac{x}{\nabla}} \tag{E.10}$$

Here, $G = g(x,t) e^{-\alpha x'} \Rightarrow G = K_j^k e^{-\alpha x d} \Rightarrow G = K_j^k e^{-x/\Delta}, and \rightarrow \Delta = \frac{1}{\alpha d}$

$$\therefore p_j^{k+1} \left[\frac{1}{\nabla t} - \frac{\mu_h F_j^{k+1}}{\nabla x} - \frac{1}{\tau_{hj}^{k+1}} + C_{hm} n_{tmj}^{k+1} + C_{hm} n_{tmij}^{k+1} \right] = \frac{p_j^k}{\nabla t} - \mu_h \frac{p_{j-1}^{k+1} F_{j-1}^{k+1}}{\nabla x} + K_j^k e^{-\frac{x}{\nabla}} \tag{E.11}$$

$$\text{or,} \quad p_j^{k+1} A_h = \frac{p_j^k}{\nabla t} - \mu_h \frac{p_{j-1}^{k+1} F_{j-1}^{k+1}}{\nabla x} + K_j^k e^{-\frac{x}{\nabla}} \tag{E.12}$$

$$\text{where,} \quad A_h = \left[\frac{1}{\nabla t} - \mu_h \frac{F_j^{k+1}}{\nabla x} - \frac{r_\mu}{\tau_{hj}^{k+1}} + C_R n_j^{k+1} + C_{hm} n_{hmij}^{k+1} \right] \tag{E.13}$$

$$\text{Or,} \quad A_h = \left[\frac{1}{\nabla t} - \mu_h \frac{F_j^{k+1}}{\nabla x} - \frac{r_\mu}{\tau_{hj}^{k+1}} + C_{hm} n_j^{k+1} + C_{hm} n_{hmij}^{k+1} \right] \tag{E.14}$$

For simplicity and practical purposes, we assume;

$$\left| F_j^{k+1} - F_{j-1}^{k+1} \right|, \quad \left| n_j^{k+1} - n_j^k \right|, \quad \left| n_{ij}^{k+1} - n_{ij}^k \right|, \text{ or } \left| \tau_{hj}^{k+1} - \tau_{hj}^k \right| << 1$$

But direct formulation get involve more complex situation during two-dimensional calculations and writings it's subsequent simulation code. Therefore, we search for alternate easy access and versatile approach in this context. For simplicity, we applied normalized measure for simulation. The space step size $\Delta x = 10^{-2}$ is sufficiently small for getting a reasonable accuracy. The time step size Δt was varied from 2.5×10^{-4} to 2.5×10^{-5} and did not get any noticeable change in the numerical results. Therefore, the time step size Δt = 2.5 $\times10^{-4}$ is assumed to be sufficiently small for getting a reasonable accuracy. The above formulations are valid for negative bias. The same procedure can be applied for positive bias case, provided all the continuity and rate equations are changed accordingly.

As mentioned above, the value of Δt was chosen less than 2.5 $\times10^{-4}$ in all calculations and so the equation (E.14) is justified for this Δt. Then, p_j^{k-1} can be calculated using equations (E.12) & (E.14) and the solution proceeds in space from left to right as in Figure E.1. Alternately, approximate values of n_j^{k-1}, n_{ij}^{k-1} *and* F_j^{k-1}can be calculated explicitly (forward Euler method) from all variables at t_k using equations (4.1)

to (4.4) & (4.6), and then p_j^{k-1} can be calculated using equations (E.12) & (E.13) [73][74]. Eventually we employed the above techniques on to our numerical model that demonstrated in chapter 4 and created customized simulator in matlab program that provided following kind of soft-hand experimental results as shown in figure F.1 in APPENDIX-F.

APPENDIX F: Customized simulator code for a-Si:H pixel sensor soft-hand operation

```
%The following code is written for pixel sensor soft hand operation in general and need
%to be adjusted for inter-matrix element matching for particular functionalities. The
%appropriate critical data should enter in order to simulate the device.

clear all
   f =F; d = 1*(10^-6); tauhd = 1.666*10^-5; taued = 3*10^-7;   Id = 1e-7 ;
   e = 1.60218*10^-19; er = 11.8;  e0 = 8.8542*10^-12;    muh =.003*(10^-4);
   mue =1*(10^-4);  te = d/(mue*f);   ru = muh/mue ;
   tauh = (muh*tauhd*f)/d;     taue = (mue*taued*f)/d;
   alfa = 3.4e6; delta=1/(alfa*d); eta = 1-exp(-1/delta);  nfact = 1/(delta*eta);
   z=1;
   d1=1e-7:1e-7:1e-6;
  for z = 1:length(d1)
     del(z)=1/(alfa*d1(z));
     eta1(z)=100*(1-exp(-1/del(z)));
     z=z+1;
  end

  T = 295 ; KT = .02542 ; Ncd = 4e26 ; NcE = 1.6e28 ; NvE = 6e27 ; Ec = 1.75 ;
  Eoc = .03 ; Eov = 0.05 ; Ndt = 5e21 ; Ndd = 5e20 ; w0 = 1e13 ;  Ef0 = Ec -0.9 ;
  dE = 0.001 ; Ectd = Eoc*log(NcE/Ndt) ; Evtd = Eov*log(NvE/Ndt) ;
  Ectdd = dE*fix(Ectd/dE);  Ect = Ec - Ectdd ; Evt = dE*fix(Evtd/dE) ;
  a = Evt/dE ;  b = Ect/dE ; c = Ec/dE ; E = [0:dE:Ec] ; Evdd = [0:dE:Evt-dE] ;
  Edd = [dE:dE:Ectdd] ; gE(1:a) = NvE*exp(-Evdd/Eov) ;
  gE(a+1:b+1) = Ndt ; gE(b+2:c+1) = Ndt*exp(Edd/Eoc);
  fmef = 1./(1+exp((E-Ef0)/KT)) ;  NiE= gE.*(1-fmef) ;
  nitE = gE.*fmef ; pitE = gE.*(1-fmef);  m =100; n = 50;
  i = 0 ;
  for Et = .9:.05:1.6
       i = i+1 ;
       Eie(i) = Et ;
       EtN = fix(Et/dE);
       Nid(i) = 0.05*gE(EtN) ;
       nitd(i,1:n+1)=0.05*nitE(EtN) ;

if i <=9
       we(i) = 8e11 ;
   else we(i) = 4e11 ;
   end
end
  tn = length(Nid) ;
```

```
  intauer= (te*we).*(exp((Eie-Ec)/KT));

j = 0 ;
 for Et = .85:-.05:.15
   j = j+1 ;
   Eih(j) = Et ;
   EtP = fix(Et/dE);
   Pid(j) = 0.05*gE(EtP) ;
   pitd(j,1:n+1) = 0.05*pitE(EtP) ;
   if j <=4
      wh(j) = 3e12 ;
   else wh(j) = 4e11 ;
   end
 end
   tp = length(Pid) ;

  intauhr= (te*wh).*(exp(-Eih/KT)) ;

  Td = 1 ; m =100;  n = 50;  a = 1; T =  Td; dt = T/m;dx = a/n; t = [0 : dt : T];
  x = [0 : dx : a];
   ch = zeros(m+1,n+1); ce = zeros(m+1,n+1); Rei = zeros(tn,n+1); Rhi = zeros(tn,n+1);
  fld = zeros(1,n+1);
      ce(m+1,1:n+1) = 0;  ch(m+1,1:n+1) = 0; fld(m+1,1:n+1) = 1;
    g0 = 5e19; q0 = g0*eta*te; c0 =(e*q0)/(er*e0*f); p0 = q0/d ; Nc = Ncd/p0 ;
  Nv = Nc ;  Ni = Nid/p0 ;  Pi = Pid/p0 ; nit = nitd/p0 ; pit = pitd/p0 ;
  nt = sum(nit); pt = sum(pit);
%
  jh(1) = 0; je(1) = 0;  jt(1) = 0;
  for tx = 1:20000
   count = tx
   for ntt = 1:500
   ce(1,1:n+1) = ce(m+1,1:n+1);  ch(1,1:n+1) = ch(m+1,1:n+1);
   fld(1,1:n+1) = fld(m+1,1:n+1) ;
  %
  fld(1,1)= 0 ;
  for j = 2 : n+1
   fld(1,j) = fld(1,j-1) + 0.5*c0*dx*(ch(1,j)+ch(1,j-1) + pt(j)+ pt(j-1) - ce(1,j)- ce(1,j-1)-
   nt(j)-nt(j-1));
   end
     c1 =-1-trapz(x,fld(1,1:n+1));
     fld(1,1:n+1) = -(c1+fld(1,1:n+1)) ;
     for k = 1 : m
     for i = 1:tn
        for j = 1: n+1
      intauei(i,j) = ((Ni(i)-nit(i,j))*we(i)*te)/Nc;
```

```
        Rei(i,j) = ce(k,j)*intauei(i,j)- nit(i,j)*intauer(i);
      nitn(i,j)=nit(i,j) + dt*Rei(i,j);
        intauhi(i,j) = ((Pi(i)-pit(i,j))*wh(i)*te)/Nc;
      Rhi(i,j) = ch(k,j)*intauhi(i,j)- pit(i,j)*intauhr(i);
      pitn(i,j)=pit(i,j) + dt*Rhi(i,j);
     end
    end
     Re = sum(Rei) ; nt = sum(nitn) ; Rh = sum(Rhi) ; pt = sum(pitn) ;
     ch(k+1,n+1)=nfact*(dt/Td)*exp(-1/delta);
     for j = 1 : n
      ah = 1/dt + ru*fld(1,n+1-j)/dx  ;
      ch(k+1,n+1-j)=(1/ah)*(ch(k,n+1-j)/dt + ru*ch(k+1,n+2-j)*fld(1,n+2-j)/dx - Rh(n+1-
j) + nfact*(1/Td)*exp(-(n-j)/(n*delta)));
     end
     ce(k+1,1)=nfact*(dt/Td);
     for j = 2 : n+1
      ae = 1/dt + fld(1,j)/dx  ;
      ce(k+1,j)=(1/ae)*(ce(k,j)/dt + ce(k+1,j-1)*fld(1,j-1)/dx - Re(j) + nfact*(1/Td)*exp(-
(j-1)/(n*delta)));
     end
     nit = nitn ; pit = pitn ;  %
      fld(k+1,1)= 0 ;
      for j = 2 : n+1
        fld(k+1,j) = fld(k+1,j-1) + 0.5*c0*dx*(ch(k+1,j)+ch(k+1,j-1) + pt(j)+ pt(j-1) -
ce(k+1,j)- ce(k+1,j-1)- nt(j)-nt(j-1));
      end
          c1 =-1-trapz(x,fld(k+1,1:n+1)); fld(k+1,1:n+1) = -(c1+fld(k+1,1:n+1)) ;
    end
  end
   fdce = fld(1,1:n+1).*ce(m+1,1:n+1) ;  fdch = fld(1,1:n+1).*ch(m+1,1:n+1) ;
   jex(m+1) = trapz(x,fdce);  jhx(m+1) = ru*trapz(x,fdch);
   je(tx+1)=jex(m+1) ;   jh(tx+1)=jhx(m+1) ;
    end
 jt = je + jh ; jed = e*mue*f*p0*je; jhd = e*muh*f*p0*jh;
 jtd = jed+jhd; td = [0:1:tx]*500*te ;
%
ietd = []; ihtd = [];
for tdcy =
[.000001:.000001:.0001,.00011:.00001:.001,.0011:.0001:.01,.011:.001:.1,.11:.01:1,1.1:.1:
10,11:1:100,110:10:10000];
   raet = intauer.*exp(-tdcy*intauer/te) ;  raht = intauhr.*exp(-tdcy*intauhr/te) ;
  for i = 1:tn
  for j = 1: n+1
     qett(i,j) = nit(i,j).*raet(i) ;
    qhtt(i,j) = pit(i,j).*raht(i) ;
  end
```

```
 end
 qet = sum(qett) ;  qht = sum(qhtt) ;  qetx = qet.*(1-x);
 qhtx = qht.*x ;  ietdd = trapz(x,qetx);  ihtdd = trapz(x,qhtx);
 ietd = [ietd ietdd];   ihtd = [ihtd ihtdd];
end
 itdcye =ietd*e*q0/te; itdcyh=ihtd*e*q0/te;
 tdcy =
[.000001:.000001:.0001,.00011:.00001:.001,.0011:.0001:.01,.011:.001:.1,.11:.01:1,1.1:.1:
10,11:1:100,110:10:1000];
```

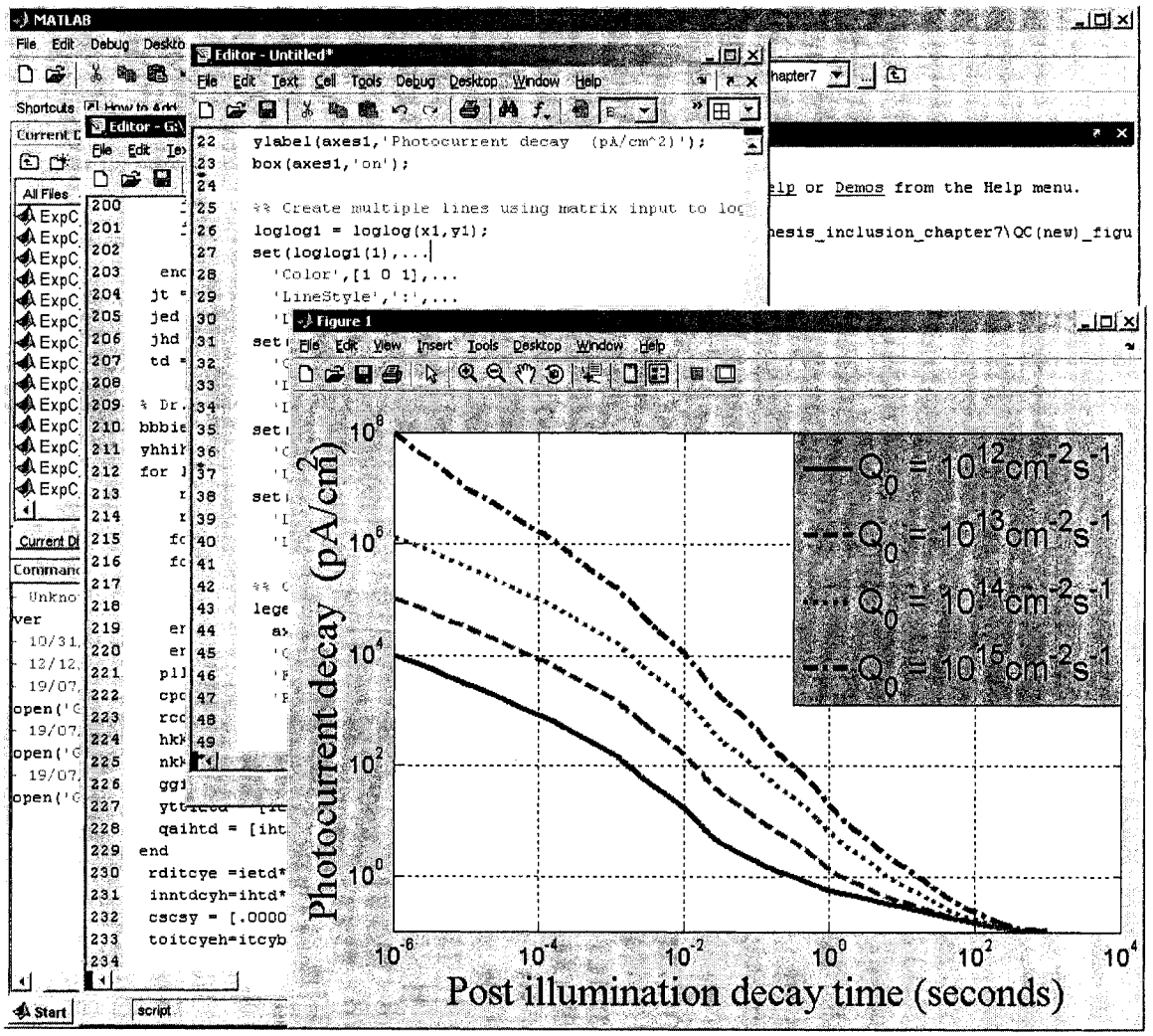

Figure F.1: Customized simulator workability illustrations.

APPENDIX-G: Prototype a-Si:H Pixel fabrication process techniques

G.1 Substrate selection for a-Si:H pixel fabrication

An active-matrix substrate is inherently loaded mechanical holds and complex circuitry in integrated system-on-chip (SoC) fashion. The fabrications involves more sophisticated in highly compact space and very precision with physical stress or deformation, especially during fabrication process to reach device level structure. Therefore, the substrate should be thermally tolerable shrinkage as well as sufficient mechanical strength, permissible fatigue, and proportional toughness, for instance glass. Because the substrate, itself has to pass through several thermal process directly or indirectly to reach device level structure. The industrial grade, commercially available Corning™ 7059 or equivalently Corning EAGLE^{2000} display grade substrate are widely being used in AMFPA fabrication. The latter brand was selected for pixel substrate with trade marked glass parameters at Mil-Std-105E quality, especially the interest of good waviness that are branded with the glass 0.7±0.07mm. For simplicity and avoiding substrate etching, it is preferable to have customized surface topology as shown in Figure G.1(a).

G.2 Echants for active matrix pixel fabrication

For amorphous silicon micro-structuring, wet-etching can be employed. In general wet etching is isotropic, meaning it directs etch in all directions at the same rate. But in amorphous silicon, wet etch-process showed good selectivity when etched by KOH [75]. The echants and etch conditions are given in Table G.1. On the other hand,

complete removal of ITO has no question of an extra cut by etching. In our model device, there is no partial removal of ITO. However, this technique needs cumbersome optimization of the various constituent gases partial pressures to ensure constant etch rate. The effects of photodiode dimensions and photon fluence to actuation are already studied in spatial regime in chapter 4 and 5. In continuation of true device, we started with patterning of Mo (the bottom electrode) on the glass substrate as bottom electrode by sputtering deposition. n^+a-Si:H, intrinsic a-Si:H, and p^+a-Si:H deposited in alternative techniques on bottom electrode in one process run. Followed by amorphous layers, ITO is to be sputtered as top electrode.

Table G.1: Wet etchants for fabrication of photodiodes.

Etch object	Etchants	Proportionate	Temperature(°C)	Ref.
Mo	H_2SO_4 : HNO_3: H_2O	1:1:5 (parts)	~12 μm @ 25 °C	[75]
a-Si:H	KOH	(10 wt. %)	40	
n^+ a-Si:H				
P^+ a-Si:H				
Al	H_3PO_4:CH_3COOH:HNO_3:H_2O		40	
ITO	HCL (18%) : Fe Cl_3	~ 1 L : 5.6 g	50	

G.3 a-Si:H photodiode fabrication into integrated pixel arena

The lithographical pattern vertically extended source-drain is to be deposited using technically feasible mask with echants as listed in Table G.1. Horizontally deposited TFT channel as well as amorphous layers has to be deposited by PECVD process measure as shown in Table G.2; followed by lithographical gate dielectrics deposition by conventional dry oxidation method on ward. The crucially metallization of

gate electrode, as well as bottom electrode of storage capacitor has to be subsequently fabricated to proceed final shape as shown in Figure G.1 and Figure G.2.

Table G.2: Deposition parameters for fabrication of pixilated a-Si:H pixel photodiode.

Layer to deposit	Pressure (Torr)	Power (W)	Substrate Temperature, °C	Gas	Deposition process
Mo (Bottom electrode)	5×10^{-3}	400	R.T	Ar.	DC sputtering
n^+ a-Si:H	0.15	12	260	$\frac{PH_3}{SiH_4}=1\%$	PECVD
a-Si:H (Active layer)	0.5	12	260	SiH_4=50 sccm	PECVD
p^+ a-Si:H	5×10^{-3}	400	R.T	Ar.	PECVD
ITO (Top electrode)	0.02	300	R.T	Ar	DC/RF sputtering

On the other hand, highly doped (n^+) microcrystalline amorphous silicon (μc- a-Si:H) layer has to be employed at electrode interface region in photodiode in order to reduce the contact resistance. The TFT and storage capacitor as depicted in Figure 5.1 were also adapted [15] in build prototype manner, maintaining conventional principle remains the same except the physical geometry and position in order to achieve about 100% fill factor (FF).

Table G.3: Pixel photodiode (PPD) structural geometry for design fabrication.

Mode of layers	Thickness, nm	Remarks
Molybdenum as bottom electrode	80	PPD surface area ≈2.5 mm^2
N+ a-Si:H	30~50	
a-Si:H	870~850	
P+ a-Si:H	30~50	
ITO as top electrode	100	

The proposed prototype structure offered about 100 % fill factor (FF) with no significant fabrication cost involvements. The process parameters for depositions are summarized in Table G.2, and pixel photodiode (PPD) dimension are illustrated in Table G.3.

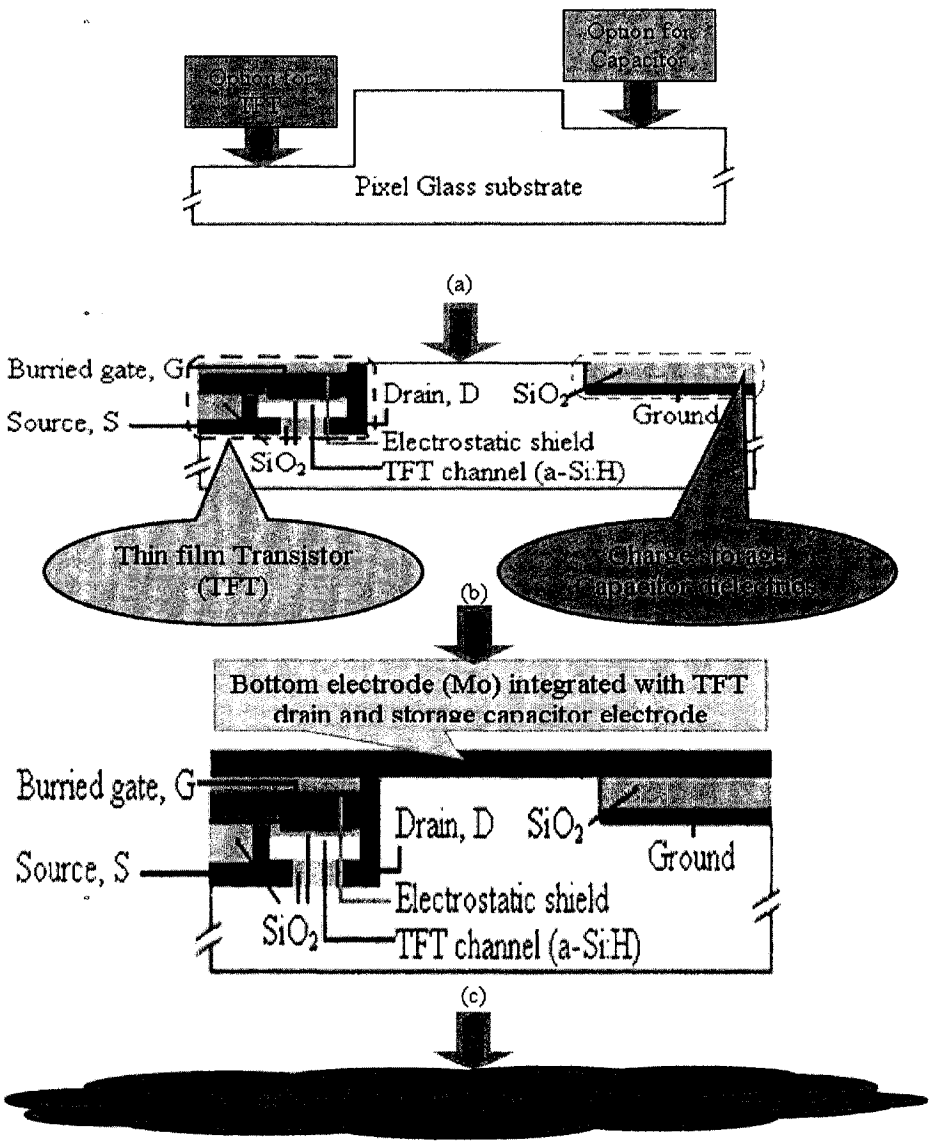

Figure G.1: Pixel fabrication process steps (a) Customized glass (Corning EAGLE^{2000}) substrate (b) TFT and charge storage capacitor integration (c) Bottom electrode layer formation by DC sputtering (continued to figure G.2).

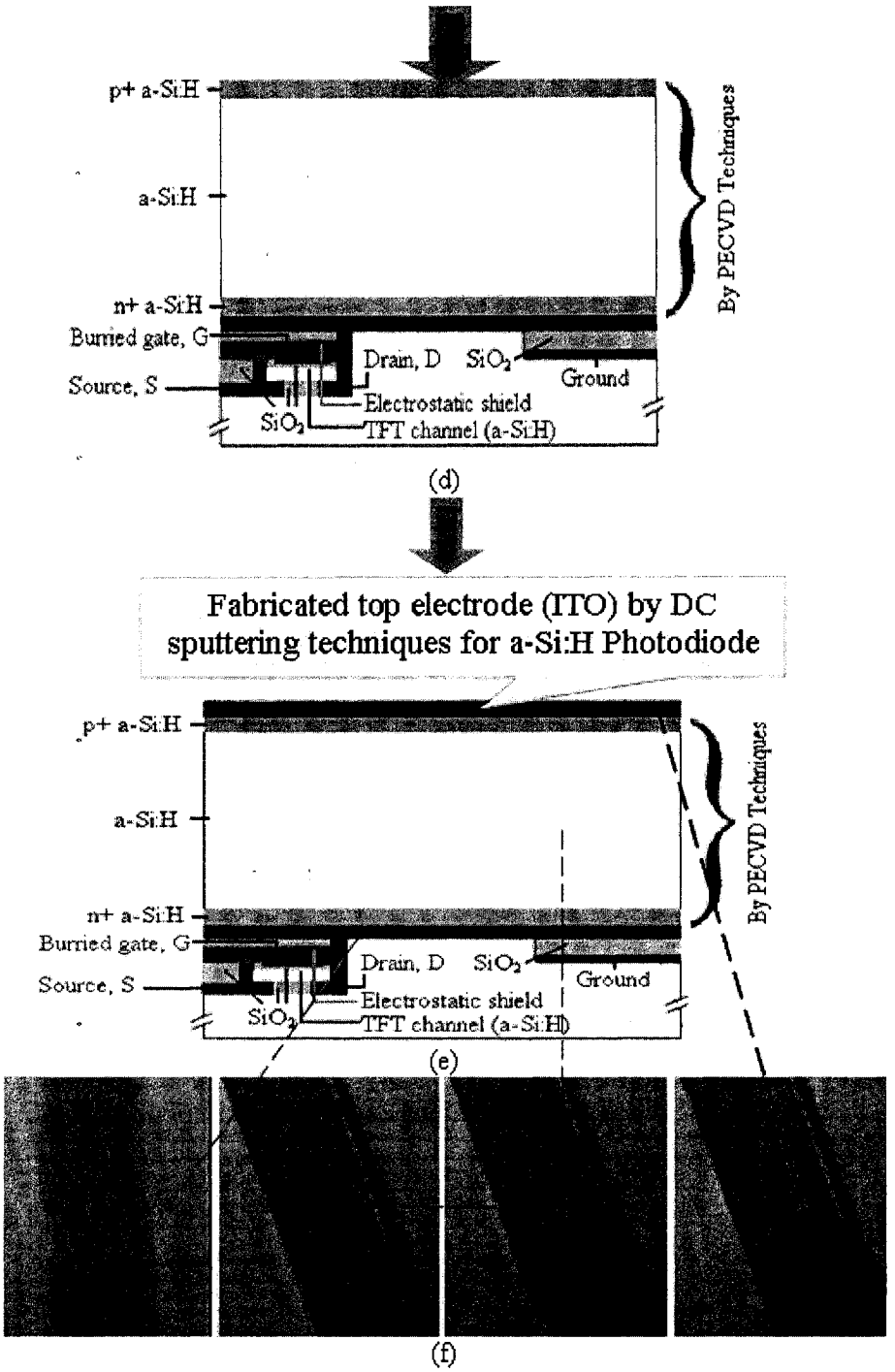

Figure G.2: Pixel fabrication process steps in progress after figure G.1, (d) Hydrogenated amorphous silicon active layers deposition by PECVD techniques (i) n+ a-Si:H (ii) Intrinsic a-Si:H layer in the middle (iii) On top of intrinsic region p+ a-Si:H layer. (e) Indium Tin Oxide (ITO) as top transparent electrode, deposited by RF sputtering, instead very slow rate DC sputtering an alternate. (f) A fabricated model pixel photodiode (PDD) ≈ Mo~30nm, a-Si:H~1μm, ITO~30nm.

The intrinsic silicon was sputtered on the bottom electrode (Mo) by RF sputtering and the ITO taken over on that being top transparent electrode. The final structure got a shape of p-i-n photodiode as shown in Figure G.2 (f). The plasma enhanced CVD techniques should be employed in order to achieve amorphous grade silicon structure. The process sequences are illustrated in Figures G.1 and Figure G.2, however, we asked for external facility in this regard and yet to be accomplished undeniably.

In the above fabrication strategy, a single pixel are depicted but mostly focused on photodiode. In integrated 3D regime, the active layer of the photodiode for each pixel is to be isolated from the surroundings in order to minimize cross-talk between neighboring pixels in large area imaging AMFPA productions. The a-SiN_x:H layer can be employed as etch mask in the a-Si:H etching to avoid etchants penetrate through undesirable area. But highly densed a-SiN_x:H film is quite difficult to make and costly. However, inclusion of a-SiN_x:H is extensively useful to suppress built-in stress, which prevents film peel-off, especially when the etching is taken over large area flat panel fabrication.